

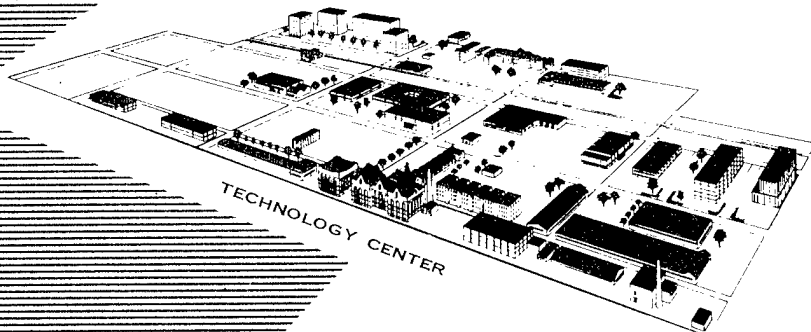
2013

0-31

ARF 4132-10

ARF

ARMOUR RESEARCH FOUNDATION OF ILLINOIS INSTITUTE OF TECHNOLOGY



**DISTRIBUTION STATEMENT A**  
Approved for Public Release  
Distribution Unlimited

SHOCK IMPINGEMENT EXPERIMENTS

ON CRUSHABLE SOLIDS

P. Lieberman

AEC Research and Development Report  
Contract No. AT(11-1)-528

Index:

- ① Shock wave in solids
- ② Shock tubes; testing of solids
- ③ Solids; shock propagation

Reproduced From  
Best Available Copy

20000920 215

## LEGAL NOTICE

This report was prepared as an account of Government sponsored work. Neither the United States, nor the Commission, nor any person acting on behalf of the Commission.

- A. Makes any warranty or representation, express or implied, with respect to the accuracy, completeness, or usefulness of the information contained in this report, or that the use of any information, apparatus, method, or process disclosed in this report may not infringe privately owned rights; or
- B. Assumes any liabilities with respect to the use of, or for damages resulting from the use of any information, apparatus, method, or process disclosed in this report.

As used in the above, "person acting on behalf of the Commission" includes any employee or contractor of the Commission to the extent that such employee or contractor prepares, handles or distributes, or provides access to, any information pursuant to his employment or contract with the Commission.

Printed in USA. Price \$2.50. Available from the Office of  
Technical Services, Department of Commerce  
Washington 25, D. C.

ARF 4132-10  
Reactors-General

ARMOUR RESEARCH FOUNDATION  
of  
ILLINOIS INSTITUTE OF TECHNOLOGY  
Technology Center  
Chicago 16, Illinois

SHOCK IMPINGEMENT EXPERIMENTS  
ON CRUSHABLE SOLIDS

P. Lieberman

United States Atomic Energy Commission  
Contract No. AT(11-1)-528  
ARF No. D132D09

June 1959

This is a technical report on Task No. 12 (formerly Task No. 4), "Shock Crushing of Reactor Shield Materials," ARF No. D132D09, performed by Armour Research Foundation for the United States Atomic Energy Commission under Contract No. AT(11-1)-528, "Studies of Reactor Containment." The work reported herein was performed from July 1958 through February 1959.

Foundation personnel who have contributed materially to this report include P. Lieberman and T.A. Zaker. The experiments and analysis reported herein were performed by P. Lieberman. E. J. Murry, J. B. Eichler, and E. J. Lewandowski assisted in the conduct of tests and in data reduction.

Respectfully submitted,

ARMOUR RESEARCH FOUNDATION OF  
ILLINOIS INSTITUTE OF TECHNOLOGY

*P. Lieberman*

P. Lieberman, Task Engineer

*T. H. Schiffman*

T. H. Schiffman, Assistant Director  
of Propulsion and Fluids Research

APPROVED:

*F. B. Porzel*

F. B. Porzel, Senior Science Advisor  
Propulsion and Fluids Research

PL/cmh

ARMOUR RESEARCH FOUNDATION OF ILLINOIS INSTITUTE OF TECHNOLOGY

## ABSTRACT

A 2-in. inside diameter shock tube was used to generate strong flat-topped shock waves in argon for impingement against cylindrical specimens of celotex, redwood, and sugar pine up to 6 in. in length. Shock pressures up to 120 atmospheres were induced in the specimens immediately following impingement. Piezoelectric crystal pressure sensors were used to record pressure-time histories in the gas upstream of the gas-solid interface.

A method of obtaining points on the shock pressure-specific volume curve (the Hugoniot) for each solid from the experimental data is given in the present report. The results for each material are presented graphically, and are compared with isothermal confined static compression data. Rather large volume changes are evidenced in shock at pressures in the neighborhood of the crushing strength for each material. The crushing strength of celotex in shock appears to be well above its confined static crushing strength, and the crushing strengths in shock of redwood and sugar pine appear to be somewhat below the corresponding static crushing strengths.

## TABLE OF CONTENTS

	<u>Page</u>
ABSTRACT . . . . .	v
LIST OF SYMBOLS . . . . .	xiii
I. INTRODUCTION . . . . .	1
II. EXPERIMENTATION . . . . .	6
A. Equipment . . . . .	6
1. The Shock Tube . . . . .	6
2. Gas System . . . . .	6
3. Combustion Driver . . . . .	7
4. Diaphragms . . . . .	8
5. Instrumentation . . . . .	9
B. Procedure . . . . .	10
III. THEORETICAL CONSIDERATIONS . . . . .	12
A. Reflection Phenomena . . . . .	12
B. Methods of Analysis of Data . . . . .	19
1. Static and Dynamic Pressure-Volume Relationships . . . . .	19
2. Derivation of the Hugoniot from Experimental Data . . . . .	24
IV. TEST RESULTS . . . . .	26
A. Film Records . . . . .	26
B. Effect of Various Materials on Reflected Pressures . . . . .	27
1. Stationary End Condition . . . . .	28
2. Celotex Samples . . . . .	29
3. Redwood Samples . . . . .	30

## TABLE OF CONTENTS (CONT'D)

	<u>Page</u>
4. Pine Samples . . . . .	30
C. Effect of Specimen Length . . . . .	31
V. ANALYSIS OF RESULTS . . . . .	33
A. Predictions and Results Regarding Reflected Pressures . . . . .	33
B. Results Regarding the Hugoniot for Solids . . . . .	36
VI. CONCLUSIONS . . . . .	39
VII. RECOMMENDATIONS . . . . .	40
BIBLIOGRAPHY . . . . .	42
APPENDICES	
A. APPROXIMATE PREDICTION OF REFLECTED PRESSURES	A-1
B. DETERMINATION OF POINTS ON THE HUGONIOT	B-1
C. SHOCK TUBE PERFORMANCE	C-1

## LIST OF ILLUSTRATIONS

<u>Diagram</u>	<u>Page</u>
I     Pressure History and Wave Diagram for the Shock Tube . .	13
II    Conditions at Gas-Solid Interface Under Step-Wave Impact .	17
III   Correlation of Typical Shock Compression Data Points . . .	23
 <u>Figure</u>	
1     Schematic of Shock Tube Facility for Crushing Reactor Blast Shield Materials . . . . .	43
2A    Photograph of Shock Tube Facility - Over-All . . . . .	44
2B    Photograph of Shock Tube Facility - Recording Instrumentation . . . . .	45
2C    Photograph of Shock Tube Facility - Schlieren Optical Triggering System . . . . .	46
3     Pressure Distribution Throughout the Shock Tube at Various Times . . . . .	47
4     Typical Incident Pressure Versus Time Histories at Two Stations Downstream of Ruptured Diaphragm (Redwood Specimen) . . . . .	48
5     Reflected Pressures of Rigid Sample Holder, Celotex, Redwood, and Sugar Pine . . . . .	49
6A    Reflected Pressures of Rigid Sample Holder at Various Pressures . . . . .	50
6B    Reflected Pressures of Celotex at Various Pressures . . .	51
6C    Reflected Pressures of Redwood at Various Pressures . .	52
6D    Reflected Pressures of Sugar Pine at Various Pressures .	53
7A    Reflected Pressures of Various Lengths of Celotex . . . .	54
7B    Reflected Pressures of Various Lengths of Redwood . . . .	55
7C    Reflected Pressures of Various Lengths of Sugar Pine . . .	56
8A    Photograph of Celotex Sample Before and After Crushing .	57



## LIST OF ILLUSTRATIONS (CONT'D)

<u>Figure</u>		<u>Page</u>
8B	Photograph of Redwood Sample Before and After Crushing .	58
9A	Graph of Incident Shock Wave Velocity and Particle Velocity for Various Incident Shock Wave Strengths (Theoretical) . .	59
9B	Graph of the Ratio of the Velocity of Sound in the Incident Wave as Compared to the Velocity of Sound in the Driven Gas for Various Shock Wave Strengths (Theoretical) . . . .	60
9C	Graph of Relative Particle Velocities in the Reflected and Incident Waves for Various Incident Shock Wave Strengths (Theoretical) . . . . .	61
10	Graph of Static Pressure Versus Specific Volume for Celotex, Redwood, and Sugar Pine (Empirical) . . . . .	62
11	Graph of Celotex, Redwood, and Pine Particle Velocities Under Various Dynamic Pressures (Semi-Empirical). . . .	63
12	Graph of Reflected Pressures of Rigid Sample Holder, Redwood, Celotex, and Pine for Various Incident Shock Wave Strengths (Semi-Empirical) . . . . .	64
13	Graph of Diaphragm Burst Pressure Ratio Versus Generated Shock Wave Strength (Theoretical Versus Experimental) . . . . .	65
14A	Graph of Reflected Pressures of Rigid Sample Holder (Theoretical Versus Experimental) . . . . .	66
14B	Graph of Reflected Pressures of Celotex (Theoretical Versus Experimental) . . . . .	67
14C	Graph of Reflected Pressures of Redwood (Theoretical Versus Experimental) . . . . .	68
14D	Graph of Reflected Pressures of Sugar Pine (Theoretical Versus Experimental) . . . . .	69
15A	Graph of Reflected and Static Pressures Versus Final Length Ratio for Celotex (Experimental) . . . . .	70
15B	Graph of Reflected and Static Pressures Versus Final Length Ratio for Redwood (Experimental) . . . . .	71

LIST OF ILLUSTRATIONS (CONT'D)

<u>Figure</u>		<u>Page</u>
15C	Graph of Reflected and Static Pressures Versus Final Length Ratio for Sugar Pine (Experimental) . . . . .	72
16A	Data Points for the Hugoniot for Celotex . . . . .	73
16B	Data Points for the Hugoniot for Redwood . . . . .	74
16C	Data Points for the Hugoniot for Sugar Pine . . . . .	75

## LIST OF SYMBOLS

<u>Symbol</u>	<u>Definition</u>
A	= velocity of sound in gas
L	= length of solid specimen
m	= molecular weight of gas
P	= absolute pressure
$R_o$	= universal gas constant, 1545 lb-ft/mol-°R
T	= absolute temperature
t	= time
v	= specific volume
w	= wave velocity
x	= distance coordinate along shock tube axis
$\gamma$	= specific heat ratio of a gas
$\rho$	= mass density

### Subscript

i:	initial
f:	final
1:	initial state of driven gas
2:	state of driven gas after shock
3:	state of driver gas after rarefaction
4:	initial state of driver gas
5, 5', 5'':	states of driven gas after shock reflections
6:	initial state of solid specimen
7:	state of solid specimen after initial shock
8, 9:	states of solid specimen after succeeding wave reflections

## SHOCK IMPINGEMENT EXPERIMENTS ON CRUSHABLE SOLIDS

### I. INTRODUCTION

In problems relating to safety and protection against uncontrolled rapid releases of energy from a large power-generating nuclear reactor installation, it is necessary to reduce the hazard to nearby personnel and physical facilities. After all preventive safety precautions have been exhausted, there still exists the possibility that in one of the many future nuclear installations there may occur an incident where an accidental "runaway" or other malfunctioning of the reactor system causes an unexpected sudden release of a large amount of energy. It then becomes necessary to devise means of attenuating the mechanical effects of the energy release within small distances from the source. A great deal of uncertainty is associated with the magnitude of the probable energy release. Consequently, a rather conservative attitude has to be adopted in regard to providing the defense against such excursions.

An effective means of attenuating the blast pressures from an explosion is to interpose a crushable, shock-absorbing medium between the explosion source and the facilities to be protected. A device based essentially on this principle has been proposed by Armour Research Foundation as a blast shield for nuclear reactor installations. A detailed discussion of some of the aspects of such a device is given in a design study for an experimental boiling water reactor at Argonne National Laboratory<sup>1</sup>. The shield designed for that reactor consists of alternating

---

<sup>1</sup>Superscript numerals refer to bibliography section.

layers of compressible (redwood and celotex) and rigid (steel) materials. The effectiveness of the device stems from the blast-absorbing characteristics of the compressible materials and from the mismatch in acoustic impedance at the interfaces of the sandwich.

In recent work at the Foundation a method was developed for evaluating the decay of pressure with distance from a point source release of energy in a solid medium<sup>2</sup>. Pressures are assumed to be well above those at which the shear rigidity of the material is important. The method hinges on a technique for calculating the fraction of specific internal energy made unrecoverable as mechanical energy by the shock process. The materials to which the technique is applicable are of a class such that the Hugoniot and the adiabatic expansion following shock are represented by nearly coincident traces in the pressure-specific volume ( $P, v$ ) plane. This is strictly true only if the equation of state of the material is of the form  $P = f(v)$ ; i. e., a third variable, such as the temperature, is absent. In this case the canonical equation of state of the material  $E = E(v, S)$ , where  $E$  and  $S$  are respectively the specific internal energy and specific entropy, has the separated form  $E = E_1(v) + E_2(S)$ . Furthermore, for this case entropy is a function of temperature only, and none of the shock-induced vibrational (or thermal) energy is recoverable mechanically. Such materials can be expected to be efficient blast absorbers. The recoverable specific internal energy is represented by the area under the expansion adiabat in the  $P, v$  plane; this is the mechanical energy which is transported forward in the material and sustains the shock wave.

Certain materials, such as wood, foamed concrete and glass, and porous insulating board are known to exhibit pronounced hysteresis in

their mechanical properties. That is, the material after compression to pressures well above its yield point (or crushing strength) returns upon release of the load to a density not far different from its compressed density. Thus only a negligible amount of expansion work can be recovered from the material, and nearly all the specific internal energy imparted to the material by shock is made unavailable to sustain the shock. Materials exhibiting such hysteresis should therefore be quite efficient as blast shielding materials (see Fig. 9 of Ref. 1).

The design of a blast shield on the assumption that the recoverable energy after shock is very small is presented in Ref. 1. Energy-absorbing characteristics of several materials were inferred from static compression tests. Cylindrical specimens 2 in. in diameter and 2 in. in length were inserted into a heavy-walled fixture and loaded through a ram in an 800,000-pound universal testing machine. Load was applied and volume decrements were recorded until an ultimate compression ratio was reached. The load was relaxed slowly and corresponding volume ratios were recorded. Redwood and celotex were finally selected for the compressible laminae of the shield, based on the favorable crushing and hysteresis characteristics of these materials at various pressure levels.

The materials selected for the blast shield designed for EBWR at Argonne National Laboratory were practicable expedients from the standpoint of availability and ease of construction, and were not considered optimum. In the absence of dynamic compression data on redwood and celotex, energy-absorbing characteristics had to be inferred from static compression data. It is likely that compression-expansion cycles of solids obtained from static tests may differ from compression-expansion cycles

under the dynamic conditions of a blast wave. In order to place the design of blast shields on a sound basis, data is needed on the pressure-volume relationships for shock-absorbing solids under dynamic conditions. In recent work at the Foundation, a technique was developed for obtaining a measure of the energy absorbed by a compressible medium under dynamic loading conditions<sup>3</sup>. In these experiments, stress, average strain, and strain-rate data were obtained for pine and for a type of insulating wall-board using an explosive-driven steel plate to compress the material. Displacement-time histories of the system were recorded on photographic film by means of a "smear" camera.

Other experimenters<sup>4</sup> have used small charges of high explosives in contact with metals to determine the Hugoniot for metals. These experiments involve the measurement of the velocity of the free surface of the metal on the side away from the charge. The analysis of the data makes use of the approximation that the shock-induced particle velocity is nearly doubled at the free surface. This procedure is permissible in the case of very dense materials such as metals. However, where more porous and crushable materials are involved, this approximation cannot be used.

In the theoretical work of Benedek<sup>5</sup>, the assumption is made that the solid material subjected to a hydrostatic pressure  $P_5$ , and temperature  $T_5$ , will have the same density as the same material behind a shock where the pressure is  $P_5$ , and the temperature  $T_5$ . For copper and aluminum in the region of 150,000 to 200,000 atmospheres, it has been shown experimentally that isothermal hydrostatic compression data for metals can be used in shock compression problems without much error.

In a paper on the propagation of plastic deformation in solids by von Karman<sup>6</sup>, the assumption is made that when a semi-infinite rod is suddenly given a velocity at one end, the stresses depend on the strain while the strain rate effects are negligible.

The present report describes dynamic pressure-volume data for celotex, redwood, and sugar pine obtained by shock impingement experiments performed in a strong shock tube at Armour Research Foundation. The shock tube experiments furnish a test of the assumptions of earlier work in the field of blast wave analysis in which static compression data have been used in dynamic problems. The shock tube introduces the additional factors, inherent in blast loading, of strain rate, non-isothermal compression, duration of load application, and load release which are ignored by the use of static compression data. Data from the shock tube can yield the shock pressure-specific volume relationship (the Hugoniot) of various porous materials by measurements of (1) incident pressure and reflected pressure in the gas adjacent to the free surface of the crushing solid, or (2) shock velocity through the solid and the reflected pressure in the gas, or (3) particle velocity of the solid and the reflected pressure in the gas, or (4) transmitted pressure and change of density in the solid. The theoretical basis for the approaches expressed by the four possible methods for obtaining the Hugoniot for various porous solids is discussed in the present report. This report is preliminary in that the feasibility of the shock tube for these purposes has been demonstrated, preliminary experimental data are presented, and some trends in the Hugoniot are analyzed employing the first of the four methods enumerated above.



## II. EXPERIMENTATION

### A. Equipment

#### 1. The Shock Tube

The shock tube used in this study was of circular cross section, having a 2-in. inside diameter and 1-in. wall thickness to contain pressures up to 60,000 psia. The tube was constructed with six lengths of cold-rolled steel, cold-pierced, with a corrosion-resistant interior finish of hard chrome plating 0.002 in. thick. The total interior length was 18 ft, which included a high-pressure driver section 6 ft in length, and a low-pressure driven section 12 ft in length. The low-pressure driven section rode on ball bearings and was movable for short axial distances to facilitate installing and removing diaphragms between the driver and driven chambers.

#### 2. Gas System

Helium and argon were used in the shock tube. Helium (molecular weight = 4.003) was used as the high-pressure driver gas and argon (molecular weight = 39.994) was used as the low-pressure driven gas, so that it was possible to generate strong incident and reflected shock waves for dynamic loading of the test sample (see Appendix C). Helium and argon also have desirable chemical stability under strong shock wave conditions, so that theoretical normal shock relationships assuming perfect gas behavior closely approximate actual conditions and thereby simplify data correlation. In addition, under the high temperatures associated with strong shock waves, preservation of the inner surface of the shock tube was aided by the use of these inert gases.

Helium pressures up to 2500 psia were obtained from pressurized bottles. A booster pump built by the American Instrument

Company was used to raise the helium driver pressure to 7500 psi. However, since each cycle of the booster pump took approximately 15 minutes and some cycles resulted in only 300-psi pressure increments, the booster pump was rarely used in the downstream low-pressure driven section of the shock tube.

Valving and gaging of the gas system were arranged so that the shock tube could be evacuated by a Kinney pump before loading helium and argon into their respective compartments at their respective pressures. The driver compartment of the shock tube was capable of being loaded either by the booster pump or from the high-pressure storage bottles. Figure 1 illustrates a schematic of the system; in addition, the working range of the equipment is shown.

### 3. Combustion Driver

The tests on materials described in later sections of the present report were all performed using cold (i. e. , non-combustible) driver gas. A few exploratory runs were made using combustible driver gas to establish an operating technique for tests with combustion-generated shocks in future work. This technique makes possible the subjection of test specimens to pressures up to 20,000 psi but necessitates much slower operation of the tube. We indicate here the system developed for tests with combustion driver.

A mixture of one part oxygen, two parts hydrogen, and 11.3 parts helium in the driver section of the shock tube yielded combustion pressures which were five to six times the initial pressures of the unburnt mixture. Tests showed that the expected combustion pressures were not attained when oxygen was loaded first and followed by the hydrogen-helium

mixture. However, when oxygen and hydrogen were mixed in the driver section in stoichiometric quantities and helium added later, the expected combustion pressures were attained.

Ignition was accomplished by a spark system. A high-voltage rectifier system developed an electrical charge that was stored in four 0.3-microfarad condensers at 15,000 volts. Because a strong field was generated by the discharge of the thyatron-condenser system, it was necessary to use a separate motor-generator to power the ignition system so that the recording instruments were isolated and the interference between the ignition system and the recording system was minimized.

When the thyatron gas switch circuitry was energized, the stored charge from the condensers was released across the open gaps of each of four spark plugs. Below 1000 psia static initial pressure of the oxygen-hydrogen-helium mixture, the 15,000-volt discharge was sufficient for spark ignition. Above 1000 psia static initial pressure of the mixture, 0.002-in. diameter copper wire had to be soldered across the spark plug gap for ignition (exploding wire technique). Because the spark plugs were required to remain gas-tight and to function successfully after repeated use under conditions of vacuum, high pressure, high voltage, and exposure to high-temperature combustion products, the spark plugs were custom-built at Armour Research Foundation. Four spark plugs 12 in. apart were used in the driver section so that the occurrence of a detonation wave was not often observed. Figure 1 also contains a schematic diagram of the ignition system.

#### 4. Diaphragms

A diaphragm was used to separate the high-pressure driver section

of the shock tube from the low-pressure driven section. The thickness of the cold-rolled S-3 steel diaphragms determined the rupture pressure and consequently the strength of incident pressure wave. Clean "petalling" in rupture was insured by scribing a Y-shaped pattern into the diaphragm material. The rounded edges of the flanges that clamped the diaphragm in place and the scribed rupture lines reduced the tendency for pieces of the ruptured diaphragm to shear off and move downstream. There were still some instances in which diaphragm rupture resulted in high-speed metal particles which impinged against the test sample at the downstream end of the shock tube.

When combustible driver was used, it was necessary to choose a diaphragm of thickness such that rupture would occur at a pressure just slightly lower than the expected maximum combustion pressure. Should the diaphragm rupture at a pressure much lower than the expected combustion pressure, the unreacted mixture would continue to burn as the shock wave traveled downstream. Thus it is necessary to select the diaphragm thickness so that the strength of the diaphragm closely matches the pressure of complete combustion, and the shock wave propagation and reflected processes are not complicated by the behavior of a reacting gas.

#### 5. Instrumentation

Static pressures in the driver section, driven section, and storage vessels were measured by calibrated bourdon gages. The vacuum in the shock tube was measured by a mercury manometer.

Kistler SLM piezoelectric crystal gages were used as transient pressure sensors. A Kistler PZ-14 pressure pickup rated to 2000 psi was used in the driver section with non-combustible driver gas; a 10X adapter can

be added for operation up to 20,000 psi with combustible driver gas. Three Kistler PZ-6 pressure pickups rated to 5000 psi were used in the driven section; 4X adapters can be added for operation up to 20,000 psi (see Figs. 1, 2A, 8A, and 8B).

The electrical signal from each pressure pickup passed through a piezo-calibrator and was displayed on the vertical sweep of an oscilloscope. The horizontal sweep of the oscilloscope furnished a time base and was calibrated by a Tektronix type 180 time mark generator. The pressure-time histories were displayed on Tektronix 541, 545, and 551 oscilloscopes, and permanently recorded on Polaroid film. The oscilloscopes were triggered by the signal from the upstream piezoelectric pressure pickup or alternatively by a schlieren optical system (see Figs. 1, 2A, 2B, and 2C).

The static and transient pressure gages were calibrated on an Ashcroft dead weight tester. The rise time of the piezoelectric pressure pickup was rated at 2 microseconds, while the over-all instrumentation system had a rise time of 20 microseconds with a pressure amplitude error of  $\pm 1$  per cent. However, it was difficult to read the Polaroid film record more accurately than to within approximately 2 or 3 per cent of the total deflection.

#### B. Procedure

The initial length of the test specimen was measured. The sample was press-fitted into a sample holder which was of the same cross section as the shock tube and was fitted with a steel blind-end flange. The sample holder was bolted to the driven end of the tube.

From the known compressive strength of the specimen material and from performance charts of the shock tube and diaphragm material, it

was possible to select an appropriate diaphragm thickness. The diaphragm was inserted between the driver and driven sections and the entire shock tube was evacuated. After evacuation, the vacuum pump was stopped and readings were taken on a vacuum gage and mercury manometer to monitor any air leakage into the shock tube.

Argon was loaded into the evacuated driven section until atmospheric pressure was attained. Helium was then loaded into the driver section until the helium pressure was sufficient to burst the diaphragm. Shortly before diaphragm rupture, the Polaroid films were each exposed to the luminous grid and the reference level of each oscilloscope beam was checked. Also, the bourdon gage on the driver section was monitored until the diaphragm ruptured so that burst pressure for each diaphragm thickness was checked.

Diaphragm rupture caused a shock wave to propagate downstream. When the shock wave passed the first piezoelectric pressure pickup (station 2) 62 tube diameters downstream of the diaphragm station, an electrical signal was generated which triggered all the oscilloscopes and the pressure levels at each station were recorded in the Polaroid camera of each oscilloscope. The pressure-time histories on the inside wall of the tube were recorded at gage stations 3 and 4 immediately upstream of the specimen (see Figs. 2B and 4).

The shock tube was then vented, the test sample holder was detached from the shock tube, and the crushed or final length of the sample was measured. When the sample crushed evenly (see Fig. 8A), only the original and crushed lengths were recorded. When the test sample crushed unevenly (see Fig. 8B), the original length, minimum crushed length, and

maximum crushed lengths were recorded. The test sample was removed and modes of failure were observed. The ruptured diaphragm was removed from the shock tube. If any portion of the diaphragm was sheared off and carried downstream, the test run was repeated.

Successive test runs were planned according to the following program:

1. Calibration of the shock tube which included monitoring of the incident and reflected wave pressure levels, wave shapes, and pulse durations at various test pressures.
2. Performance testing of various blast shield materials at pressure levels in the elastic and crushing ranges of each of the materials.
3. Performance testing of various sample lengths under loadings of sufficient pressure magnitude and duration to induce significant crushing in the samples.

### III. THEORETICAL CONSIDERATIONS

In this section the mechanics of shock transmission and reflection at the interface between the driven gas and the compressible solid specimen in the shock tube are discussed. This leads to methods of interpreting the test results so as to make possible the construction of the Hugoniot for the compressible solid.

#### A. Reflection Phenomena

The events following the bursting of the shock tube diaphragm are illustrated in Diagram I. This is a wave diagram conventionally used in the study of one-dimensional non-steady fluid flow problems. Following the burst of the diaphragm, a step pressure pulse (i.e., a shock followed by fairly uniform flow) is generated in the driven gas. When the shock impinges

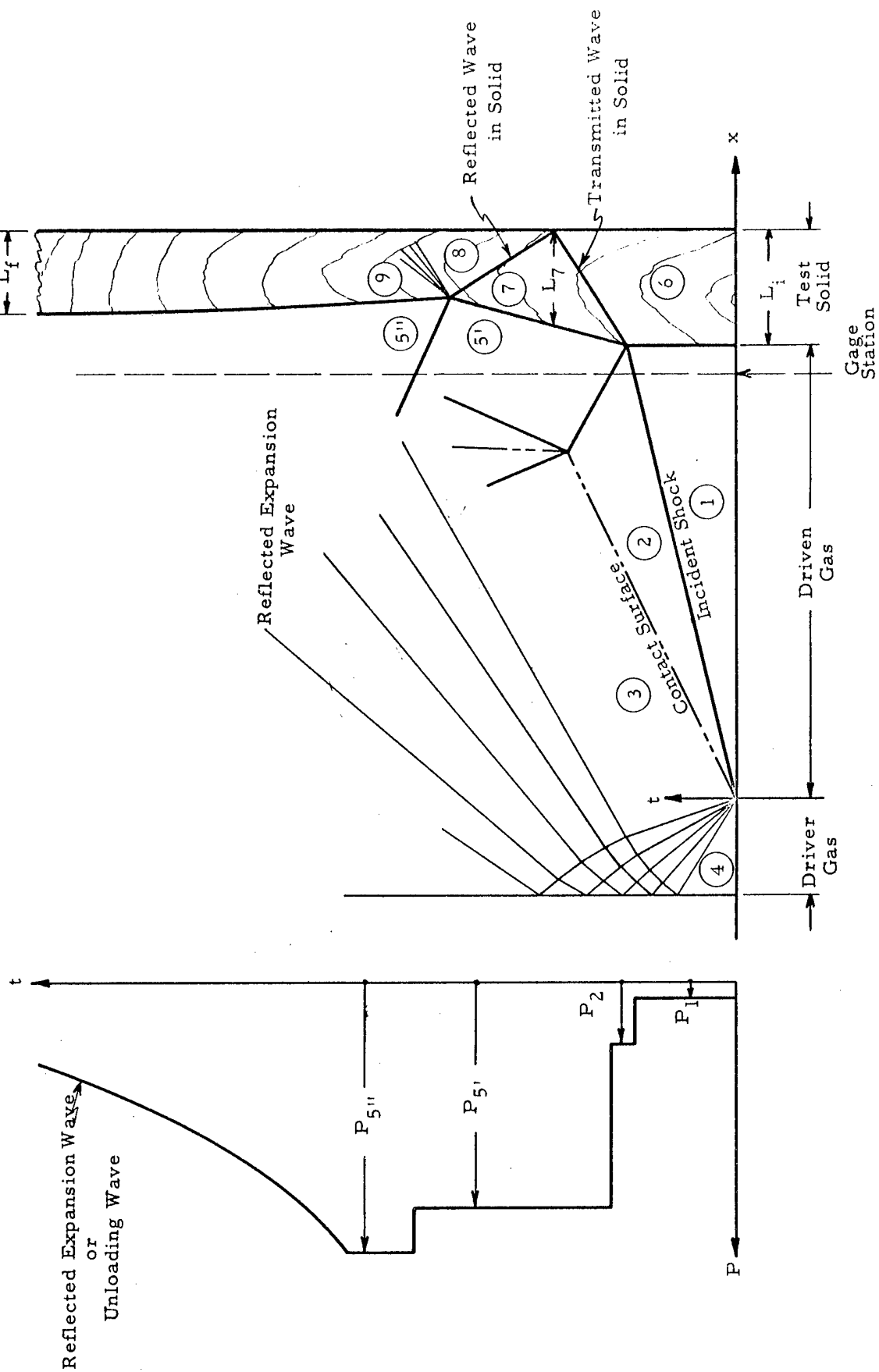


DIAGRAM I PRESSURE HISTORY AND WAVE DIAGRAM FOR THE SHOCK TUBE



on the solid surface, a wave is transmitted into the solid and another wave is reflected back into the gas.

The wave reflected from the gas-solid interface moves upstream, interacting with the contact surface between the driver and driven gases and setting up minor reflected and transmitted disturbances. This interaction is indicated in the wave diagram, but these disturbances tend to wash out with time and their later history is omitted for clarity.

The wave transmitted through the solid induces crushing at the front. If the pressure in region 5' is higher than the crushing strength of the material, the transmitted wave is essentially a step shock. The crushed material behind the shock attains a velocity depending on the strength of the transmitted wave. This velocity is also related to the strength of the wave reflected back into the gas. The gas-solid interface separating regions 5' and 7 is therefore a contact discontinuity across which pressure and particle velocity are continuous, but densities and temperatures differ in the two media.

The shock in the solid reaches the rigid end of the specimen holder and is reflected as a compressive wave of sufficient strength to bring the moving particles of the solid to rest. The pressure in region 8 is quite high, necessarily being at least twice the pressure of the original wave transmitted through the solid (region 7). When the reflected wave or stagnation front in the solid reaches the gas-solid interface, a compression wave is driven upstream into the gas and the high reflected pressure in the solid is relieved by a rarefaction or unloading wave which moves back through the solid, the pressure and particle velocity again being continuous across the gas-solid interface separating regions 5'' and 9. A complicated

sequence of compression and expansion waves thus traverses the specimen, further details of which are omitted from the diagram.

Meanwhile, a centered rarefaction wave originating at the diaphragm station at burst time moves into the driver chamber and is reflected from the rigid end of the driver chamber. This reflected rarefaction moves through the driven gas, weakening the reflected compression waves, and eventually interacting with the solid. When the intense pressures to which the solid has been subjected are relieved, the solid recovers somewhat in volume.

In Diagram I is also shown the pressure-time history in the driven gas at a station immediately upstream of the gas-solid interface. A gage at this station successively senses the initial pressure  $P_1$ , the incident pressure  $P_2$ , the pressure  $P_5$ , in the wave reflected from the moving gas-solid interface, the pressure  $P_{5'}$ , in the wave transmitted from the solid after the reflection from the rigid end of the sample holder, and finally the expansion wave reflected from the driver end of the tube.

The pressure in the solid in region 7 is thus sensed at the gage, since  $P_{5'} = P_7$  across the contact surface separating regions 5' and 7. It should be emphasized that the pressure in the solid is subsequently raised to a much higher pressure (region 8) than the pressures sensed at the gage station because of the effect of reflection of the wave in the solid at the rigid end of the sample holder.

Thus the wave diagram furnishes a qualitative picture of the events occurring after shock impingement on a compressible solid. The driven gas, argon, can be considered to behave essentially as a perfect gas. From the relationships connecting particle velocity and pressure in

reflection processes in a perfect gas, quantitative information can be deduced leading to the determination of the Hugoniot for the solid material.

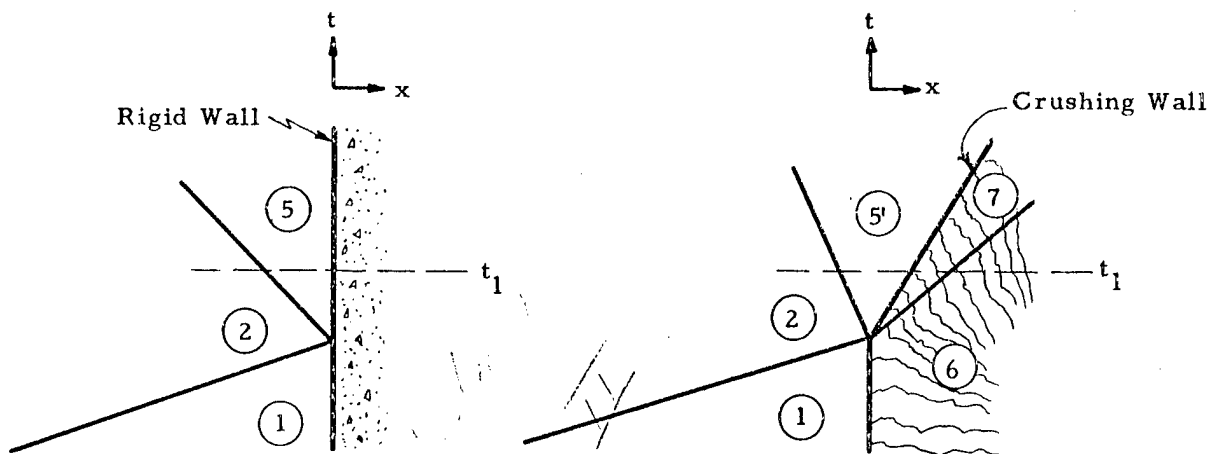
Consider now the normal reflection of a plane, flat-topped shock wave in a perfect gas from a rigid boundary. The sequence of events following reflection is shown in Diagram II. The condition of reflection from a rigid boundary requires that the reflected wave be of sufficient strength to bring the moving gas particles to rest as it sweeps upstream. The reflected pressure  $P_5$  is given in terms of the incident pressure  $P_2$  and the ambient pressure  $P_1$  by (see Ref. 7, p. 93)

$$\frac{P_5}{P_1} = \frac{P_2}{P_1} \left[ \frac{(2 \frac{\gamma-1}{\gamma+1} + 1) \frac{P_2}{P_1} - \frac{\gamma-1}{\gamma+1}}{\frac{\gamma-1}{\gamma+1} \frac{P_2}{P_1} + 1} \right], \quad (1)$$

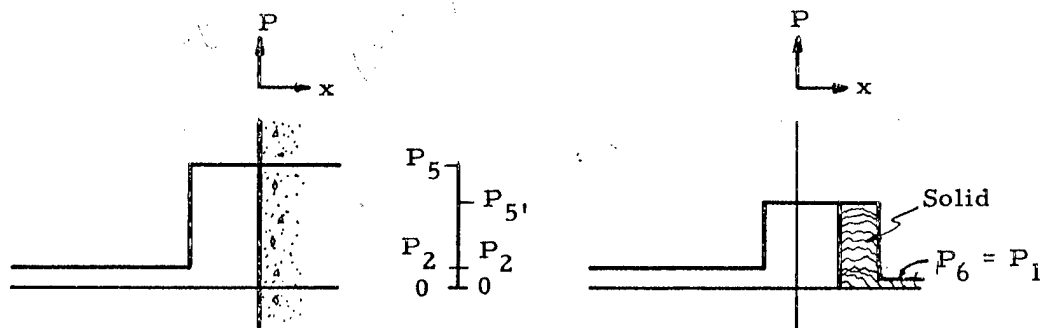
where  $\gamma$  is the ratio of specific heats of the driven gas. Argon, a monatomic gas, has a specific heat ratio of 5/3.

When a plane, flat-topped shock wave is reflected normally from the surface of a compressible material (Diagram II), motion is induced in the solid, and the condition of reflection requires that the velocities of the gas and solid be equal at the gas-solid interface. The solid may be visualized as a piston which is withdrawn at the velocity  $U_5$ , (see Fig. 3) at the instant of shock impingement. The resulting reflected pressure  $P_{5'}$  is less than the reflected pressure  $P_5$  associated with a stationary boundary.

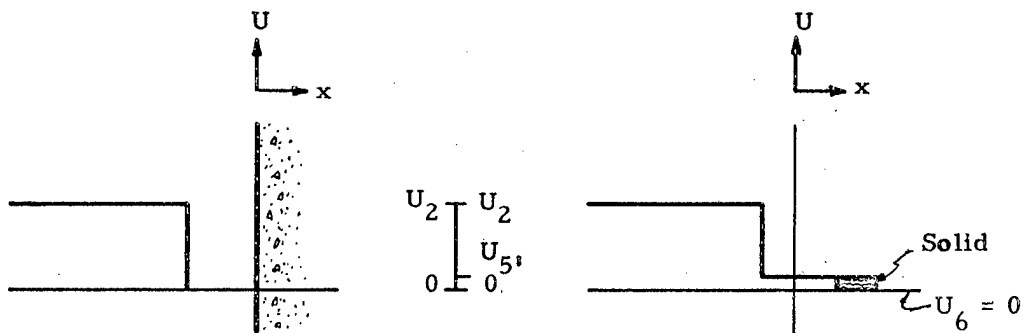
When the shock tube is fired with the specimen absent, the closed end of the sample holder presents an essentially stationary boundary for reflection of the incident wave. When a compressible specimen is inserted



A. Wave Diagrams for Rigid and Crushing Wall Wave Reflection



B. Pressure Distribution at Time  $t_1$  During Rigid and Crushing Wall Wave Reflection



C. Particle Velocity Distribution at Time  $t_1$  During Rigid and Crushing Wall Wave Reflection

## DIAGRAM II CONDITIONS AT GAS-SOLID INTERFACE UNDER STEP-WAVE IMPACT

into the sample holder, the impinging shock wave induces motion in the solid as discussed in preceding paragraphs. For the same incident shock pressure  $P_2$ , a more compressible solid reflects a lower pressure  $P_5$ , than a less compressible solid.

The precise pressure-time history in the gas immediately upstream of the specimen, shown schematically in Diagram I, is dependent on the length of the sample relative to the length of the flat-topped portion of the input wave. For a sample sufficiently long relative to the length of the input wave, the expansion wave which is reflected from the driver end of the tube arrives at the gage station ahead of the pressure  $P_5$ , which is transmitted into the gas from the solid specimen. In this case only the pressures  $P_1$ ,  $P_2$ , and  $P_5$ , are sensed at the gage before the pressure is relieved by the expansion wave. In some tests of the present study this behavior was exhibited on the pressure records. The essential measurements in the present study are, however, the pressures  $P_2$  and  $P_5$ , in the gas immediately upstream of the specimen; it was necessary to select the specimen length and gage position so that these pressures were sensed before arrival of the reflected expansion wave from the driver end of the tube.

When the applied load is below the crushing strength of a specimen, the transmitted wave in the solid is essentially an acoustic or stress wave. In this case the reflected pressure  $P_5$ , is very nearly the pressure reflected from a rigid boundary, since the particle velocity associated with the wave in the solid is very low in the absence of crushing.

The phenomena of interest to the present study involves lengths of solid specimen short enough so that the pressure and particle velocity associated with the transmitted shock in the solid can be considered uniform

over the engulfed length of the specimen. In a sufficiently long specimen, however, one would expect significant decay of the shock front pressure with distance in the solid. Since a flat-topped wave in the gas impinges on the solid, the pressure at the interface is maintained at a value which is essentially constant for the duration of the flat-topped portion of the wave. When the expansion wave which is reflected from the driver end of the tube reaches the gas-solid interface, an unloading wave enters the crushed solid. Because of the hysteresis characteristic of the solid, this unloading wave in the crushed material can have a velocity substantially greater than that of the transmitted shock wave. The unloading wave thus tends to overtake the shock, thereby shortening the length of the wave in the solid. Eventually the pressure decay at the front, together with the overtaking unloading wave, would reduce the pressures below the crushing strength of the material and the wave would continue to propagate as an acoustic wave if the specimen were sufficiently long. In experiments using contact explosives or an explosive-driven plate against compressible solids, details of pressure decay are difficult to obtain; in future work with longer specimens in the strong shock tube it will be possible, using more extensive instrumentation, to assess pressure decays with distance in the specimens.

#### B. Methods of Analysis of Data

This section discusses alternate schemes which can be used to deduce the Hugoniot for compressible solid materials from shock tube measurements.

##### 1. Static and Dynamic Pressure-Volume Relationships

If the equation of state of the solid material were of the form  $P = f(v)$ , at least as far as the compression phase of loading is concerned,

then all (P-v) states which could be reached by compression would lie on a single curve in the P-v plane. Furthermore, the same states would be reached by isothermal, adiabatic, or shock compression. Then the Hugoniot for the material would coincide with the statically obtained pressure-specific volume curve. Assuming that these curves are not far different, the static curve can be used to predict roughly the reflected pressures  $P_5$ , for given incident pressures  $P_2$  by considering the argon to behave as a perfect gas. The pertinent relationships are presented in later paragraphs of this section. The results of calculations of this type were useful in planning the program of tests reported herein. The measured values of  $P_5$ , and  $P_2$  resulting from tests on a given material could then be superimposed on a plot of predicted reflected pressure  $P_5$ , as a function of incident pressure  $P_2$  obtained using the static pressure-volume data. Deviations of the experimental points from the curve on a chart of this type indicate the discrepancy between the Hugoniot and static (essentially isothermal) compression data.

Referring again to Diagram II and assuming uniform pressure and particle velocity profiles across regions 5" and 7, we write the condition for conservation of mass across the shock front in the crushing solid:

$$\rho_6 w_{76} = \rho_7 (w_{76} - U_7) \quad (2)$$

where the symbol  $\rho$  denotes density and  $w_{76}$  is the velocity of the transmitted wave. The subscripts refer to regions in the diagram. The jump condition for conservation of momentum gives

$$P_7 - P_6 = \rho_6 w_{76} U_7 \quad (3)$$

Across the contact surface we have  $P_5 = P_7$  and  $U_5 = U_7$ ; in addition,

$P_6 = P_1 = 1$  atmosphere and  $U_6 = U_1 = 0$ . From Eqs. (2) and (3) and from the conditions across the contact surface, we obtain

$$U_{5'} = \sqrt{P_1 v_6} \sqrt{\left(\frac{P_{5'}}{P_1} - 1\right) \left(1 - \frac{v_7}{v_6}\right)}, \quad (4)$$

where  $v = 1/\rho$ , and  $v_6$  is therefore the initial specific volume of the solid.

Static compression data define a relationship

$$P_{5'} = f(v_7)$$

at  $P_6 = 1$  atmosphere (see Fig. 10). Assuming perfect gas behavior to the left of the gas-solid interface, the particle velocities  $U_2$  and  $U_{5'}$  are related to the pressures  $P_2$  and  $P_{5'}$ , as follows:

$$\frac{|U_2 - U_1|}{A_1} = \frac{|U_2|}{A_1} = \left(\frac{P_2}{P_1} - 1\right) \sqrt{\frac{2}{(\gamma+1) \frac{P_2}{P_1} \frac{\gamma-1}{\gamma+1} + \frac{P_2}{P_1}}} \quad (\text{see Fig. 9A}), \quad (5)$$

$$\frac{A_2}{A_1} = \sqrt{\frac{1 + \frac{\gamma-1}{\gamma+1} \frac{P_2}{P_1}}{1 + \frac{\gamma-1}{\gamma+1} \frac{P_1}{P_2}}} \quad (\text{see Fig. 9B}), \quad (6)$$

$$\frac{|U_{5'} - U_2|}{A_2} = \frac{A_1}{A_2} \cdot \frac{|U_{5'} - U_2|}{A_1} = \left(\frac{P_{5'}}{P_2} - 1\right) \sqrt{\frac{2}{(\gamma+1) \frac{P_{5'}}{P_2} \frac{\gamma-1}{\gamma+1} + \frac{P_{5'}}{P_2}}} \quad (\text{see Fig. 9C}). \quad (7)$$

The symbol  $A$  denotes sound velocity in the gas, given by

$$A = \sqrt{\gamma R_o T/m}, \quad (8)$$

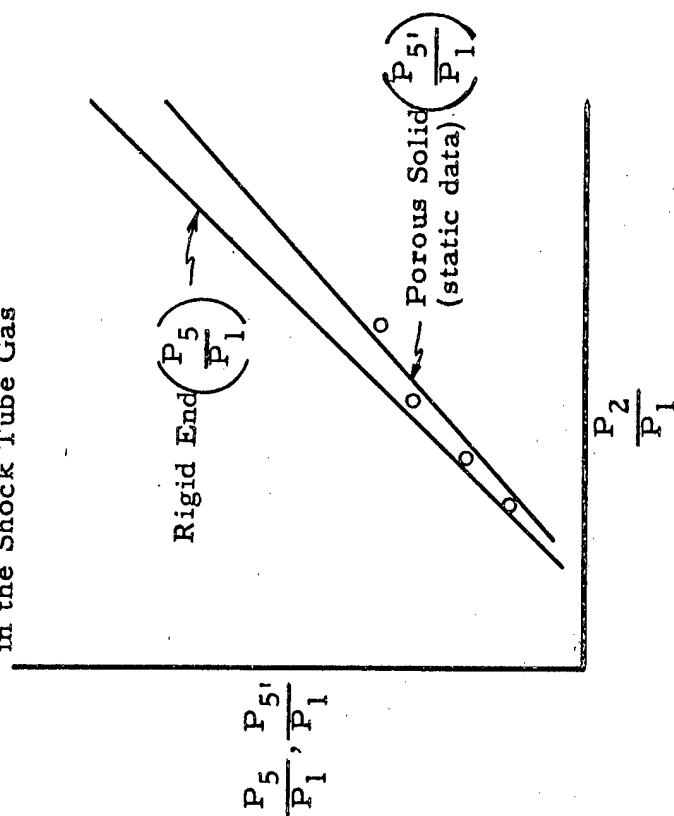
where  $T$  and  $m$  are the absolute temperature and molecular weight of the gas, and  $R_o$  is the universal gas constant. Equations (5), (6), and (7) are derived and numerical values are tabulated in Ref. 8 for  $\gamma = 5/3$ .



From Eq. (4) and the relationships indicated by Eqs. (5), (6), and (7), approximate values of  $P_{5'}$  were predicted for given values of the incident pressure  $P_2$ . The results are shown in Fig. 12. A schematic comparison of the pressures reflected from a compressible solid and from a rigid wall is shown in Diagram III. It is clear that for a given incident pressure  $P_2$  the pressure  $P_{5'}$  reflected from a compressible solid boundary does not differ drastically from the pressure  $P_5$  reflected from a rigid boundary. This is advantageous from the standpoint of test operation in which a priori order-of-magnitude information on the anticipated signals from the sensing equipment is useful. A typical calculation for the rough prediction of the reflected pressure  $P_{5'}$  based on static compression data is given in Appendix A.

The "flow patterns" postulated following shock impingement on the solid in the present analysis (i. e., constant states separated by shocks and contact discontinuities) are based on analogy to wave motion across regions of fluid of differing density. These flows are admissible in the sense that they satisfy the field equations for motion of continuous media and the appropriate boundary conditions. The analysis is an adequate representation of the physical situation when the pressure wave in the solid exceeds the crushing strength of the material. At lower pressures the shock is not necessarily a stable wave configuration, and a highly directional state of stress can be propagated through the solid together with more complicated wave forms. The present treatment is more or less conventional; a discussion of the assumptions involved in a fluid dynamic model of the solid is given in Ref. 4.

Display of Data  
as Measured  
in the Shock Tube Gas



Shock Tube Gas Measurements Reduced  
to Obtain  
Hugoniot of the Solid

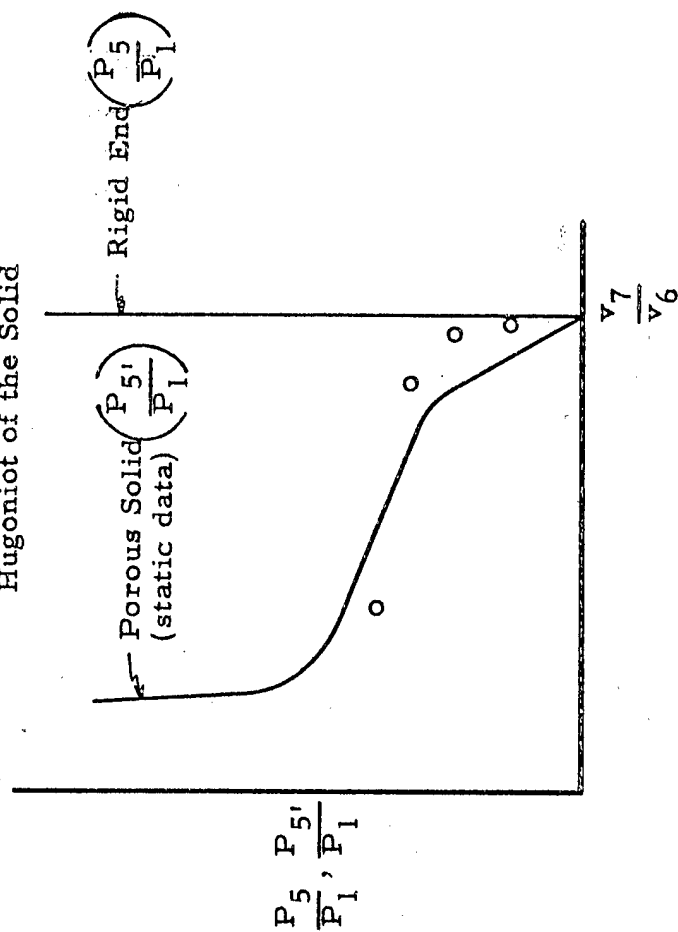


DIAGRAM III CORRELATION OF TYPICAL SHOCK COMPRESSION DATA POINTS

## 2. Derivation of the Hugoniot from Experimental Data

Equations (2) and (3) of the preceding section are the statements of conservation of mass and momentum across a shock. These jump conditions require the existence of a shock of constant thickness and hold irrespective of the equation of state of the material. The contact surface separating the gas and solid, across which pressure and particle velocity are continuous, is assumed to be a plane across which there is no transfer of mass. Equations (2) and (3) represent two relationships among the four unknown quantities  $P_7$ ,  $\rho_7$ ,  $w_{76}$ , and  $U_7$ . Assuming uniform pressure and particle velocity profiles in the solid and recalling the contact surface conditions  $P_{5'} = P_7$  and  $U_{5'} = U_7$ , one can, in principle, determine the Hugoniot  $P_{5'} = f(v_7)$  by experimental measurement of any pair of the four unknown quantities. Practically, the following four methods are possible for the determination of the Hugoniot:

1. Measure  $P_2$  and  $P_{5'}$ ,
2. Measure  $w_{76}$  and  $P_{5'}$ ,
3. Measure  $P_{5'}$  and  $U_7$
4. Measure  $P_7$  and  $\rho_7$

Method 1 is that employed in the present analysis. The measurement of the pressures  $P_2$  and  $P_{5'}$  by a sensor immediately upstream of the gas-solid interface leads to a determination of the particle velocity  $U_{5'}$  through Eqs. (5) through (8) (Figs. 9A, 9B, and 9C), assuming perfect gas behavior to the left of the interface. The initial length of the specimen is immaterial except to the extent that practical considerations in regard to the testing have to be satisfied. The shock tube, which utilizes compressed gas for shock generation, provides flat-topped free-stream waves followed by

fairly uniform flow and is ideally suited for these measurements. By inspection of Diagram III, it is clear that the reflected pressure  $P_5$ , will be rather insensitive to variations in the Hugoniot; correspondingly, there is inherent loss of precision in the determination of the Hugoniot from reflected pressure measurements. However, instrumentation is simple in that a single pressure record is taken in the gas to the left of the interface. A typical calculation of a point on the Hugoniot for celotex is given in Appendix B.

Method 2 requires the simultaneous measurement of pressure in the gas and shock velocity in the solid. Experimentally, this method requires more sophisticated instrumentation than Method 1, but the analysis is more direct in that the assumption of perfect gas behavior upstream of the solid is avoided. Inherent loss of precision in the determination of the Hugoniot is smaller in the analysis using this pair of measurements.

Method 3 involves the measurement of the shock-induced particle velocity in the solid and a simultaneous measurement of the pressure  $P_5$ . This can be accomplished by using a series of standard piezoelectric crystal pressure sensors mounted along the wall of the tube at and near the initial position of gas-solid interface. These sensors would be consecutively triggered by passage of the interface, providing a simultaneous measurement of reflected pressure and interface velocity. Again the assumption of perfect gas behavior is avoided, and again inherent loss of precision is smaller than in Method 1.

Method 4 would employ a direct measurement of the pressure in the solid together with the measurement of the final density. It would first have to be demonstrated that (1) the momentary high reflected pressure

$P_8$  to which the solid is subjected has little effect in further volume reduction after the first shock has traversed the specimen, and (2) volume recovery after unloading is either negligible or compensating. Although the method requires rather extensive preliminary experimentation to prove its validity, it would represent a quite convenient scheme for obtaining the gross features of the Hugoniot for a solid without resorting to extensive analysis.

It is planned to incorporate the latter three methods into further experiments on solids. In any event, it is desirable to introduce some redundancy into the measurements in order to furnish experimental checks on the consistency of the data and to improve accuracy in the determination of the Hugoniot. Once the shock velocity is related to the pressure by experiments on small specimens, it will be possible to obtain shock pressures in longer specimens solely by arrival time measurements.

#### IV. TEST RESULTS

In this section the gross features of the experimental data are discussed. The effects of variation of specimen material and specimen length are considered.

##### A. Film Records

The data obtained in the present study consist of oscilloscope traces recorded on film showing the time histories of pressure at three gage stations in the driven chamber. Visual observations were made of the test samples before and after exposure to shock; initial and final specimen lengths were recorded.

The pressure records were interpreted on the basis of Diagram I, Fig. 3, and the discussion in Section III-A of the present report. Figure 4

shows typical pressure-time histories at gage station 2 (62 tube diameters downstream of the diaphragm station) and at gage stations 3 and 4 (68 tube diameters downstream of the diaphragm station) for a redwood specimen. These latter two gages were mounted approximately 5/8 in. upstream of the face of the 6-in. specimen in a steel ring located between the tube proper and the sample holder. The gage at station 2 was used to obtain the incident pressure  $P_2$ . The gages at stations 3 and 4 sensed the same phenomena; the horizontal sweep speed of the oscilloscope displaying the output of the gage at station 3 was greater by a factor of 20 than that of the oscilloscope displaying the output of the gage at station 4. As indicated in Fig. 4, the gage record at station 4 thus has a compressed time scale, so that later wave phenomena are observed on this record.

It may be noted that the incident wave is nearly flat-topped, but that some attenuation of the shock front pressure due to wall friction and boundary layer phenomena is evidenced by the slight increase of pressure with time before the onset of the wave reflected from the solid. That the incident wave is not perfectly steep-fronted is due primarily to limitations on the response of the gage system and associated circuitry, and to a lesser extent to non-ideal gas effects.

#### B. Effect of Various Materials on Reflected Pressures

In Fig. 5 a comparison of the pressure records at gage stations 2 and 3 is given for the stationary end condition and for 6 in. specimens of chamber at the time of diaphragm burst (see Diagram I). The lowest reflected pressures  $P_5$ , resulted from celotex, the most compressible of the three materials. Higher reflected pressures resulted from sugar pine than from redwood, although the dynamic crushing strengths of the two woods

appear to be comparable.

The ratio of final to initial lengths for the shots shown in Fig. 5 ranged from 50 to 55 per cent in the case of celotex, from 50 to 53 per cent in the case of redwood, and from 64 to 69 per cent in the case of sugar pine. Because the samples compressed somewhat unevenly due to non-homogeneities, the maximum and minimum values of the final-to-initial length ratios are reported (see Fig. 8B).

#### 1. Stationary End Condition

In Fig. 6A are shown the pressure-time histories at gage station 3 with the specimen absent, the closed end of the tube presenting an essentially rigid boundary for normal reflection of the incident wave. Over the range of reflected pressures from 60 to 1800 psia, the total pulse duration is of the order of 5 milliseconds. At reflected pressures below 100 psia, the reflected wave is followed immediately by the expansion reflected from the driver end of the tube. At reflected pressures between 100 and 1500 psia, the reflected wave is essentially flat-topped for about 1.5 milliseconds. At reflected pressures above 1500 psia, the nearly constant reflected pressure persists for about 2 milliseconds before the onset of pressure relief.

Although the reflected pressures  $P_5$  in argon for given shock pressures  $P_2$  incident upon a rigid boundary are well predicted from perfect gas theory (Fig. 14A), the shots with the specimen absent serve to identify the properties of pressure waves which are generated as they are affected by the characteristics of the shock tube itself. That is, these shots serve as reference or calibration shots. For example, some attenuation of shock front pressure due presumably to wall friction and viscosity

effects in the gas is evidenced by the fact that the incident wave is not perfectly flat-topped; the gentle slope is magnified somewhat in the reflected wave.

Workers at Cornell Aeronautical Laboratory have reported results regarding wave attenuation in shock tubes<sup>9</sup> which are consistent with the phenomena displayed in Fig. 6A. Their results also show that helium or helium additive in the driver gas produces more nearly flat-topped waves than four other driver gases, including both non-combustible and combustible generation techniques. The attenuation effect increases with increasing shock strength; jump conditions hold locally across the shock front in any event however, and the pressures plotted in Fig. 14A are those immediately behind the incident and reflected wave fronts.

## 2. Celotex Samples

The pressure records at gage station 3 are shown in Fig. 6B for various initial driver pressures  $P_4$  with celotex specimens. The incident pressure  $P_2$  is sensed for only a fraction of a millisecond; this is the time of transit of the incident wave from the gage station to the face of the specimen plus that of the reflected wave back to the gage station. With the specimen absent (Fig. 6A), the incident pressure  $P_2$  is sensed for the time of transit of waves down the 6-in. sample holder to the rigid end and back again.

For a given incident pressure  $P_2$ , the pressure  $P_{5'}$  reflected from the surface of a sample is lower than the pressure  $P_5$  reflected from a rigid boundary whenever crushing occurs in the sample. When the shock strength is too low to result in crushing, the pressures  $P_{5'}$  and  $P_5$  are approximately equal. At the initial driver pressure of 3865 psia, the pressure



$P_5$ , is about 21 per cent less than the pressure  $P_5$  which would have been reflected from a rigid boundary. The pressures  $P_5$ , are seen to persist for times of the order of a millisecond, which roughly represents the time of transit of waves down the specimen and back to the gage station.

### 3. Redwood Samples

A comparison of Figs. 6A and 6C shows that at initial driver pressures somewhat higher than 1000 psia, the pressures reflected from redwood and from a rigid wall are nearly equal at about 800 psia. Inspection of the sample after testing at this pressure showed very little visible effect in terms of permanent deformation or surface erosion. At higher incident shock strengths, the reflected pressures  $P_5$ , were again lower than the corresponding rigid-wall reflected pressures  $P_5$ . At the initial driver pressure of 3865 psia, the reduction is again about 21 per cent. The pressures  $P_5$ , in the case of redwood persist for times of the order of 0.5 to 1 millisecond.

Visual inspection of the samples after testing showed that at the higher pressure loadings the surface erosion effects of high shock temperatures were noticeably increased. In some cases traces of brittle failure along slip planes were observed; there was also considerable splitting and splintering of the specimens.

### 4. Pine Samples

At the initial driver pressure of 1040 psia, the pressures reflected from sugar pine (Fig. 6D) and from a rigid wall (Fig. 6A) are again nearly equal at about 800 psia, and no significant permanent deformation of the specimen is evidenced. At higher shock strengths, the pressures  $P_5$ , reflected from sugar pine are somewhat higher than the pressures

reflected from redwood for the same incident pressures  $P_2$ . At the initial driver pressure of 3840 psia, the pressure  $P_{5'}$  is about 12 per cent less (in comparison to 21 per cent in the case of redwood and celotex) than the corresponding rigid-wall reflected pressure  $P_5$ . The pressures  $P_{5'}$  again persist for times of the order of 0.5 to 1 millisecond.

Inspection of the samples after testing showed traces of splitting and brittle failure along slip planes, but the samples exhibited no splintering as encountered in redwood.

### C. Effect of Specimen Length

A series of shots were fired at initial driver pressures in the neighborhood of 1000 psia with specimens of celotex, redwood, and sugar pine ranging in nominal length from zero (specimen absent) to 6 in. This section summarizes some observations on the pressure-time histories at gage station 3 located immediately upstream of the sample holder. Over the range of specimen length up to 6 in., the gross features of the phenomena are essentially independent of the sample length in that the same series of pressure levels shown schematically in Diagram I is sensed at gage station 3. That is, the incident pressure  $P_2$ , the reflected pressure  $P_{5'}$ , the pressure  $P_{5''}$  transmitted into the gas from the solid, and the expansion wave reflected from the driver end of the tube are exhibited on the pressure records. In the case of the longest specimens, the expansion reflected from the driver end appears before the pressure  $P_{5''}$  as discussed in Section III-A of the present report.

The use of a shorter specimen is equivalent to moving the pressure gage (see Diagram I) farther upstream of the gas-solid interface, since the time and distance scales in Diagram I are immaterial as long as the

pressure reflected from the specimen appears at the gage before the expansion from the driver end of the tube. With the shorter specimens, the incident pressures  $P_2$  are sensed for longer periods of time and the reflected pressures  $P_5$  persist for shorter periods of time before the pressures  $P_{5''}$  appear.

With celotex specimens (see Fig. 7A), initial driver pressures of about 1000 psia produce reflected pressures  $P_5$ , from 700 to 750 psia. In the case of the nominal 6-in. specimen, the pressure  $P_{5''}$  does not appear. The pressure  $P_5$  persists for about a millisecond in the case of the nominal 4-in. specimen and for about 0.5 millisecond in the case of the 2-in. specimen. It is interesting that the pressures  $P_{5''}$ , where they appear, are quite close to the pressure  $P_5$  reflected from a rigid boundary at corresponding times after arrival of the incident shock at the gage.

For redwood samples (see Fig. 7B), the shock waves generated by initial driver pressures somewhat higher than 1000 psia are just sufficient to induce a small amount of crushing in the specimens. The reflected pressure  $P_5$  is about 750 psi, and is sensed for progressively shorter durations as the length of the specimen is decreased.

The reflected pressures produced by initial driver pressures near 1000 psi are apparently about equal to the dynamic crushing strength of sugar pine (see Fig. 7C). A negligible amount of permanent deformation was evidenced on visual post-test inspection of the specimens, and the pressures reflected from the gas-solid interface are about the same as those reflected from a rigid boundary.

## V. ANALYSIS OF RESULTS

The experimental data described in the preceding section were used to obtain points on the Hugoniot for the solid materials tested.

### A. Predictions and Results Regarding Reflected Pressures

Approximate values of the pressure  $P_5$ , reflected from the surface of the solid specimen were calculated following the assumptions and procedure discussed in Section III-B-1 of the present report. Confined static compression data for celotex, redwood, and sugar pine were taken from Ref. 1. The curves are reproduced in Fig. 10 of the present report. These essentially isothermal pressure-specific volume loci were considered as approximating the Hugoniot for purposes of the calculation. The approximate predictions of reflected pressures  $P_5$ , for various incident pressures  $P_2$  were compared with the pressures  $P_5$  given by Eq. (1) which result from reflection of the incident pressures  $P_2$  from a rigid boundary. An example of the stepwise calculation for a specimen of celotex with  $P_2/P_1 = 18.4$  is given in Appendix A. Curves of predicted interface velocity  $U_5$ , as a function of  $P_5$ , for the three materials (i. e., the plots of Eq. (4) incorporating static compressibility data) are shown in Fig. 11. Curves of predicted reflected pressure as a function of incident pressure for each of the three materials and for the rigid boundary are shown in Fig. 12. The reflected pressures of celotex, the most compressible of the materials, are hence the lowest anticipated. These are followed in order by redwood and sugar pine.

The pressure  $P_5$  reflected from a rigid boundary is shown as a function of the incident pressure  $P_2$  in Fig. 14A. The solid line is a plot of Eq. (1) and the experimental points are superimposed. The

approximate predictions of the reflected pressure  $P_5$ , as a function of  $P_2$  for celotex, redwood, and sugar pine are repeated in Figs. 14B, 14C, and 14D, respectively. The plot of Eq. (1) and the experimentally obtained pairs of  $P_2$  and  $P_5$ , are also shown in each figure.

The experimentally obtained reflected pressures  $P_5$  from a rigid wall (Fig. 14A) lie roughly within 10 per cent of the theoretical values. Reflected pressures up to about 120 atmospheres were recorded.

Celotex specimens (Fig. 14B) were subjected to reflected pressures  $P_5$ , well above the static compressive strength of the material. The crushing strength of a specimen in confined static compression is defined by a shoulder or "yield point" in the static pressure-specific volume curve (Fig. 10). For celotex, the yield point is too low to be identified clearly on the scale of pressures in Fig. 10. The experimental points in Fig. 14B fall between the rigid wall reflected pressures and the rough predictions based on the static pressure-specific volume curve.

Inspection of Fig. 10 shows that the yield point for redwood in confined static compression is of the order of 1500 psia. At the lower incident pressures, it is seen from Fig. 14C that the resulting reflected pressures are about the same as those reflected from a rigid boundary. At the higher incident pressures, the reflected pressures are apparently in the neighborhood of the dynamic crushing strength of the material, and these pressures are lower than those reflected from a rigid boundary.

From Fig. 10, the yield point for sugar pine in confined static compression is of the order of 2500 psi. Thus the specimens in the shock tube tests were subjected to pressures  $P_5$ , lower than the static crushing strength. However, a significant amount of permanent deformation, due

presumably to successive traversal of the specimen by high reflected pressures, was evidenced in the tests at higher pressures. Correspondingly, Fig. 14D shows that the higher incident pressures resulted in reflected pressures somewhat below those reflected from a rigid boundary.

Initial and final lengths of the specimens were recorded after visual post-test inspection. Permanent deformation was not perfectly uniform over the cross-sectional area of the specimen, so that maximum and minimum values of the final or crushed length were noted in each case. The entire collection of experimental data for celotex, redwood, and sugar pine is displayed in Figs. 15A, 15B, and 15C. These are charts of pressure versus final-to-initial length ratio. For each test, the pressures  $P_{5'}$  and  $P_{5''}$  (see Diagram I) and the maximum and minimum length ratios are plotted. The corresponding static pressure-specific volume curve is repeated on each chart for the sake of completeness. It should be emphasized that these charts serve only to display the experimental data. No particular physical significance can be attached at this time to the loci of the experimental points, since the final length of a specimen after testing and removal from the sample holder is a function of the entire time history of stress to which it has been subjected. It was pointed out in Section II-A that, following shock impingement, a complicated sequence of compression and expansion waves traverse the specimen, the stress history being dependent in part on the characteristics of shock generation in the tube. It is possible that successive reflections of waves may have little effect in the way of further volume reduction after the initial shock, and that volume recovery upon unloading may be either negligible or compensating. If these conditions can be shown to be essentially true, the loci of such experimental points could

be used directly to determine at least the gross features of the Hugoniot for a given solid.

#### B. Results Regarding the Hugoniot for Solids

Points on the Hugoniot curves for celotex, redwood, and sugar pine were obtained using the experimentally obtained incident pressures  $P_2$  and reflected pressures  $P_5$ , in conjunction with the assumptions and procedure outlined in Section III-B-2 (Method 1) of the present report. Each test thus yields a single point on the Hugoniot for a given material. An example of the calculation for a specimen of celotex with  $P_2/P_1 = 18.4$  is given in Appendix B. The average initial weight densities of the specimens tested were found to be  $17.3 \text{ lb/ft}^3$  in the case of celotex,  $24.1 \text{ lb/ft}^3$  in the case of redwood, and  $22.2 \text{ lb/ft}^3$  in the case of sugar pine. Points on the Hugoniot derived from the experimental data for celotex, redwood, and sugar pine are shown in Figs. 16A, 16B, and 16C, respectively. The corresponding static compression curve is shown on each chart for purposes of comparison.

In the case of celotex (Fig. 16A), points on the Hugoniot from all tests lie above the static compression curve. The dynamic crushing strength of the material appears to be of the order of 1000 psia. Considerable scatter is evidenced in the data.

Except for points resulting from tests at the lowest shock strengths, points on the Hugoniot for redwood (Fig. 16B) lie below the static compression curve. Apparently the crushing strength of redwood in dynamic compression is somewhat lower than its yield point in confined static compression. The dynamic crushing strength of redwood appears to be of the order of 1200 psia.

Interesting behavior is exhibited in the case of sugar pine (Fig. 16C). Points on the Hugoniot lie well below the static compression curve, except for tests at the lowest shock strengths. The dynamic crushing strength of the material appears to be of the order of 1400 psia. Although the reflected pressures  $P_5$ , are all in the neighborhood of the dynamic crushing strength, large changes of specific volume in shock are deduced. Since only small amounts of permanent deformation were observed in the range of testing reported herein, it is evident that hysteresis in sugar pine under shock loading conditions is not as pronounced as that in redwood and celotex.

The experiments reported herein are preliminary in the sense that they were conducted over a rather limited range of incident shock pressures for the purpose of demonstrating the capabilities of the shock tube as a tool for obtaining the properties of certain solids in dynamic compression. Certain trends in the Hugoniot for these materials have been identified. It should be remembered, however, that we are dealing with substances whose equations of state may be quite complex. In other words, it is likely that the detailed thermodynamic state of the material is not completely described simply by the specification of, say, a pair of state variables. Such a description may be possible at extreme pressures and temperatures, where the material behaves as an essentially homogeneous fluid. For some applications, however, it is sufficient to work with a limited number of certain average quantities which may be considered as describing the state of the substance to within some required degree of accuracy. In the present experiments and analysis, we make use of the fundamental conservation laws in conjunction with assumptions in regard to pressure and



velocity profiles in the solid specimen. These assumptions are drawn from experience with wave motion in fluids, and the postulated flows satisfy the field equations for motion of continuous media without reference to an equation of state.

It is interesting to note that in the case of redwood and sugar pine, points on the Hugoniot in the region investigated lie below the presumably isothermal static compression data. While a certain amount of error is inherent in the determination of the specific volume in single shock using the experimental measurement of the pressures  $P_2$  and  $P_5$ , in connection with the assumption of perfect gas behavior in the argon (see Section III-B-2), the pressure  $P_5$  at the interface is that measured directly by the sensor upstream of the specimen. One might expect the pressure at the shock front in the solid to be somewhat lower, if anything, than the pressure at the interface, because of energy dissipation at the front. This would lead to points on the Hugoniot still farther below the isotherm than indicated in Figs. 16B and 16C.

Jump conditions hold across the wave front in the solid to the extent that the front is a quasi-stationary region. That is, the zone of transition from the initial state to the equilibrium state following shock is assumed to be a zone of steady flow relative to the motion of the front; thus the wave front need not be infinitely steep as far as application of the jump conditions is concerned.

In further experimental work on solids in the shock tube, resolution of pressure-time oscilloscope traces is being improved by the addition of a D.C. bias to magnify fluctuations in the traces, thereby providing more detail on the records. In addition, oscilloscope traces are now being recorded

on Polaroid transparencies which make possible enlargement and consequent improved data reduction.

## VI. CONCLUSIONS

The shock tube is a useful tool for the determination of the Hugoniot for crushable solid materials by shock impingement experiments. Assuming perfect gas behavior in the driven chamber gas, it is possible to deduce the particle velocity, density, and wave velocity in the solid following shock. The sole measurement necessary is the pressure-time history in the driven gas immediately upstream of the gas-solid interface. Solid specimens can easily be subjected to pressures of the order of 2000 psia using non-combustible driver gas and an initial driven gas pressure of 1 atmosphere. With combustible driver gas, pressures up to 20,000 psia on the specimen can be reached by initial pressurization of the driven gas to 10 atmospheres (see Appendix C).

In the present study, specimens of celotex, redwood, and sugar pine were subjected to reflected pressures up to 120 atmospheres. Because motion is induced in the solid as a result of shock impingement, these pressures are considerably lower than those which would result from normal reflection of the same shock waves from a rigid wall. Pressure reductions up to 21 per cent of the corresponding rigid-wall reflected pressures were noted in the case of celotex and redwood.

Points on the Hugoniot for celotex, redwood, and sugar pine were obtained from the present experiments. Rather large volume changes are attained in shock at pressures in the neighborhood of the crushing strength of the materials. In the case of celotex, points on the Hugoniot lie above the statically obtained pressure-specific volume curve. Points on the

Hugoniot for redwood and sugar pine lie below the corresponding static compression curves. The crushing strength of celotex in shock appears to be of the order of 1000 psia, that of redwood about 1200 psia, and that of sugar pine in the neighborhood of 1400 psia. In general, there seem to be significant differences between the static and dynamic crushing strengths of these three materials.

## VII. RECOMMENDATIONS

The results of shock impingement experiments described in the present report give rise to the following recommendations for improved operation, some of which are being incorporated into further work presently being undertaken in the strong shock tube at Armour Research Foundation.

1. Because the calculation of points on the Hugoniot of a solid specimen from experimental pressure-time data in the driven gas is quite sensitive to small variations in reflected and incident pressures, further tests should be performed with improved pressure resolution. This can be accomplished by electrically subtracting a portion of the signal from the sensor and amplifying the remainder.

2. In order to make possible a better determination of the Hugoniot, some redundancy should be introduced into the experimental data by the additional direct measurement of particle velocity and wave velocity in the solid sample. These measurements can be made by lines of pressure sensors and pressure "switches" mounted along the solid specimen.

3. The pressure range of the experiments should be extended through initial pressurization of the driven gas in order to obtain more information on the Hugoniot for the solids tested in the present study.

4. The effect of a variation in support conditions on the final length of the specimen should be investigated. That is, rather than backing up the specimen with the rigid steel blind end flange, more compressible backup materials can be used downstream of the specimen. In this connection, the specimen itself can be lengthened to the point where shock pressure attenuation is observable. Once the Hugoniot for the material is established from tests on shorter specimens, pressure decays in long specimens can be assessed solely by wave velocity measurements.

5. Tests should be undertaken on specimens of other crushable materials, such as foamed ceramics and foamed plastics. Testing techniques have to a great extent been routinized so as to permit rapid evaluation of a variety of materials.

6. It would also be of interest to observe the effect of various driven gases on specimens. During the present study, a small amount of charring of some specimens was noted, due presumably to high shock temperatures and chemical reaction with entrained air. With a combustible solid material and a driven gas other than one of the noble gases, one would expect more extensive charring and perhaps ignition. If these considerations were to assume importance, such conditions could be avoided in applications by the use of non-combustible crushable solids as blast-absorbing materials.

## BIBLIOGRAPHY

1. Porzel, F. B. Design Evaluation of BER (Boiling Experimental Reactor) in Regard to Internal Explosions, ANL 5651, ARF No. D090, Argonne National Laboratory Subcontract No. W31-109-eng-38-596, Armour Research Foundation (June 1956)
2. Zaker, T. A. Point Source Explosion in a Solid, Report No. ARF 4132-6, U. S. Atomic Energy Commission Contract No. AT(11-1)-528, Armour Research Foundation (November 1958)
3. Napadensky, H. S., and R. H. Stresau. A Technique for the Observation and Measurement of the Behavior of Porous Materials When Rapidly Compressed, Report No. D132D11-1, U. S. Atomic Energy Commission Contract No. AT(11-1)-528, Armour Research Foundation (August 1958)
4. Rice, M. H., R. G. McQueen, and J. M. Walsh. "Compression of Solids by Strong Shock Waves," Solid State Physics 6, 1 - 63, F. Seitz and D. Turnbull, ed., Academic Press, Inc. (1958)
5. Benedek, G. B. Deduction of the Volume Dependence of the Cohesive Energy of Solids from Shock Wave Compression Measurements, Technical Report No. 286, Office of Naval Research Contract No. Nonr-1866(16), Harvard University (November 1958)
6. von Karman, T. On the Propagation of Plastic Deformation in Solids, NDRC Progress Report No. A-29, OSRD No. 365, Office of Scientific Research and Development (January 1942)
7. Glass, I. I. Shock Tubes. Part I: Theory and Performance of Simple Shock Tubes, UTIA Review No. 12, Institute of Aerophysics, University of Toronto (May 1958)
8. Rudinger, G. Wave Diagrams for Nonsteady Flow in Ducts, D. Van Nostrand Co., Inc., New York (1955)
9. Witliff, C. E., and M. R. Wilson. Shock Tube Driver Techniques and Attenuation Measurements, Report No. AD-1052-A-4, U. S. Air Force Contract No. AF18(603)-10, Cornell Aeronautical Laboratory, Inc. (August 1957)

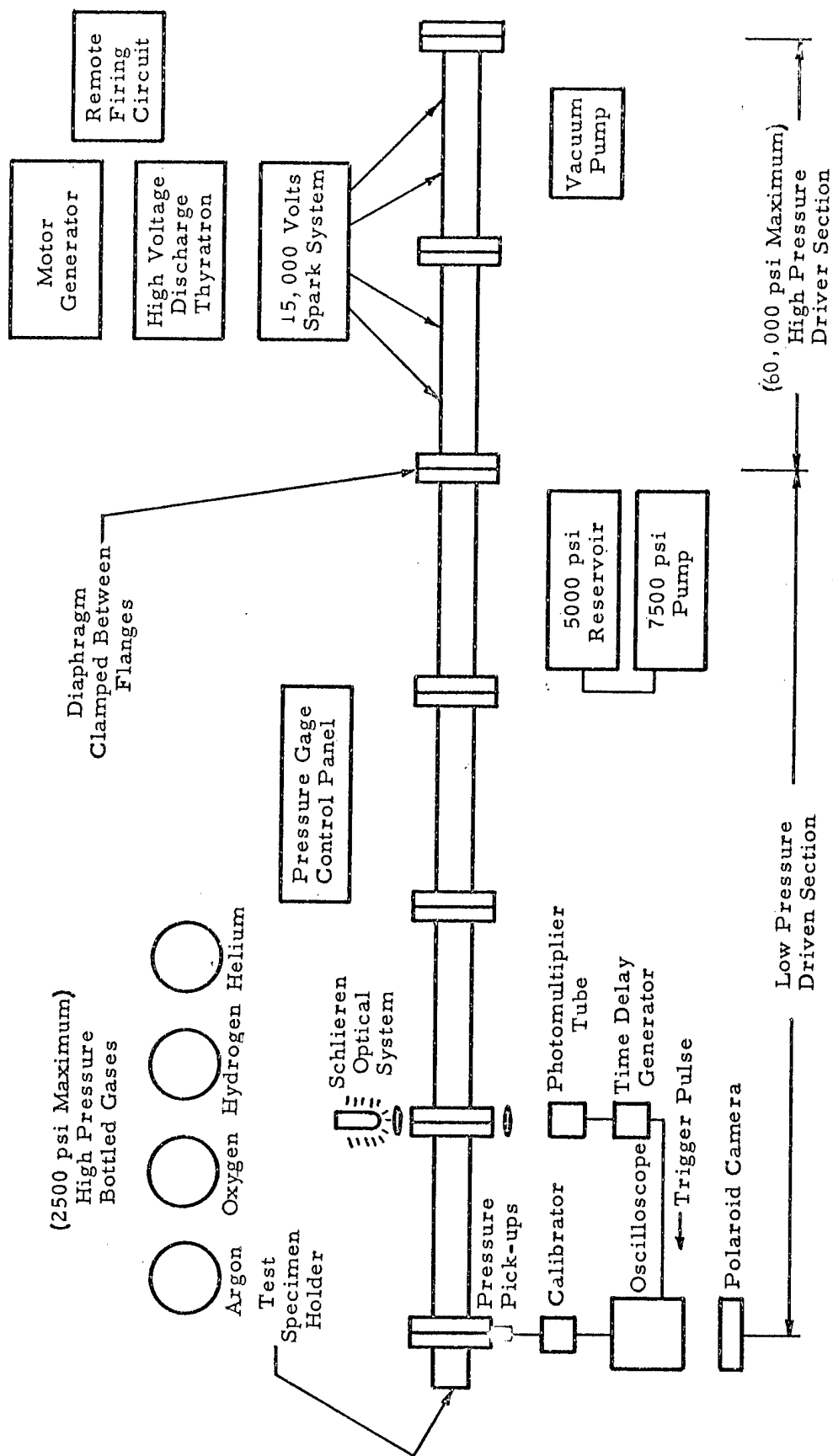


Fig. 1 SCHEMATIC OF SHOCK TUBE FACILITY FOR CRUSHING  
REACTOR BLAST SHIELD MATERIALS

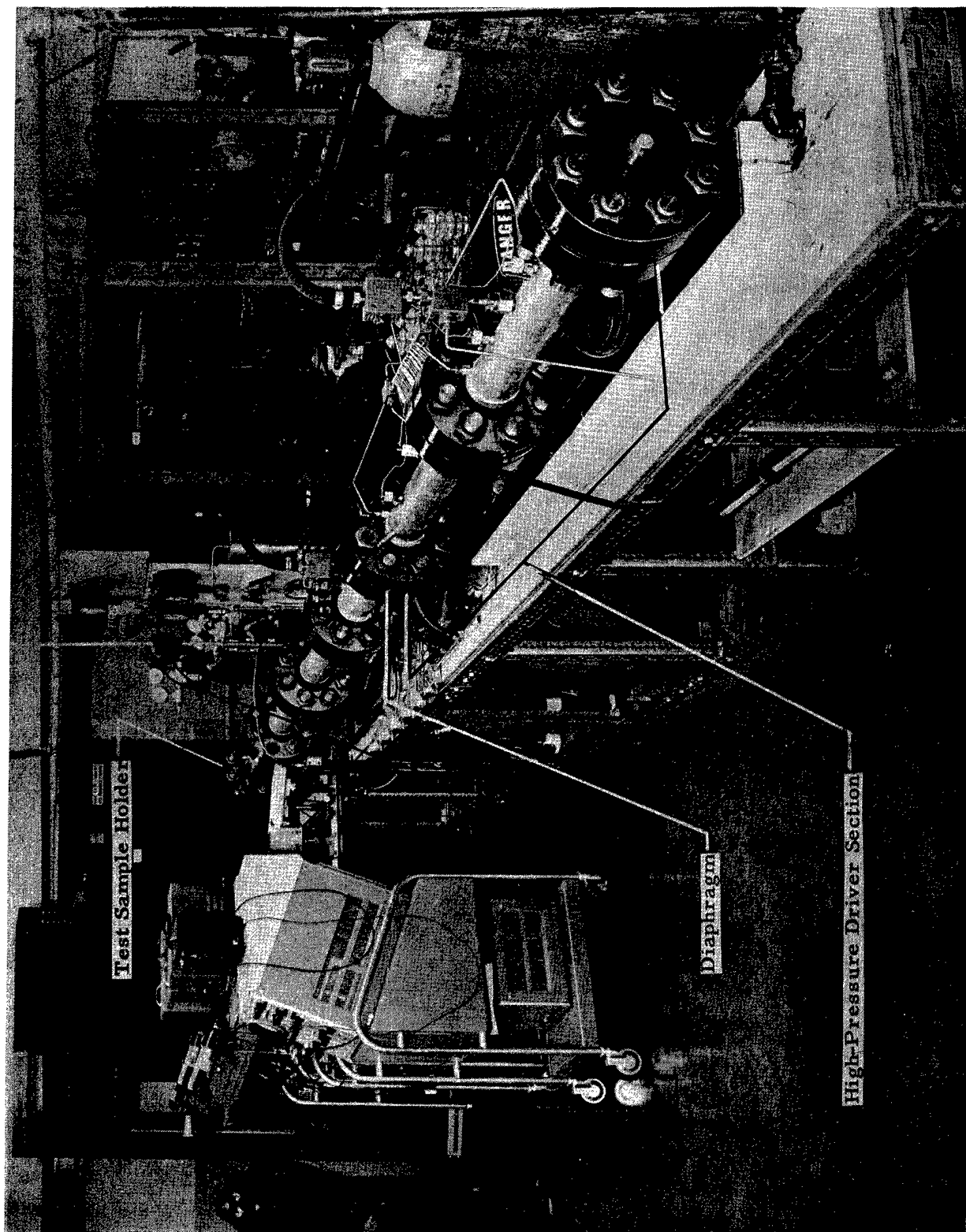


Fig. 2A PHOTOGRAPH OF SHOCK TUBE FACILITY - OVER-ALL

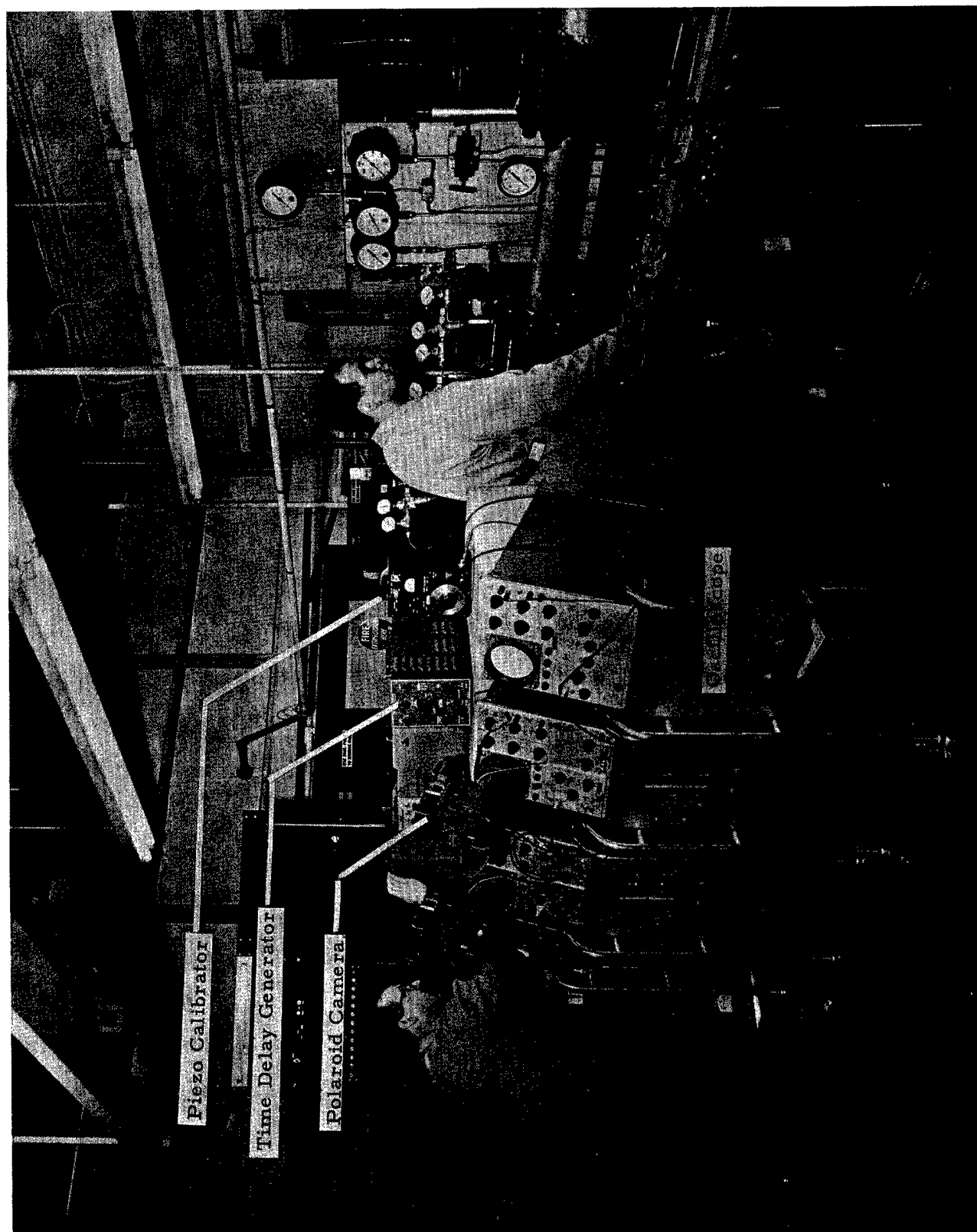


Fig. 2B PHOTOGRAPH OF SHOCK TUBE FACILITY - RECORDING INSTRUMENTATION



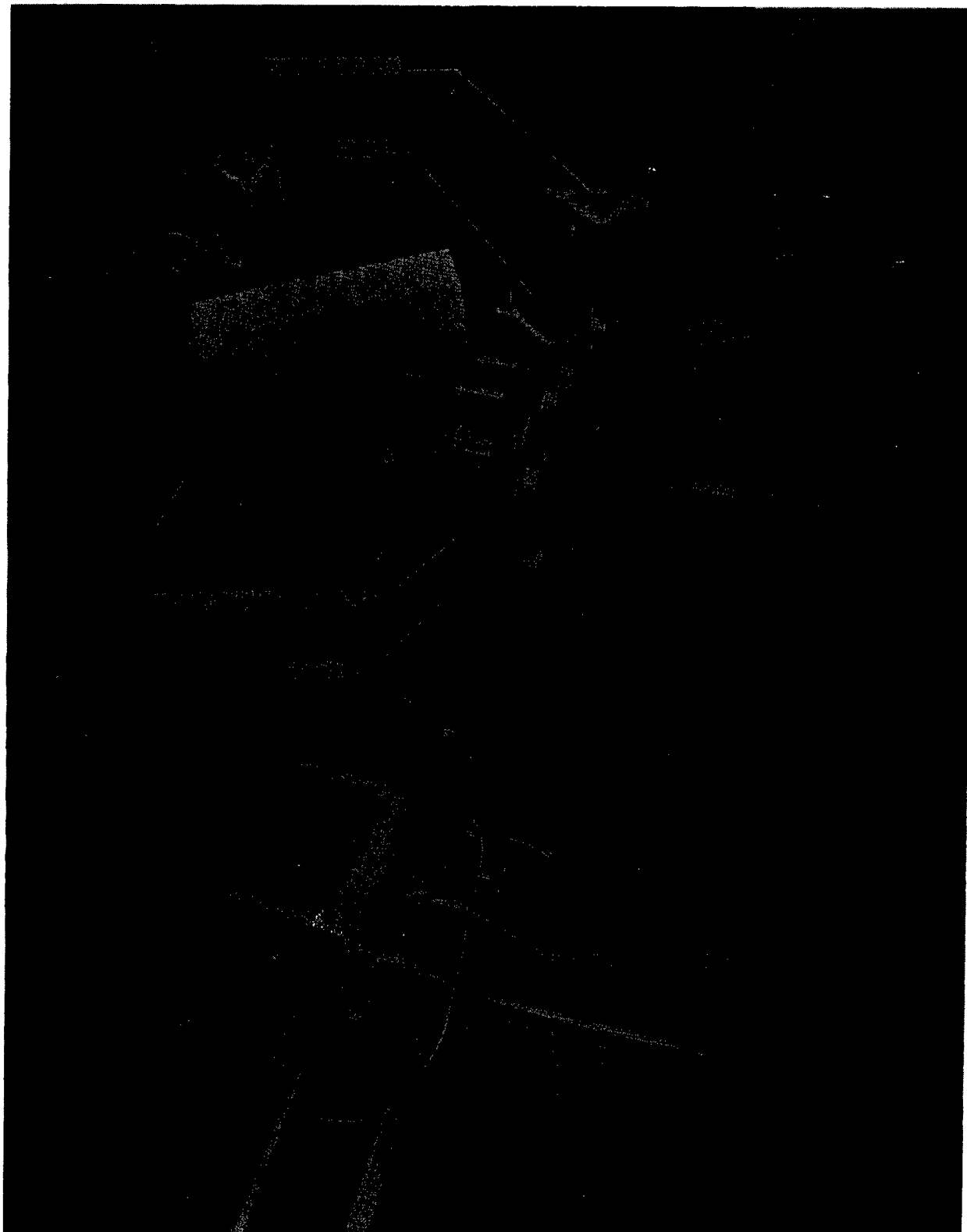


Fig. 2C PHOTOGRAPH OF SHOCK TUBE FACILITY - SCHLIEREN  
OPTICAL TRIGGERING SYSTEM

ARMOUR RESEARCH FOUNDATION OF ILLINOIS INSTITUTE OF TECHNOLOGY

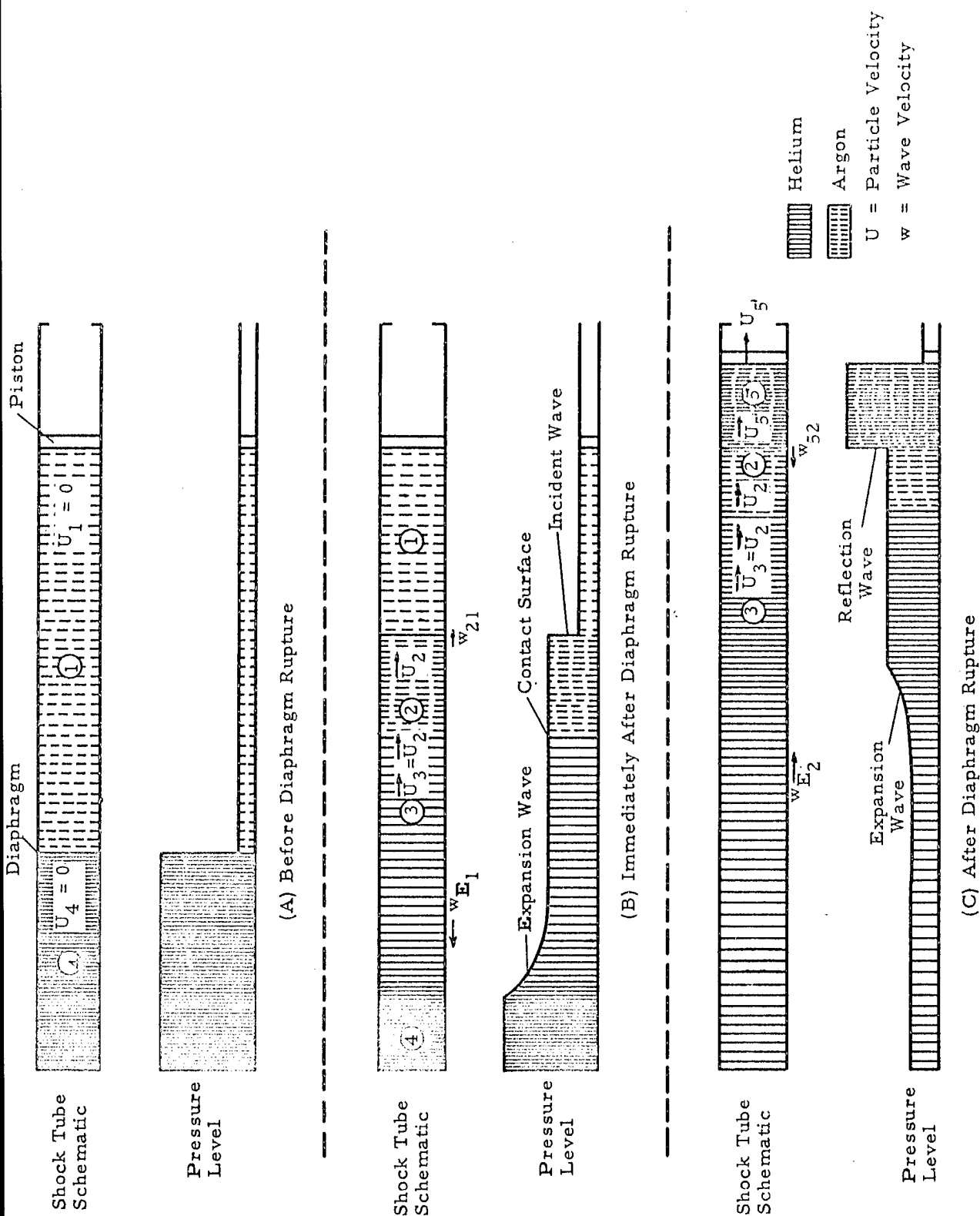


Fig. 3 PRESSURE DISTRIBUTION THROUGHOUT THE SHOCK TUBE  
AT VARIOUS TIMES

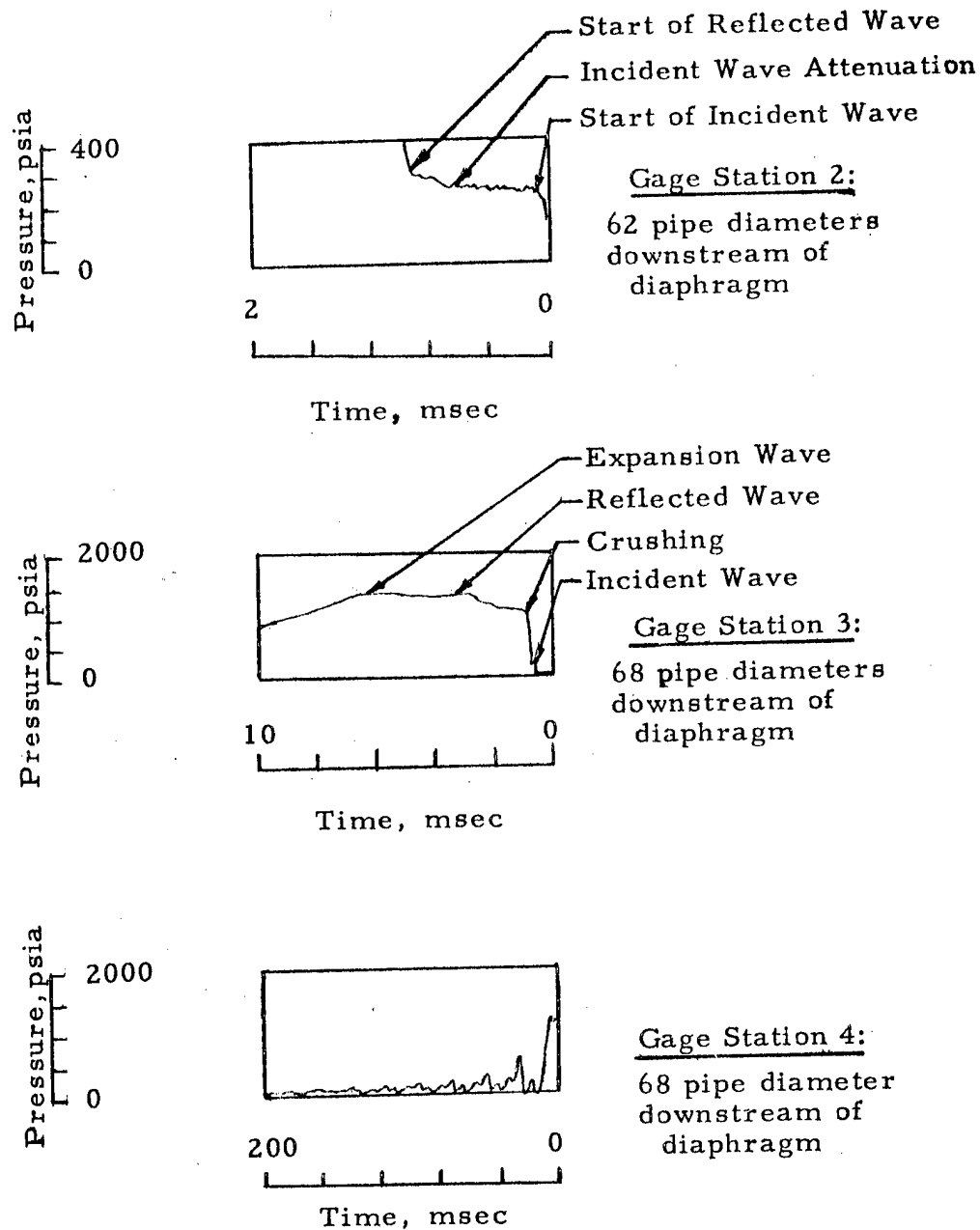
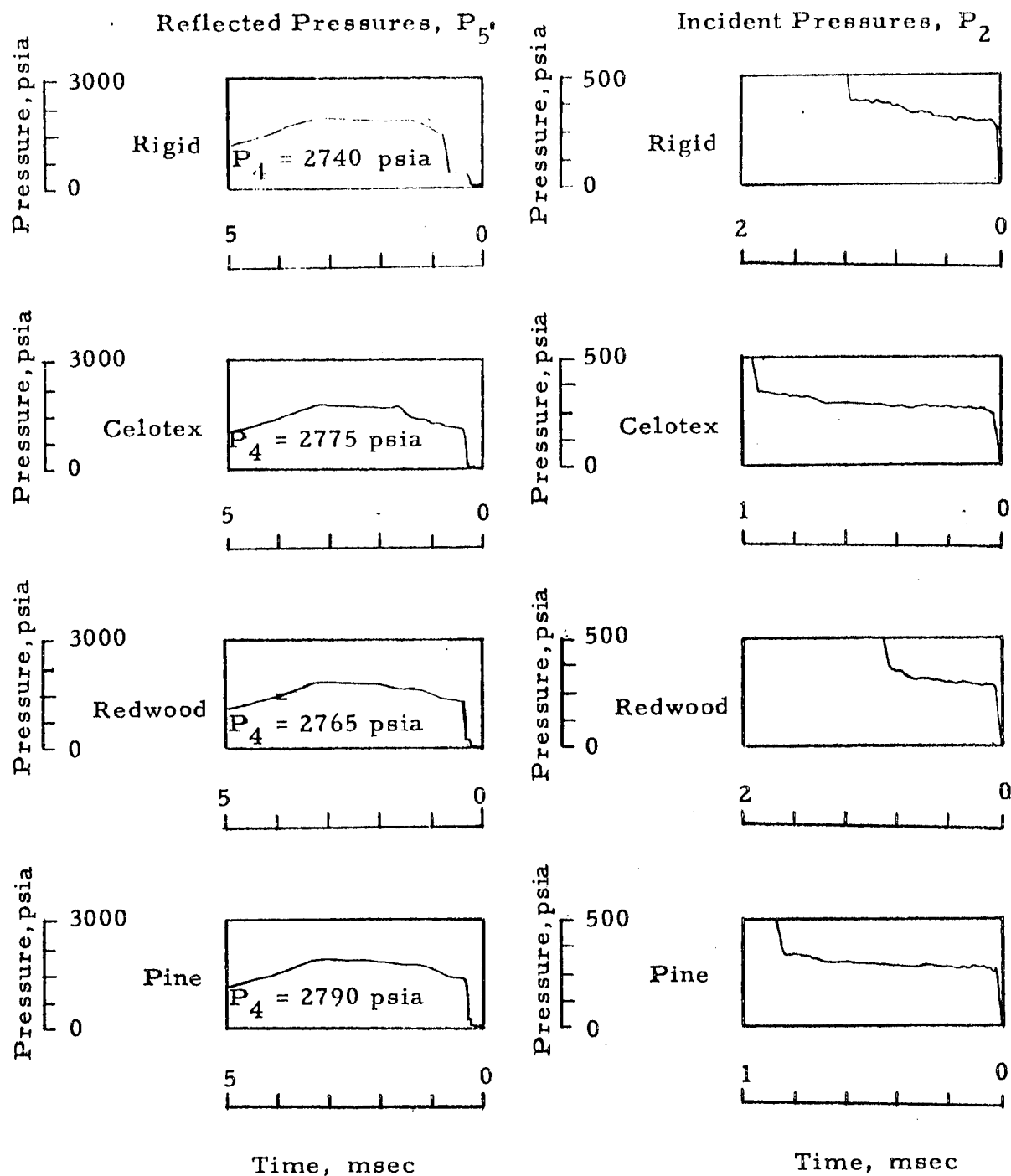
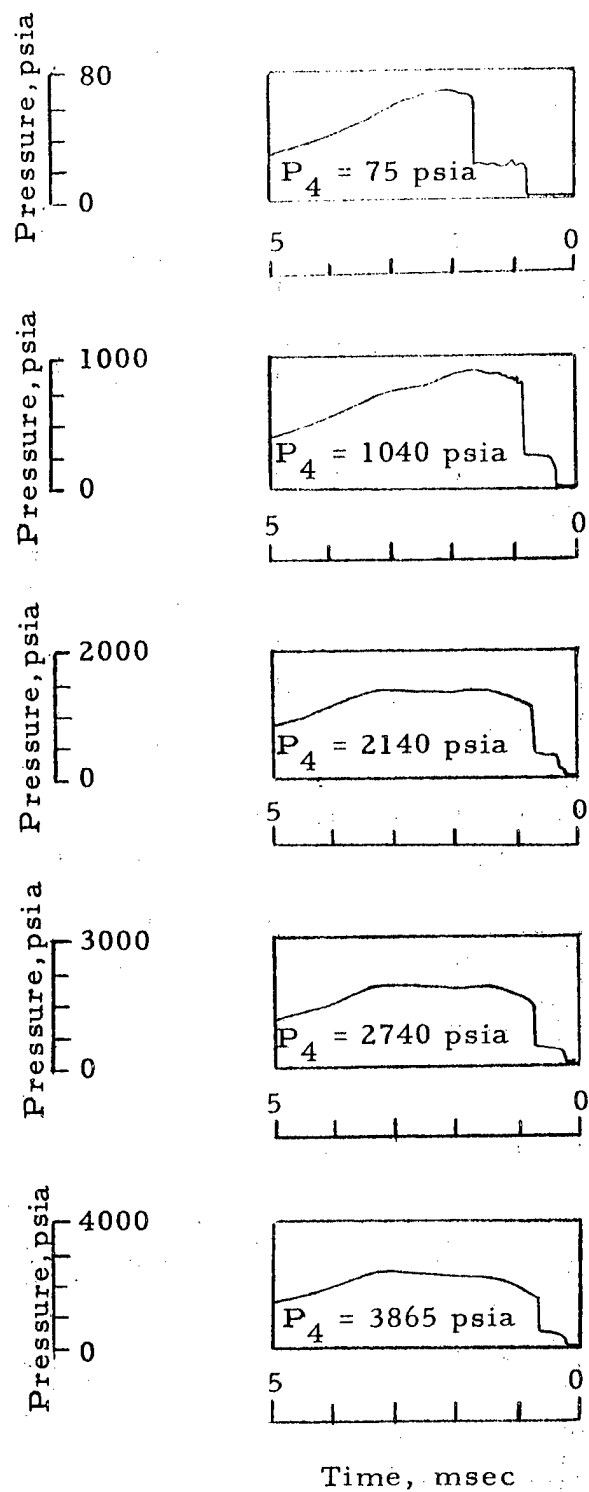


Fig. 4 TYPICAL INCIDENT PRESSURE VERSUS TIME HISTORIES AT TWO STATIONS DOWNSTREAM OF RUPTURED DIAPHRAGM (REDWOOD SPECIMEN)



**Fig. 5 REFLECTED PRESSURES OF RIGID SAMPLE HOLDER, CELOTEX, REDWOOD, AND SUGAR PINE**



**Fig. 6A REFLECTED PRESSURES OF RIGID SAMPLE HOLDER**  
**AT VARIOUS PRESSURES**

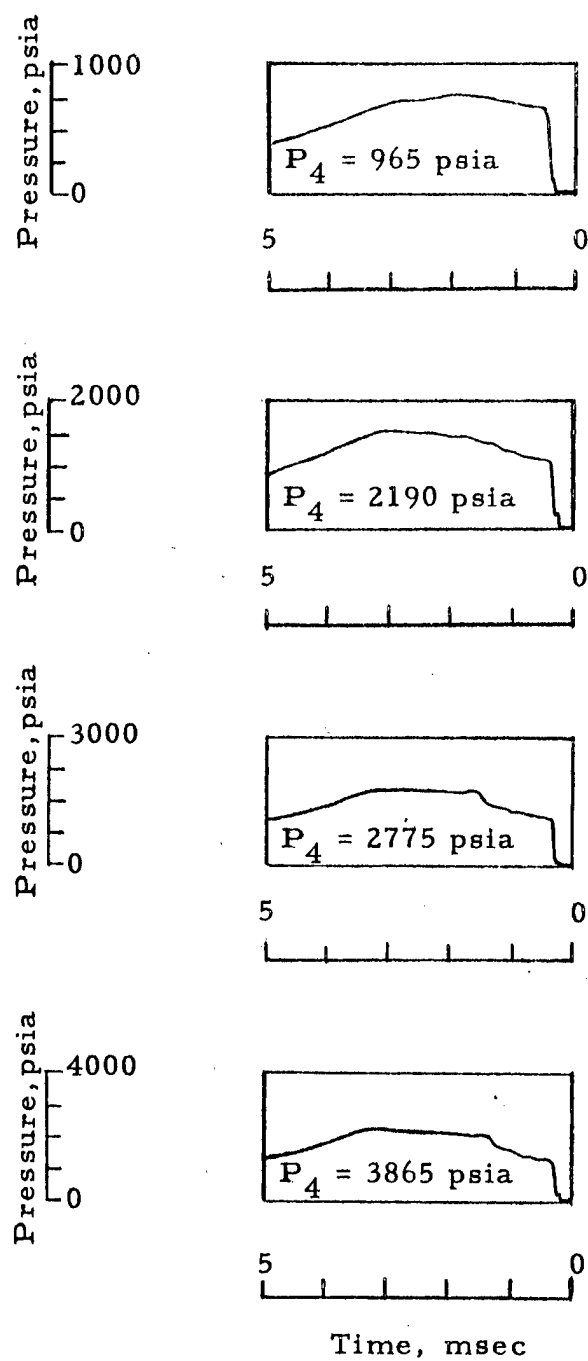


Fig. 6B REFLECTED PRESSURES OF CELOTEX AT VARIOUS PRESSURES

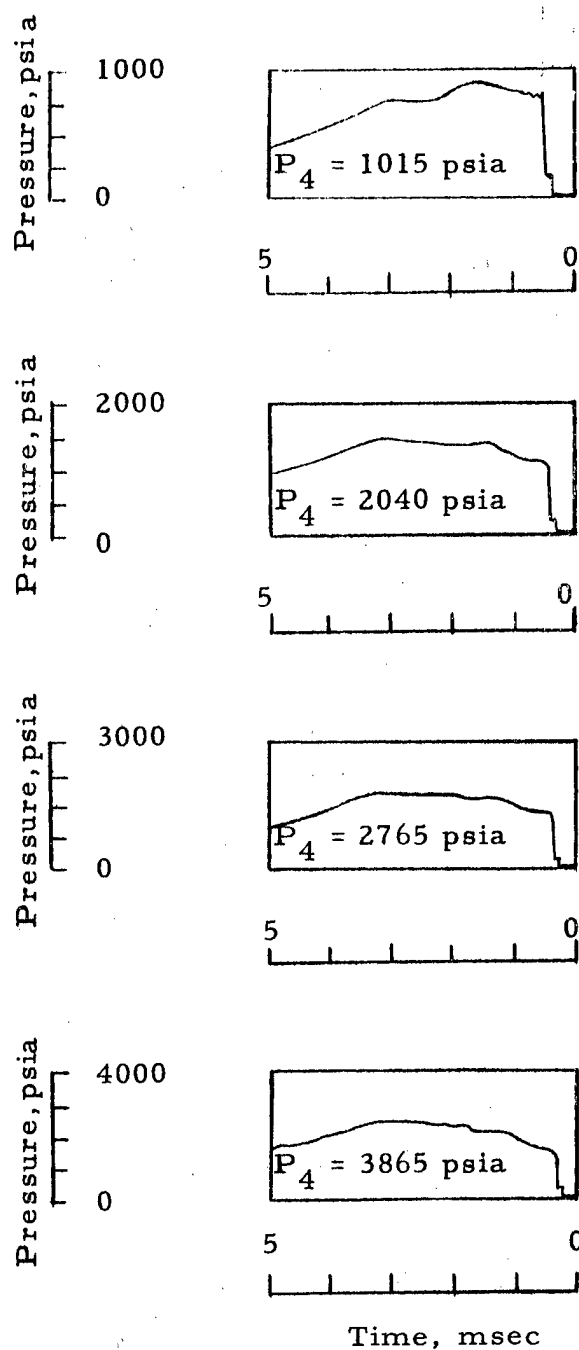


Fig. 6C REFLECTED PRESSURES OF REDWOOD AT VARIOUS PRESSURES

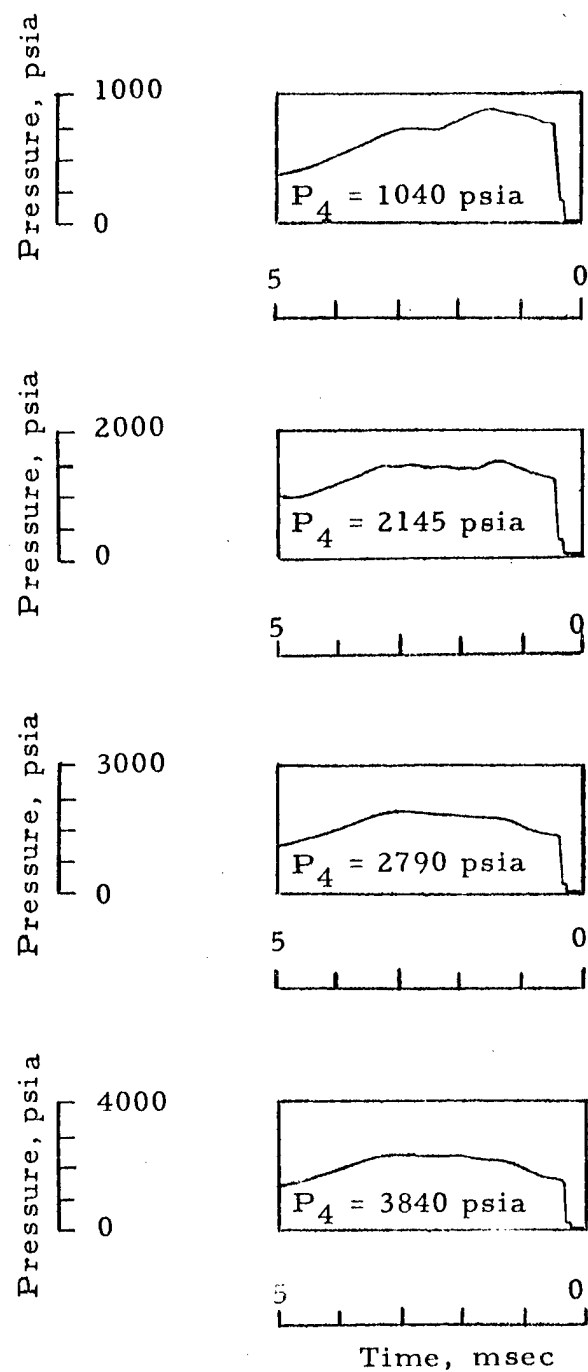


Fig. 6D REFLECTED PRESSURES OF SUGAR PINE  
AT VARIOUS PRESSURES



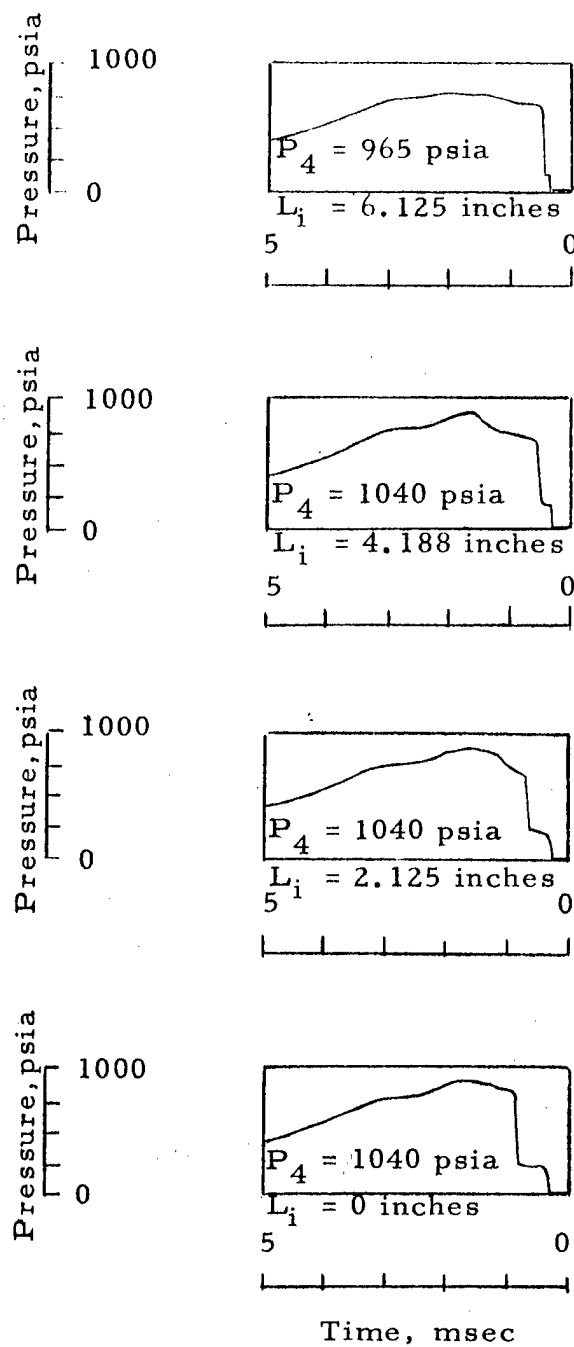


Fig. 7A REFLECTED PRESSURES OF VARIOUS LENGTHS OF CELOTEX

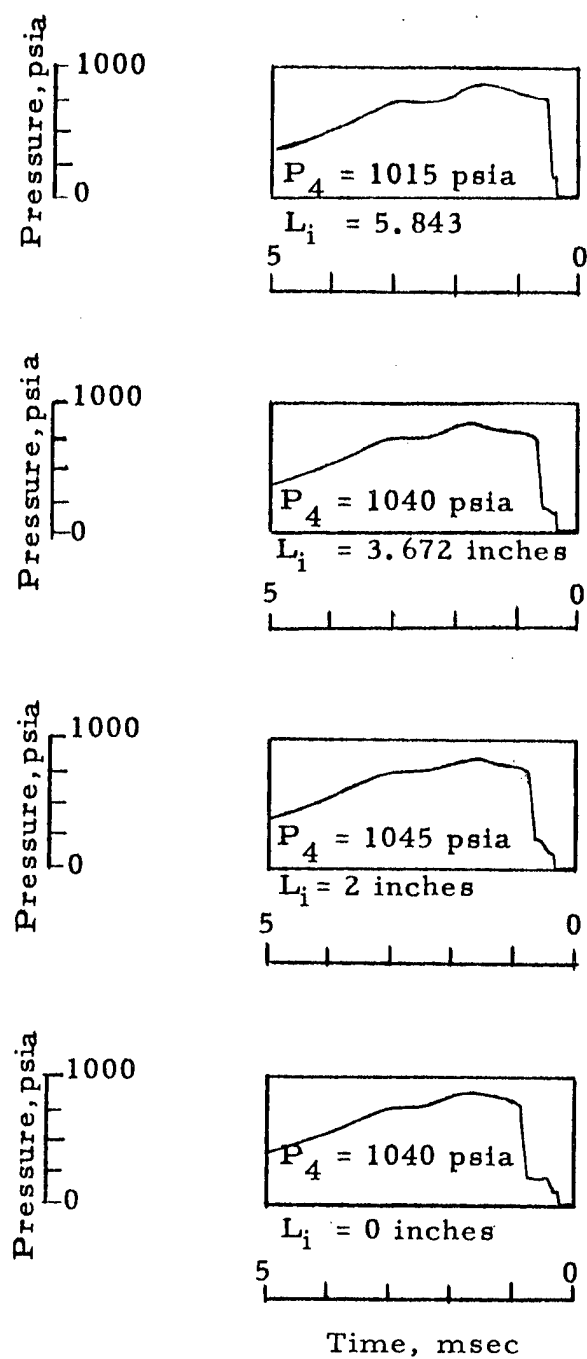


Fig. 7B REFLECTED PRESSURES OF VARIOUS LENGTHS OF REDWOOD

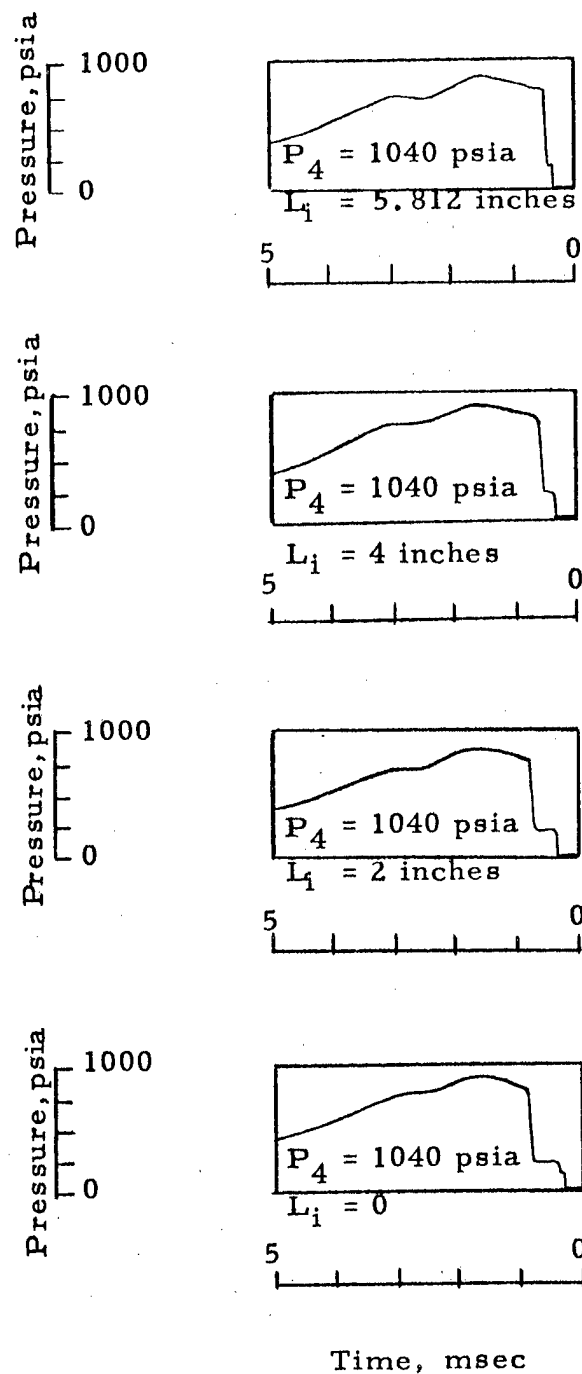


Fig. 7C REFLECTED PRESSURES OF VARIOUS LENGTHS OF SUGAR PINE

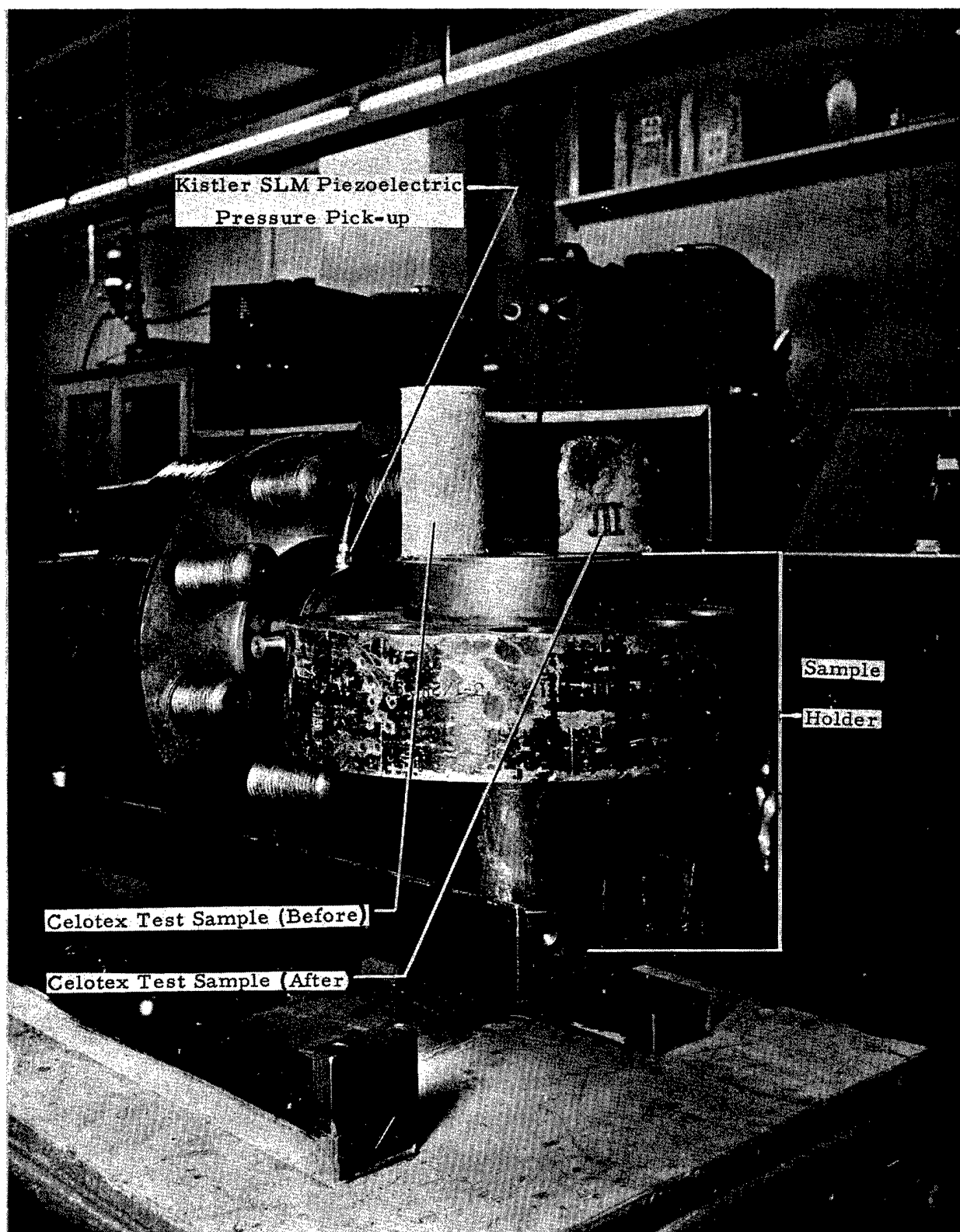


Fig. 8A    PHOTOGRAPH OF CELOTEX SAMPLE BEFORE AND  
AFTER CRUSHING

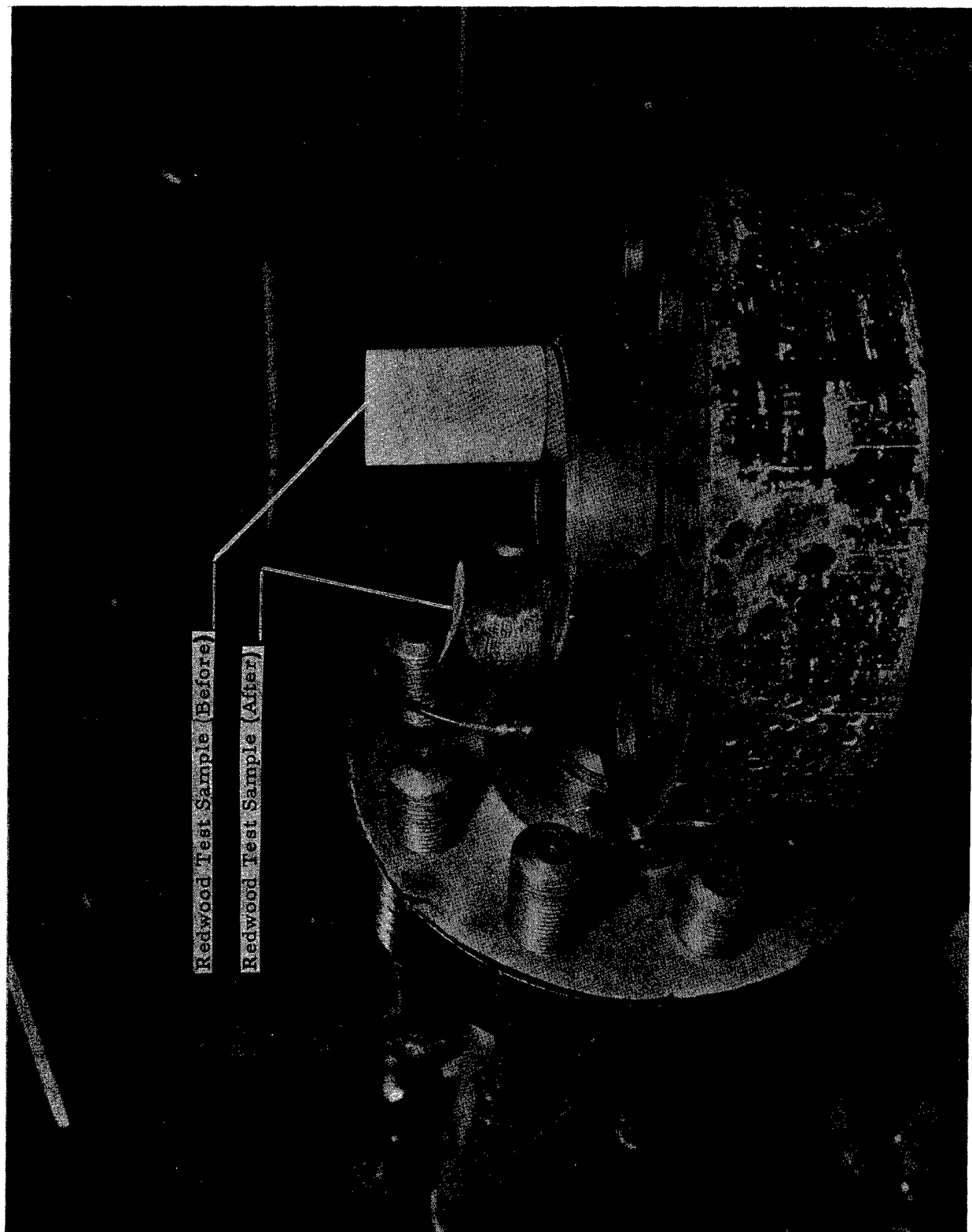


Fig. 8B PHOTOGRAPH OF REDWOOD SAMPLE BEFORE AND AFTER CRUSHING

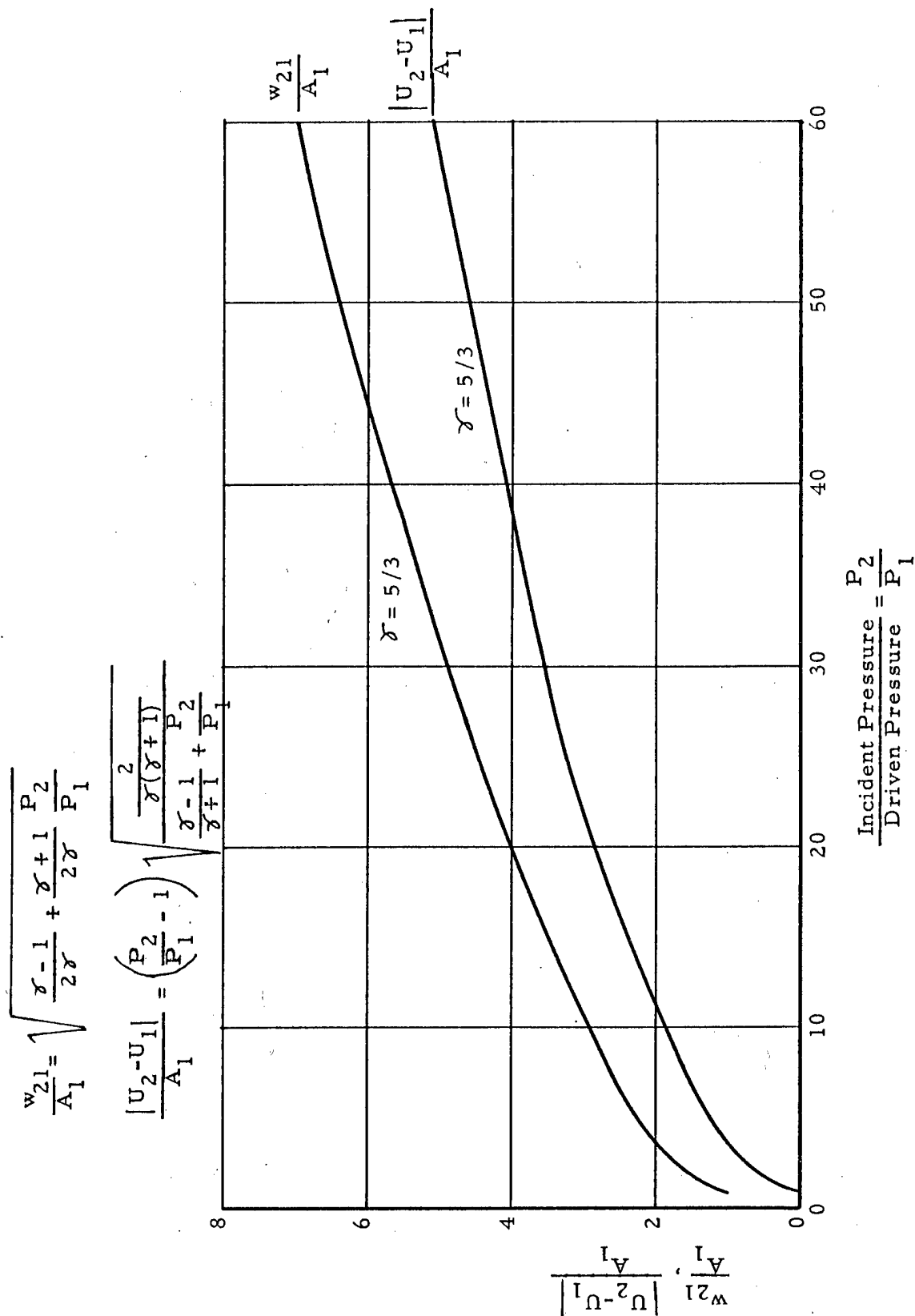


Fig. 9A GRAPH OF INCIDENT SHOCK WAVE VELOCITY AND PARTICLE VELOCITY  
FOR VARIOUS INCIDENT SHOCK WAVE STRENGTHS (THEORETICAL)

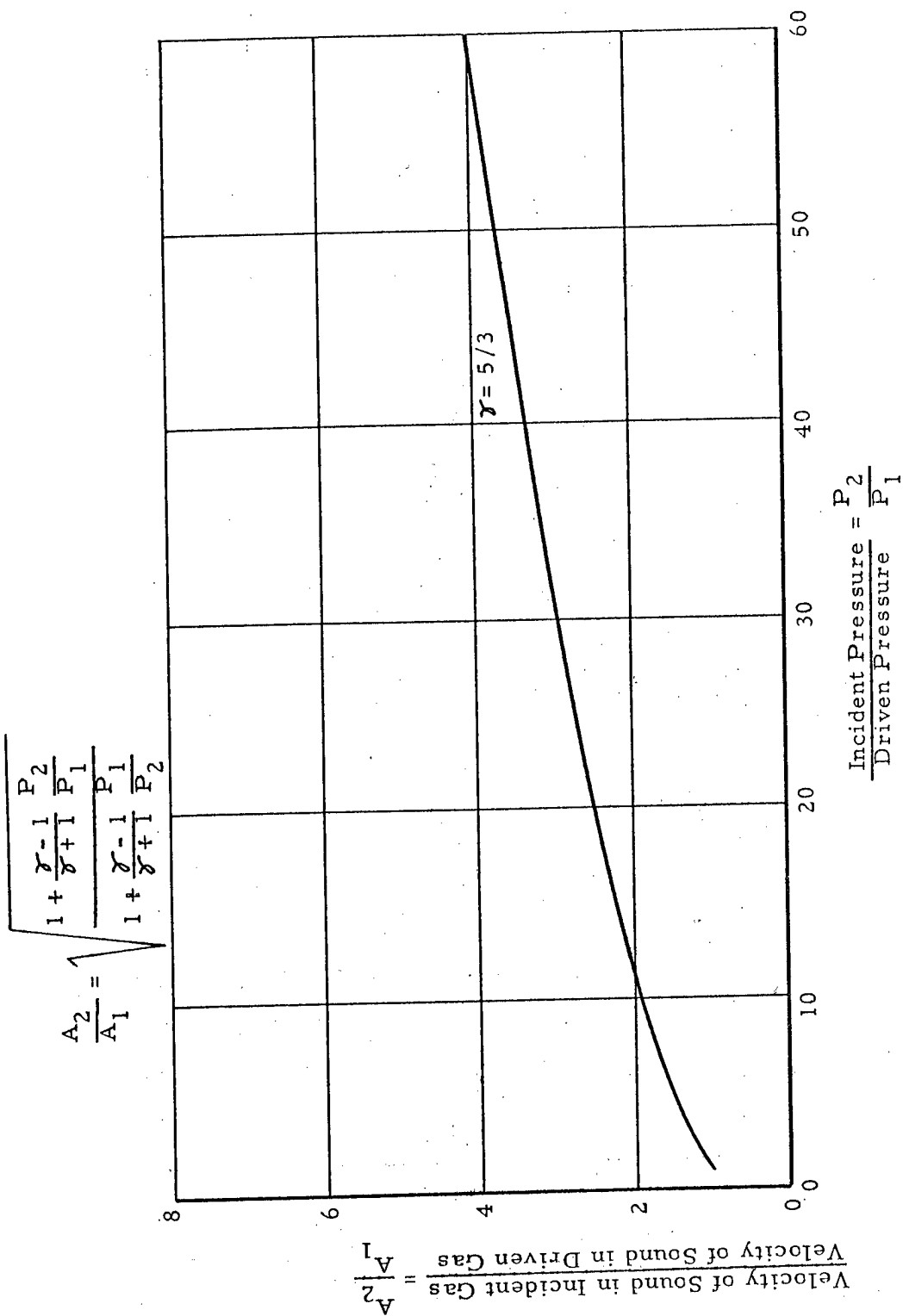


Fig. 9B GRAPH OF THE RATIO OF THE VELOCITY OF SOUND IN THE INCIDENT WAVE AS COMPARED TO THE VELOCITY OF SOUND IN THE DRIVEN GAS FOR VARIOUS SHOCK WAVE STRENGTHS (THEORETICAL)

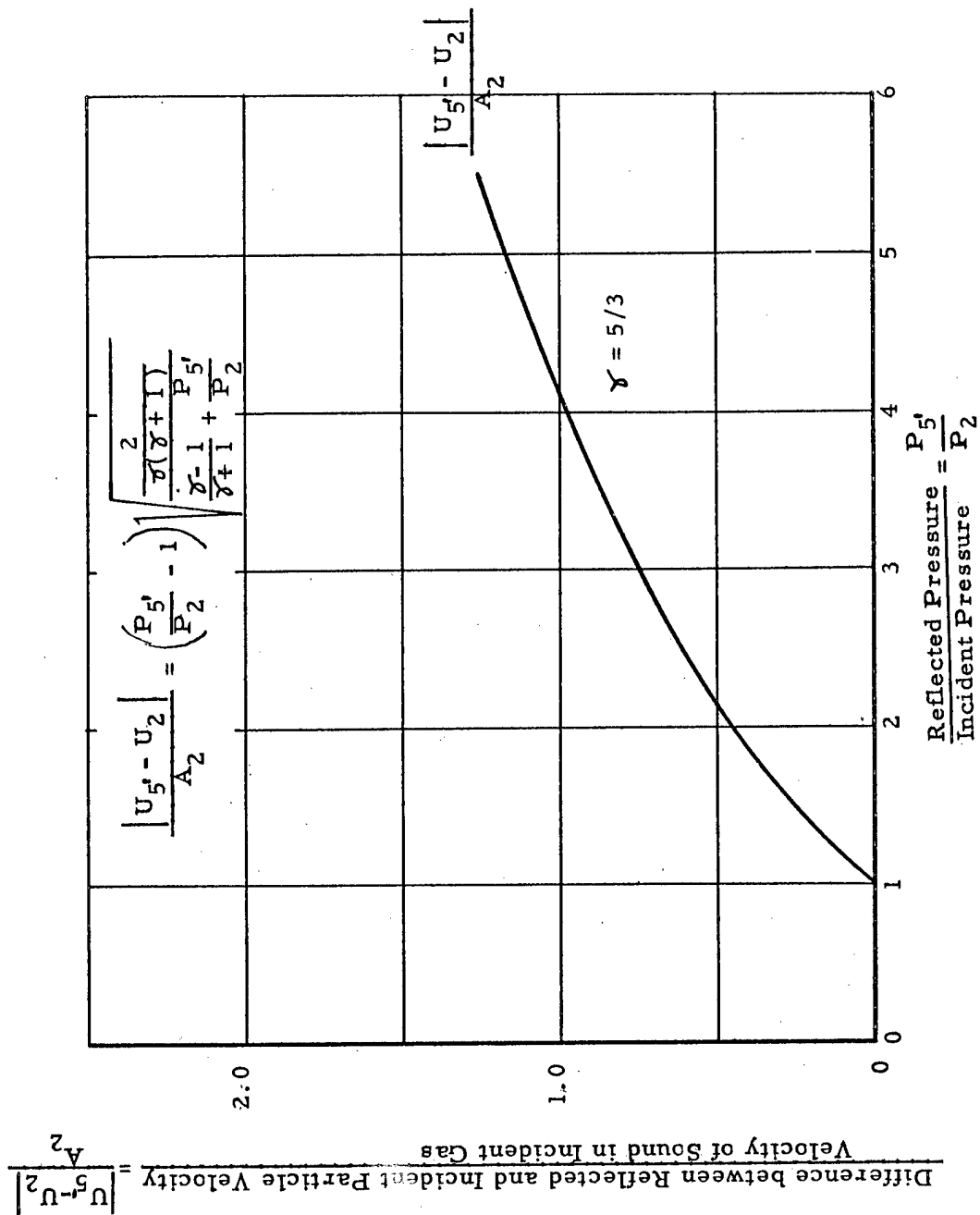


Fig. 9C GRAPH OF RELATIVE PARTICLE VELOCITIES IN THE REFLECTED AND INCIDENT WAVES FOR VARIOUS INCIDENT SHOCK WAVE STRENGTHS (THEORETICAL)



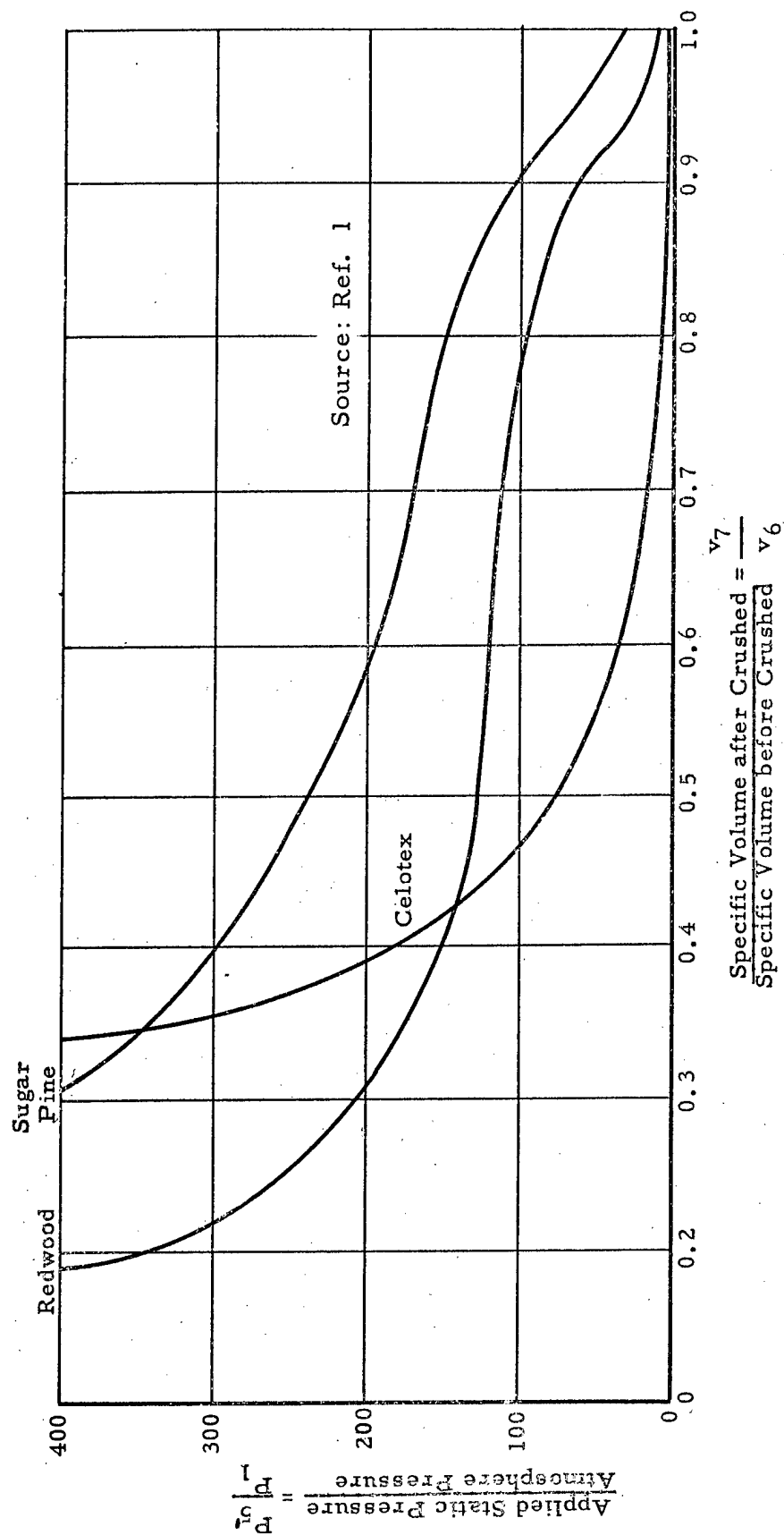


Fig. 10 GRAPH OF STATIC PRESSURE VERSUS SPECIFIC VOLUME FOR CELOTEX,  
REDWOOD, AND SUGAR PINE (EMPIRICAL)

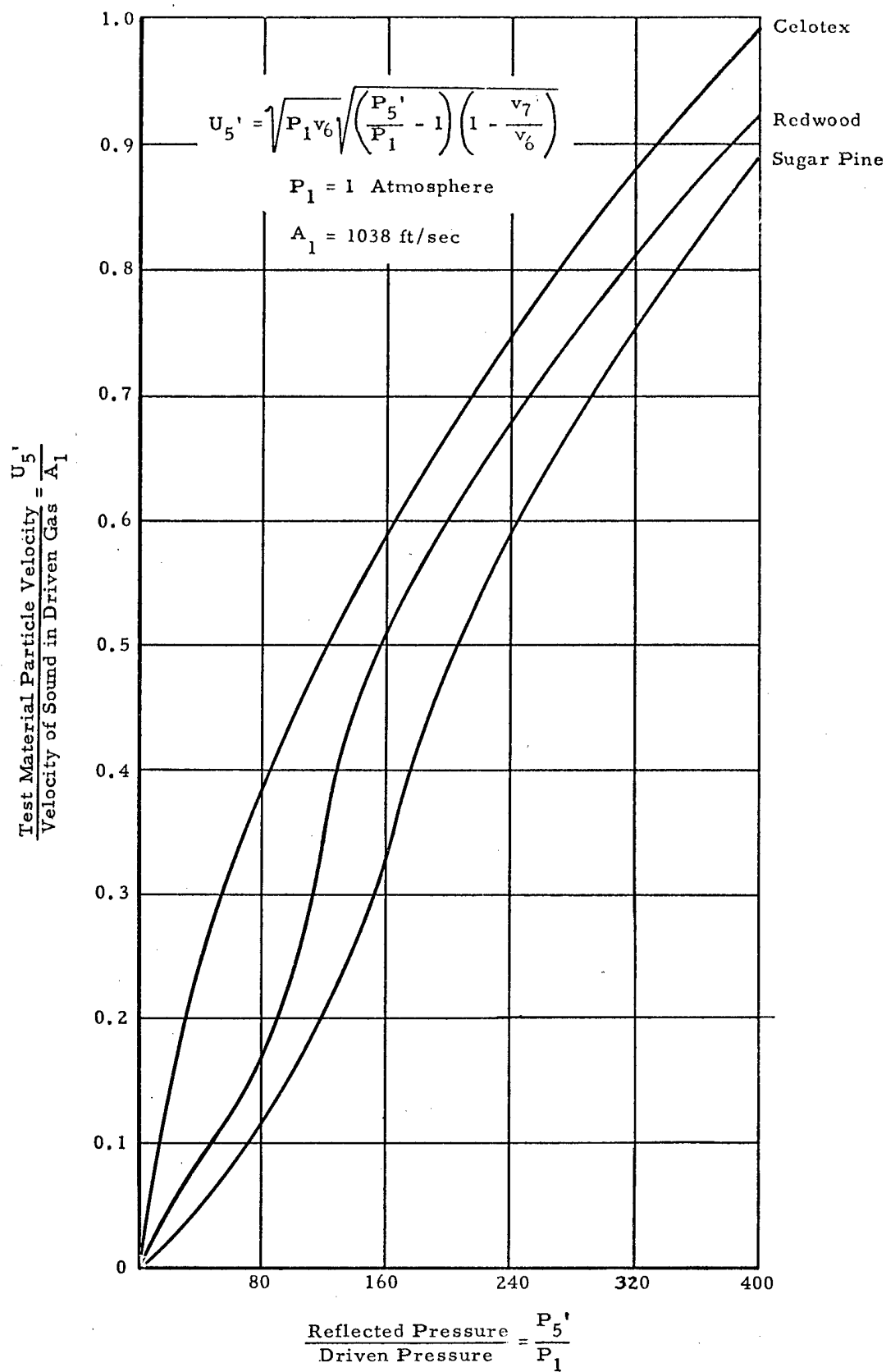


Fig. 11 GRAPH OF CELOTEx, REDWOOD, AND PINE  
PARTICLE VELOCITIES UNDER VARIOUS  
DYNAMIC PRESSURES (SEMI-EMPIRICAL)

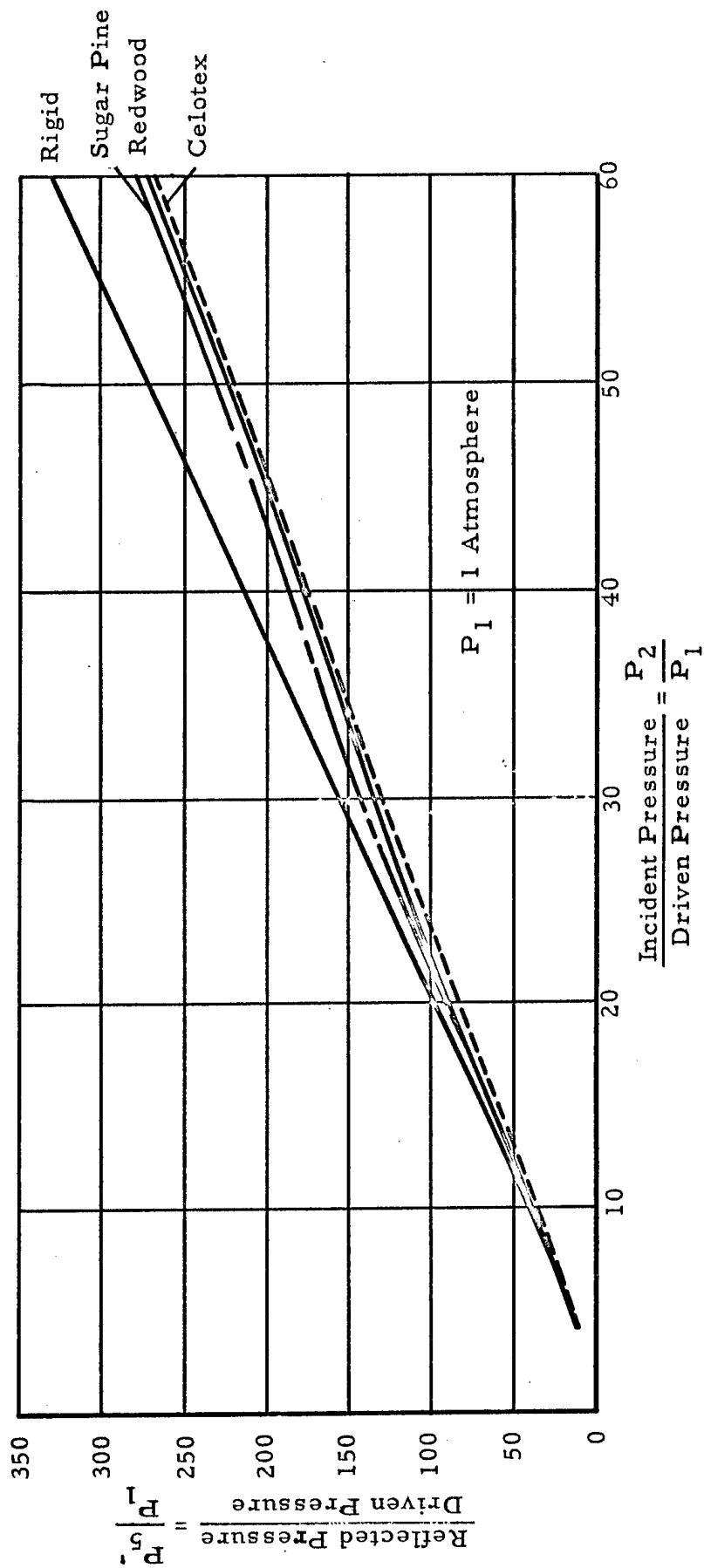


Fig. 12 GRAPH OF REFLECTED PRESSURES OF RIGID SAMPLE HOLDER, REDWOOD, CELOTEX AND PINE FOR VARIOUS INCIDENT SHOCK WAVE STRENGTHS (SEMI-EMPIRICAL)

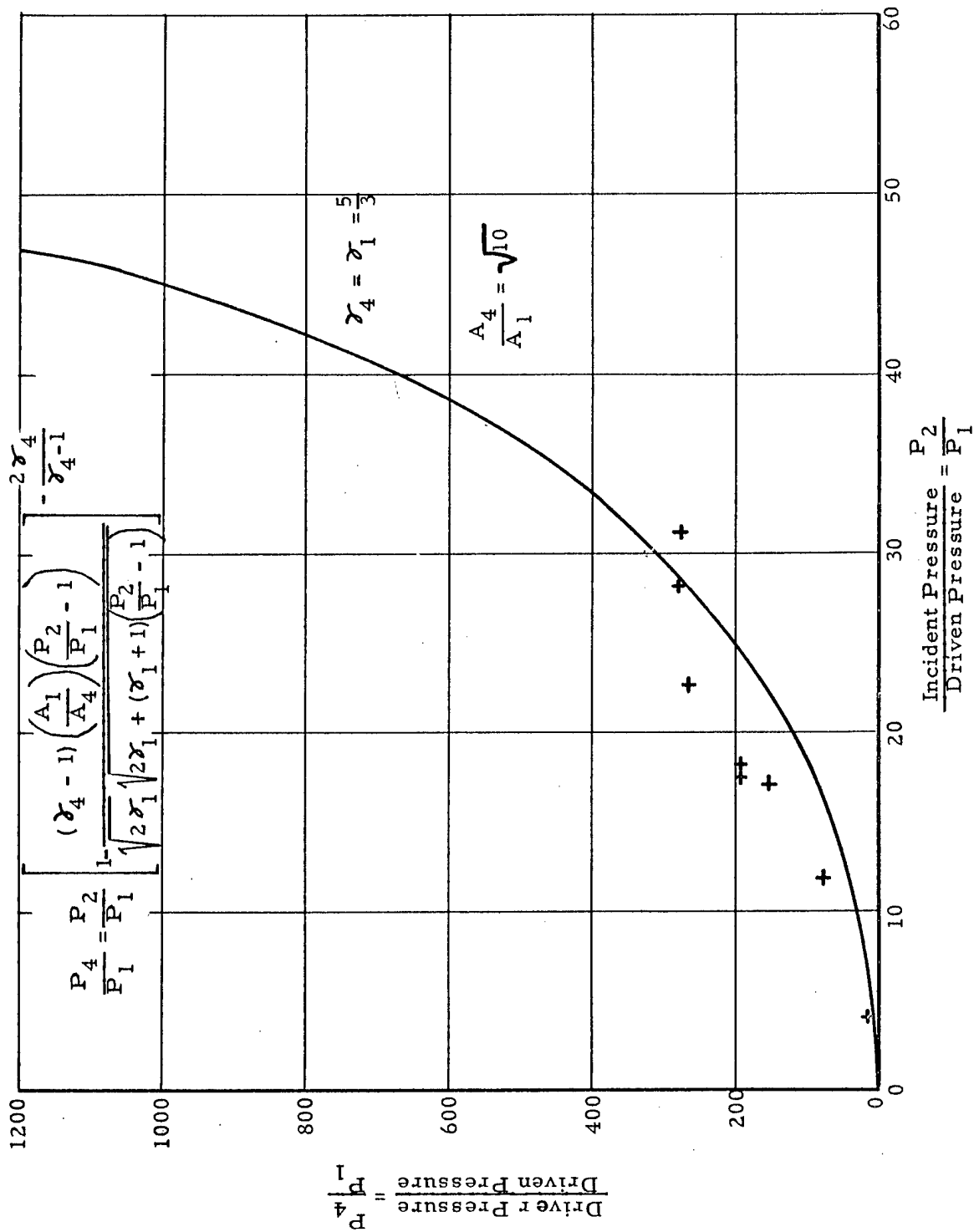


Fig. 13 GRAPH OF DIAPHRAGM BURST PRESSURE RATIO VERSUS GENERATED SHOCK WAVE STRENGTH (THEORETICAL VERSUS EXPERIMENTAL)

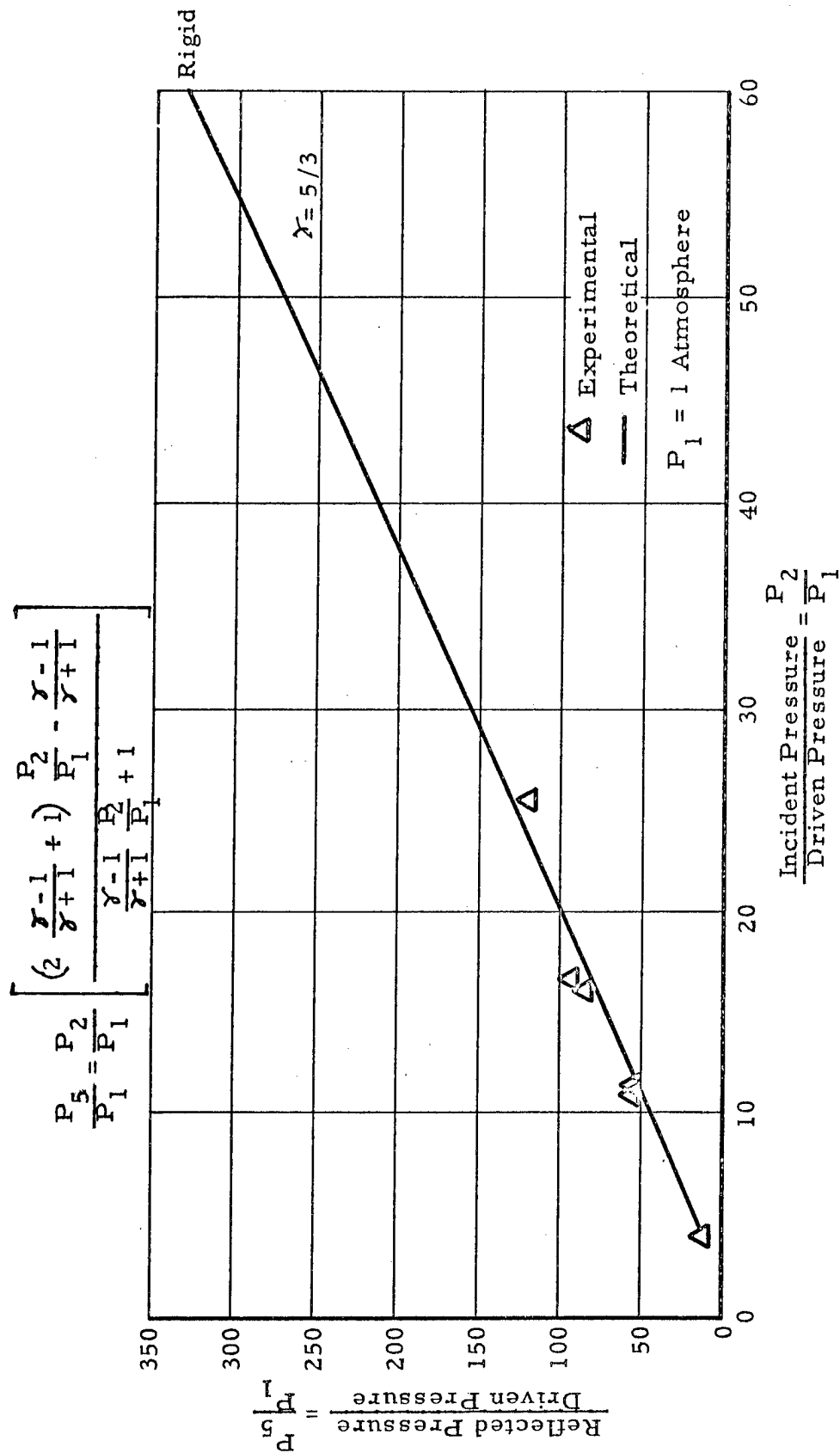


Fig. 14A GRAPH OF REFLECTED PRESSURES OF RIGID SAMPLE HOLDER (THEORETICAL VERSUS EXPERIMENTAL)

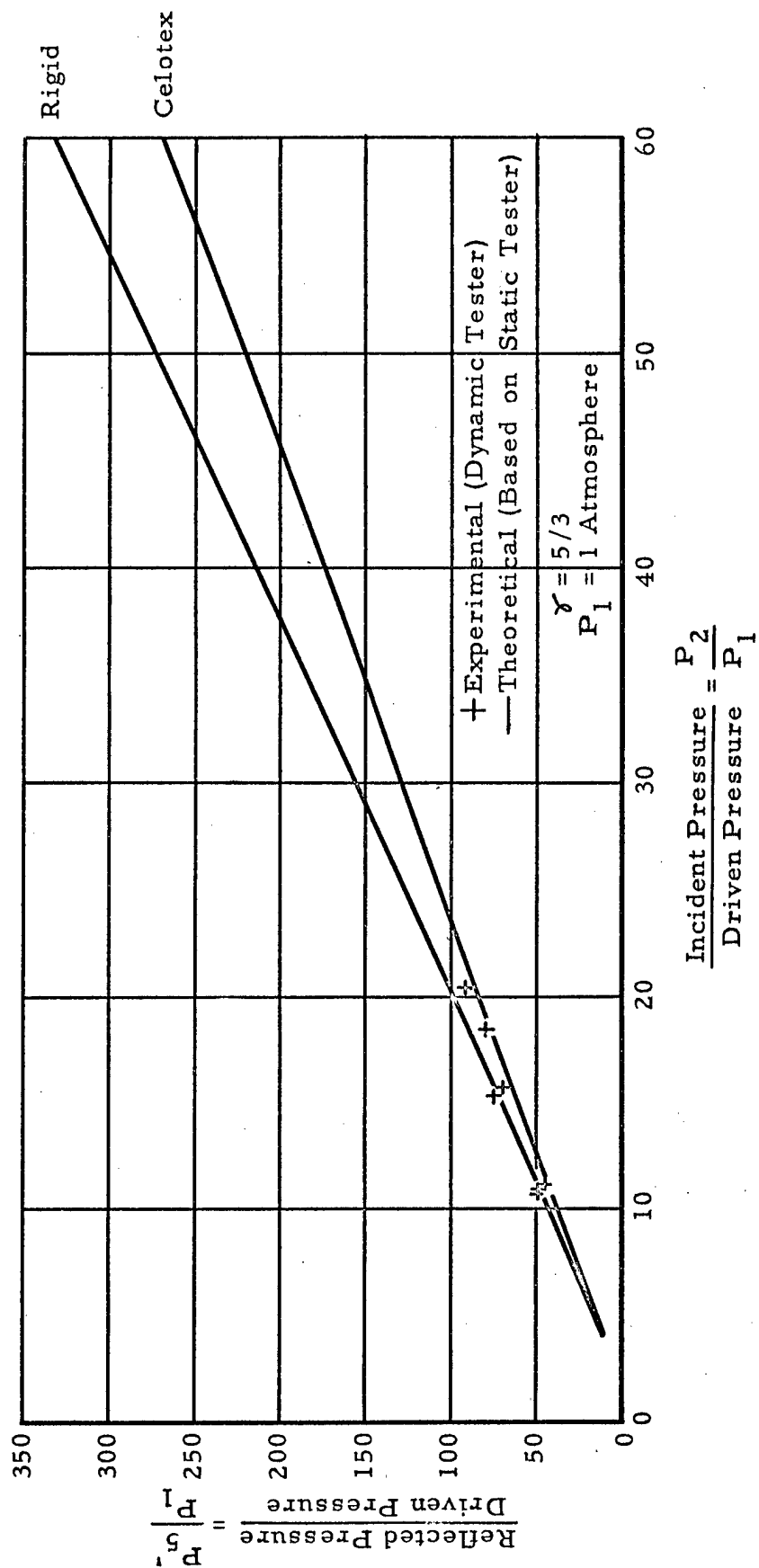


Fig. 14B GRAPH OF REFLECTED PRESSURES OF CELOTEX  
(THEORETICAL VERSUS EXPERIMENTAL)

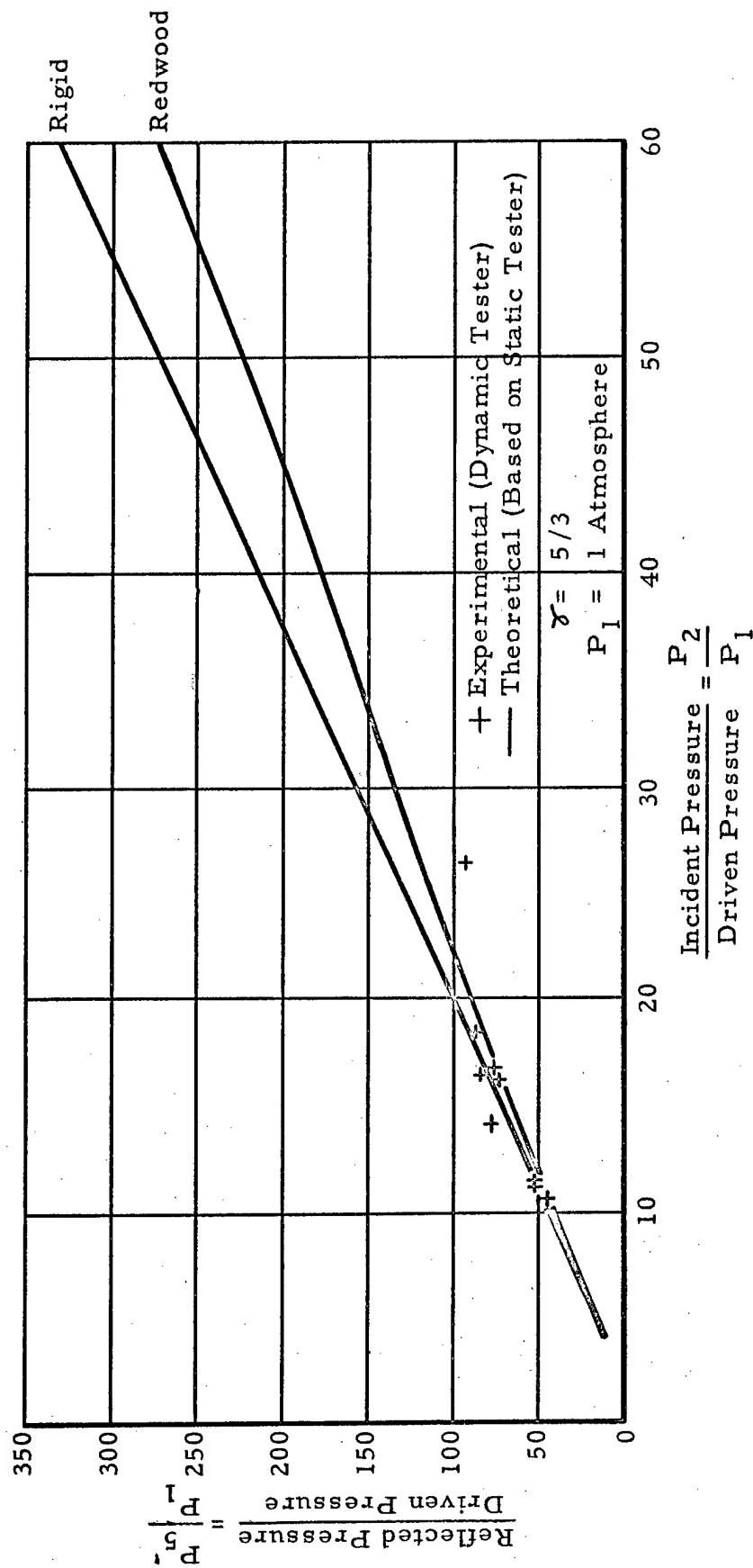


Fig. 14C GRAPH OF REFLECTED PRESSURES OF REDWOOD  
 (THEORETICAL VERSUS EXPERIMENTAL)

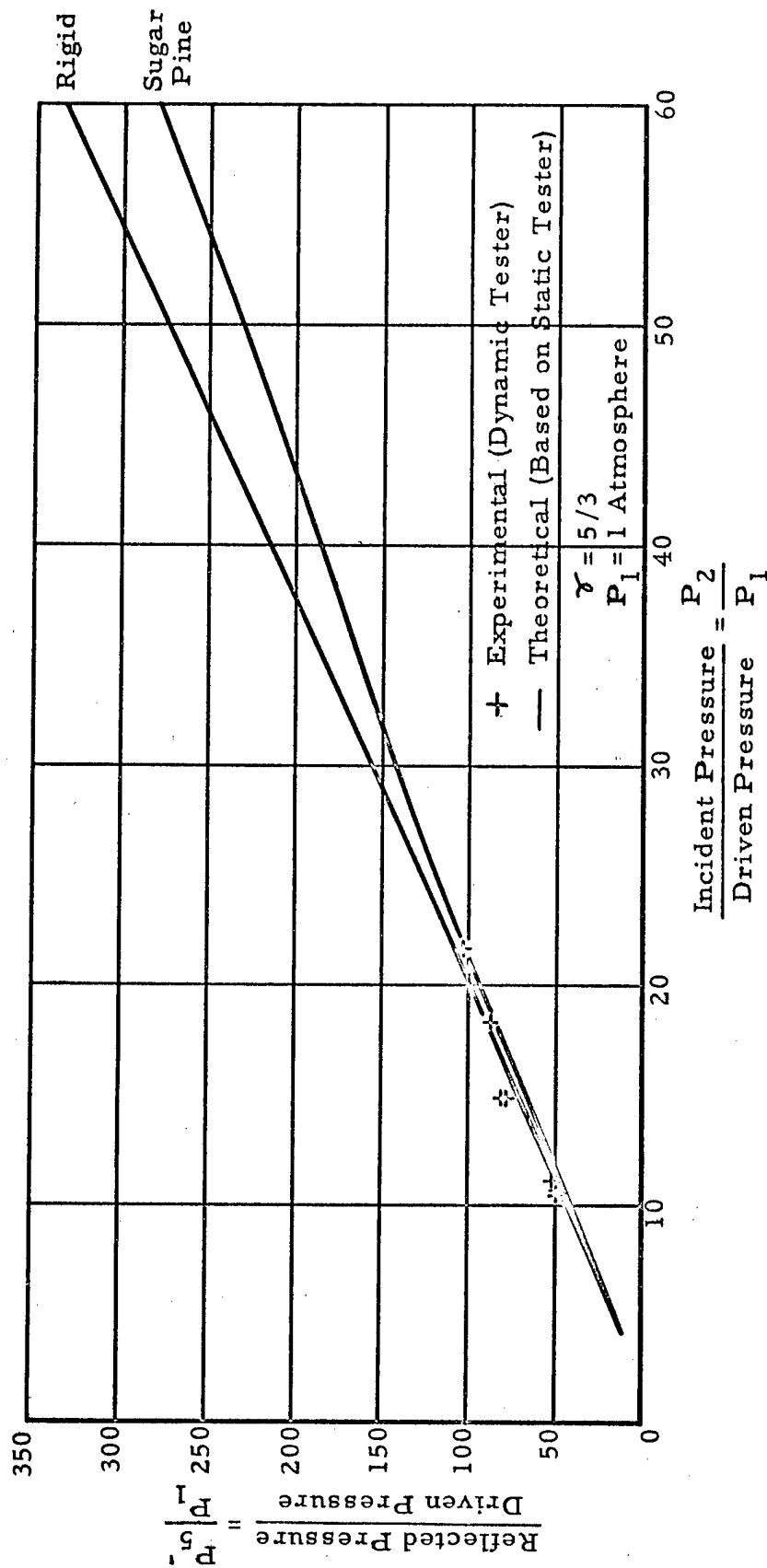


Fig. 14D GRAPH OF REFLECTED PRESSURES OF SUGAR PINE  
(THEORETICAL VERSUS EXPERIMENTAL)



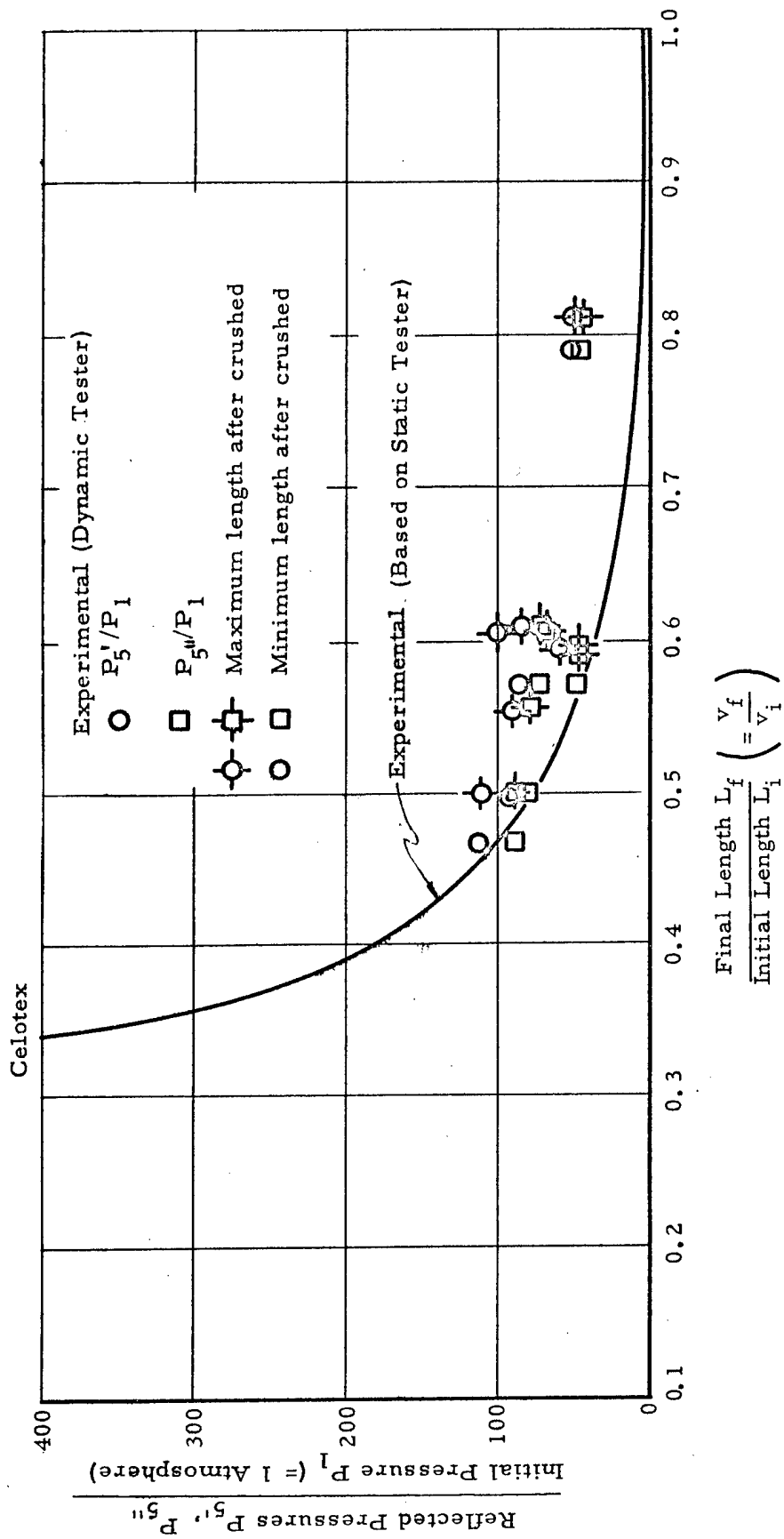


Fig. 15A GRAPH OF REFLECTED AND STATIC PRESSURES VERSUS  
FINAL LENGTH RATIO FOR CELOTEX (EXPERIMENTAL)

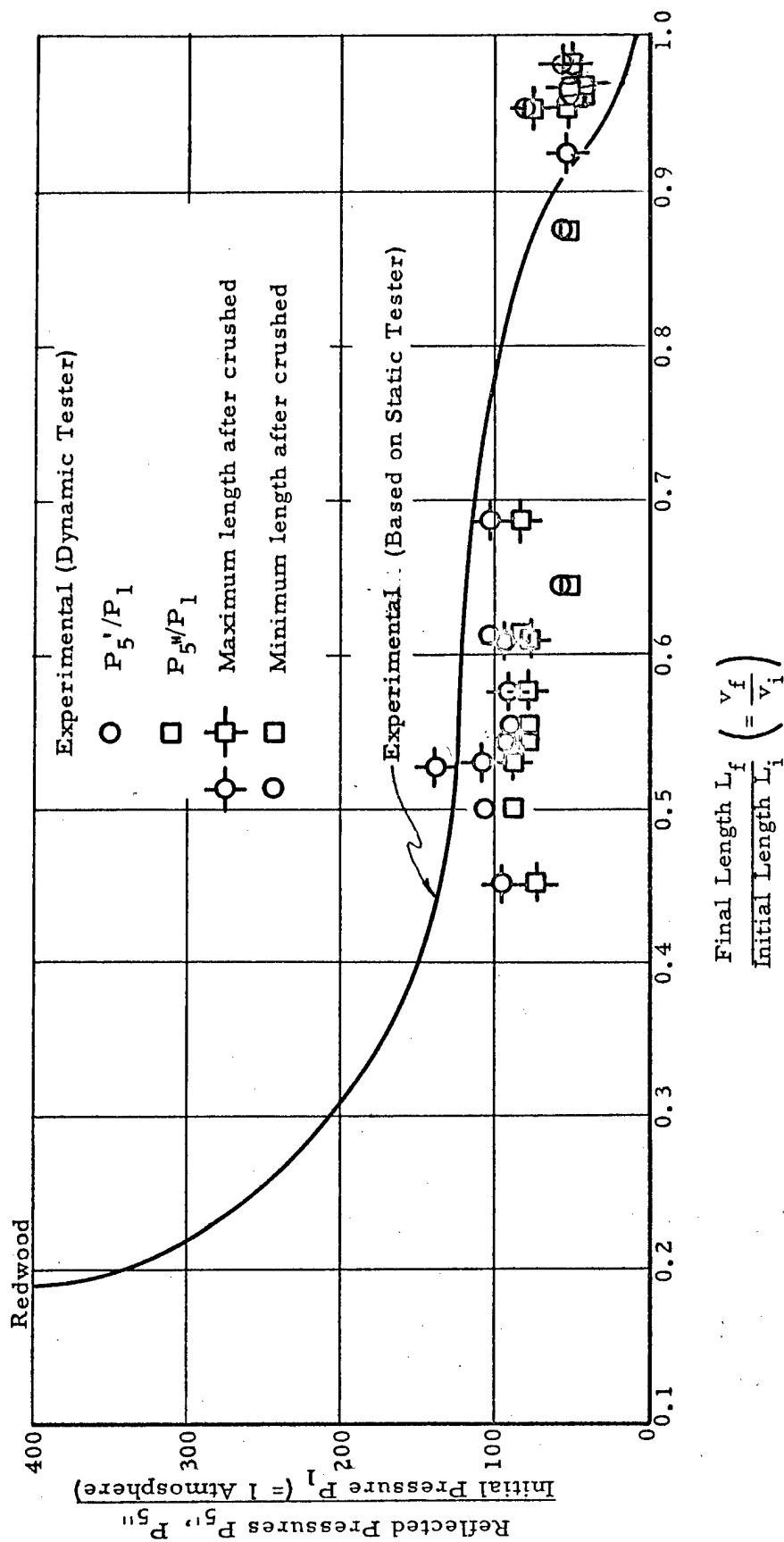


Fig. 15B GRAPH OF REFLECTED AND STATIC PRESSURES VERSUS  
FINAL LENGTH RATIO FOR REDWOOD (EXPERIMENTAL)

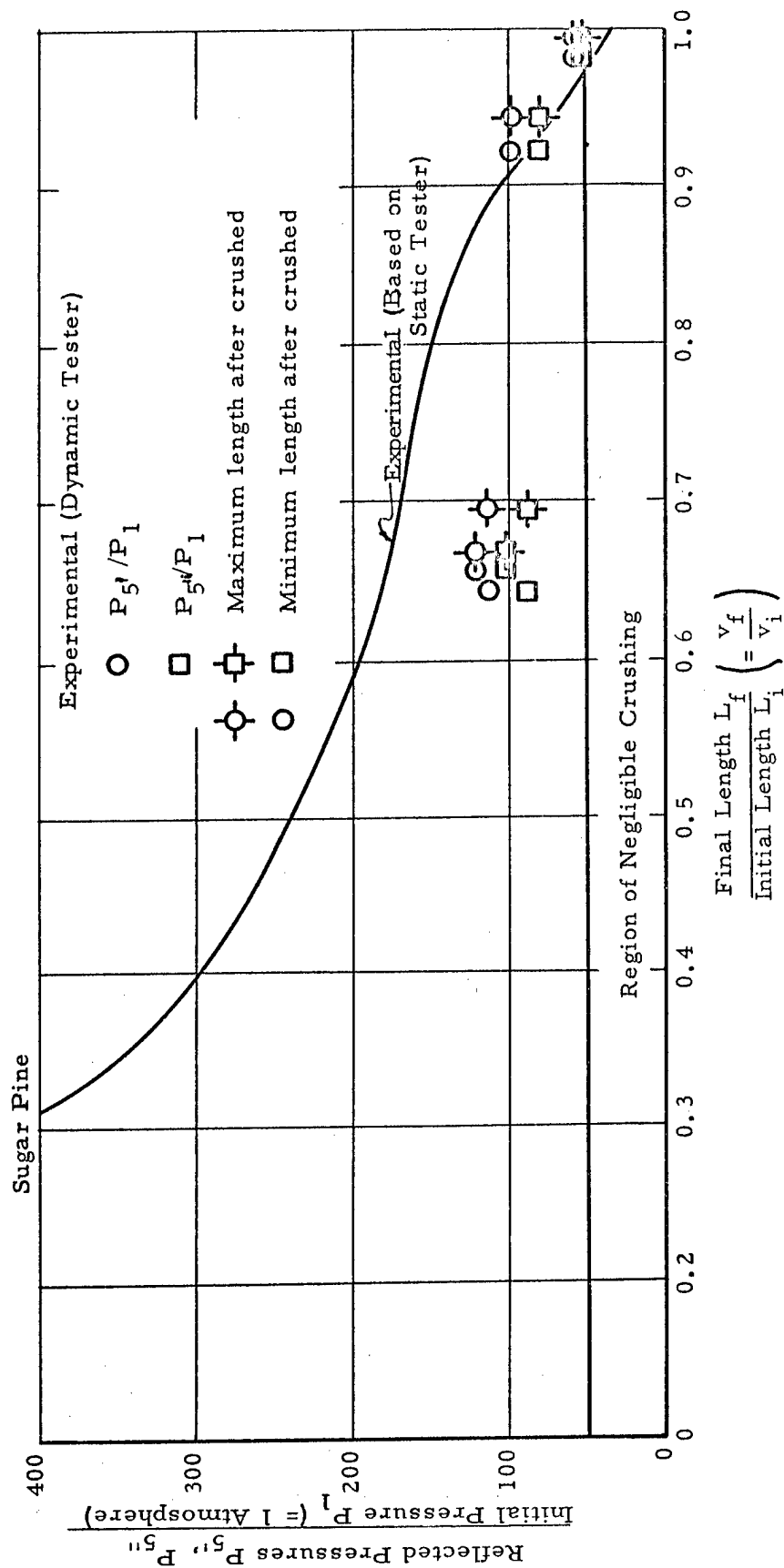


Fig. 15C GRAPH OF REFLECTED AND STATIC PRESSURES VERSUS  
FINAL LENGTH RATIO FOR SUGAR PINE (EXPERIMENTAL)

+ Shock Compression  
 $P_1 = 1$  Atmosphere

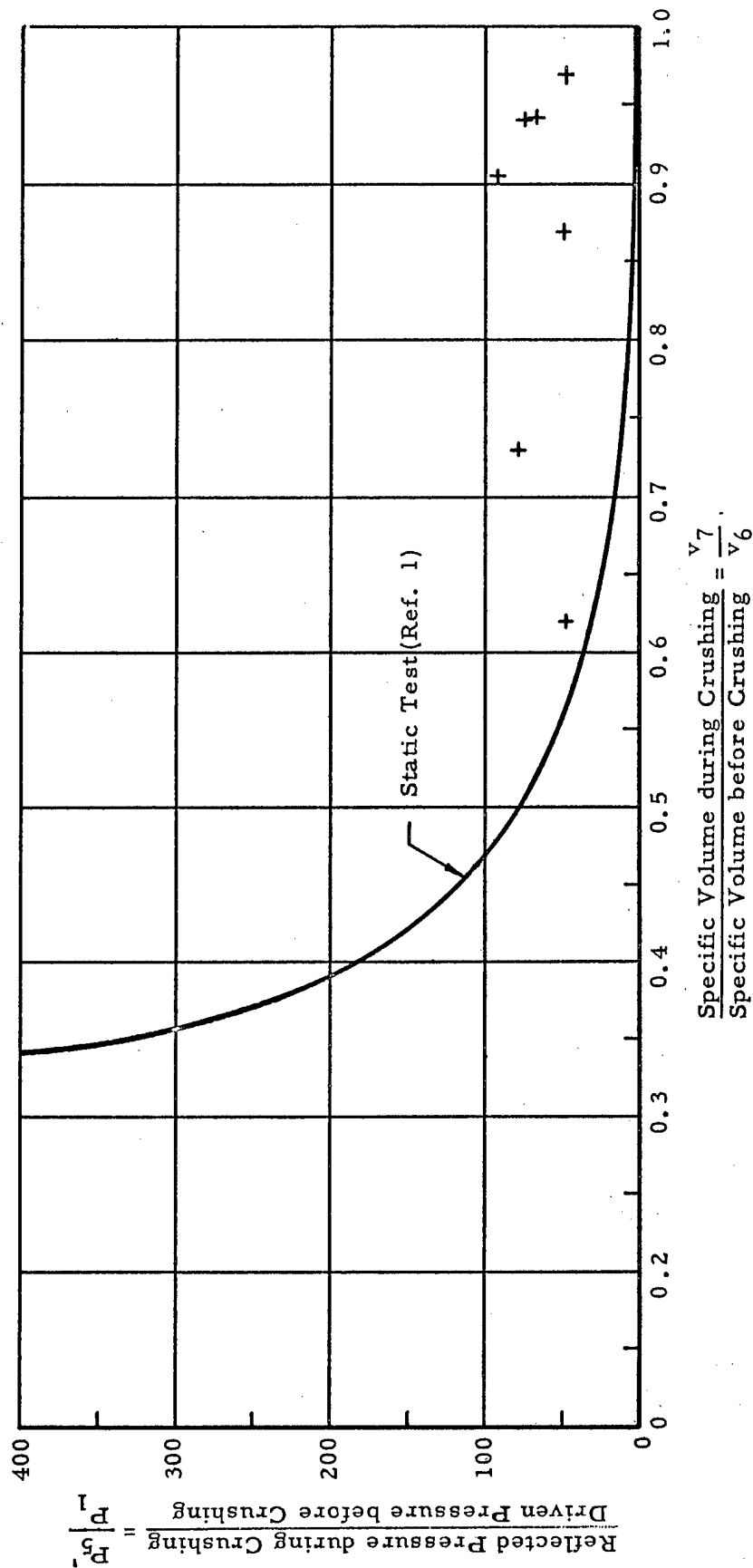


Fig. 16A DATA POINTS FOR THE HUGONIOT FOR CELOTEX

+ Shock Compression  
 $P_1 = 1$  Atmosphere

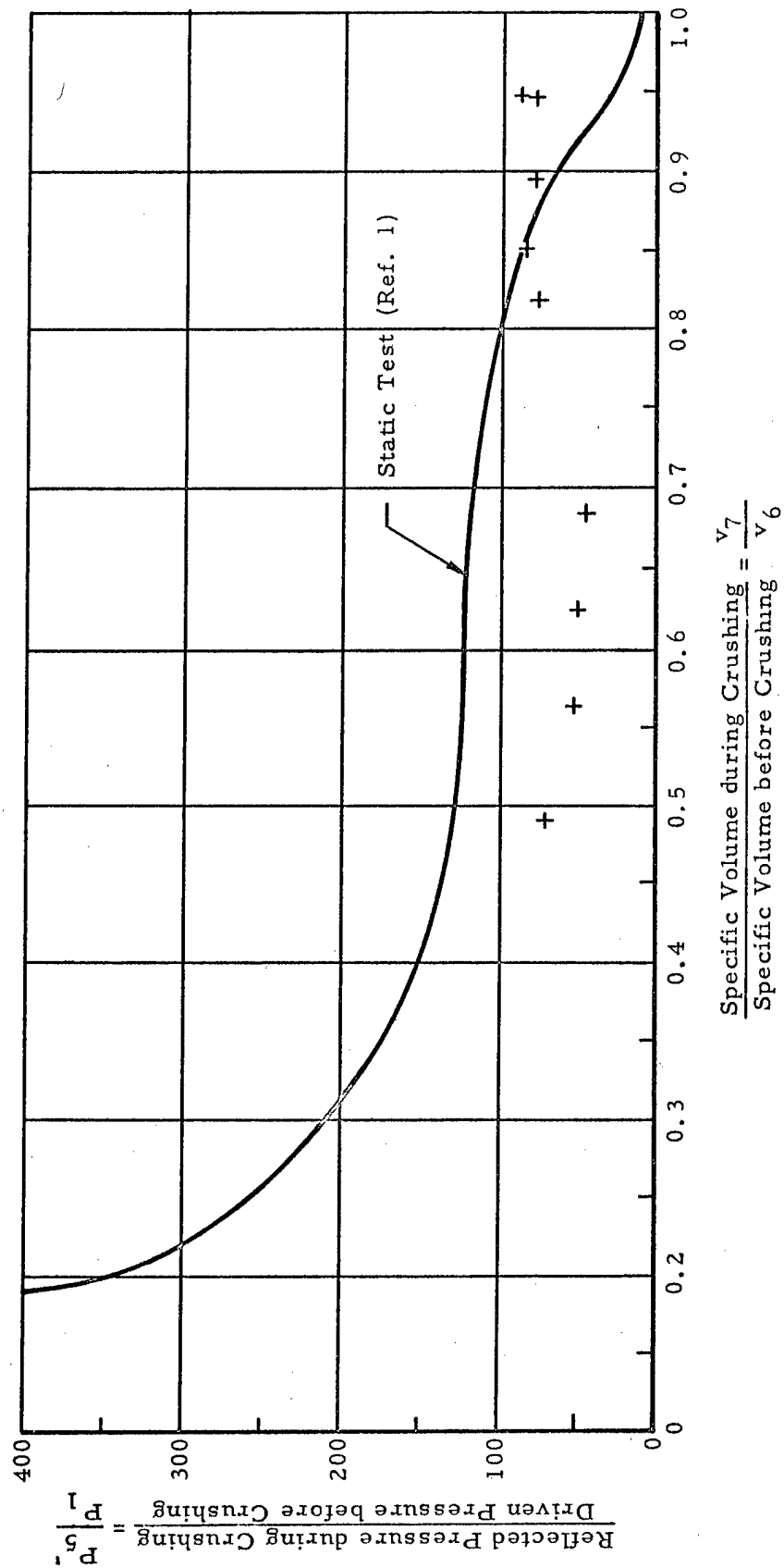


Fig. 16B DATA POINTS FOR THE HUGONIOT FOR REDWOOD

+ Shock Compression  
 $P_1 = 1$  Atmosphere

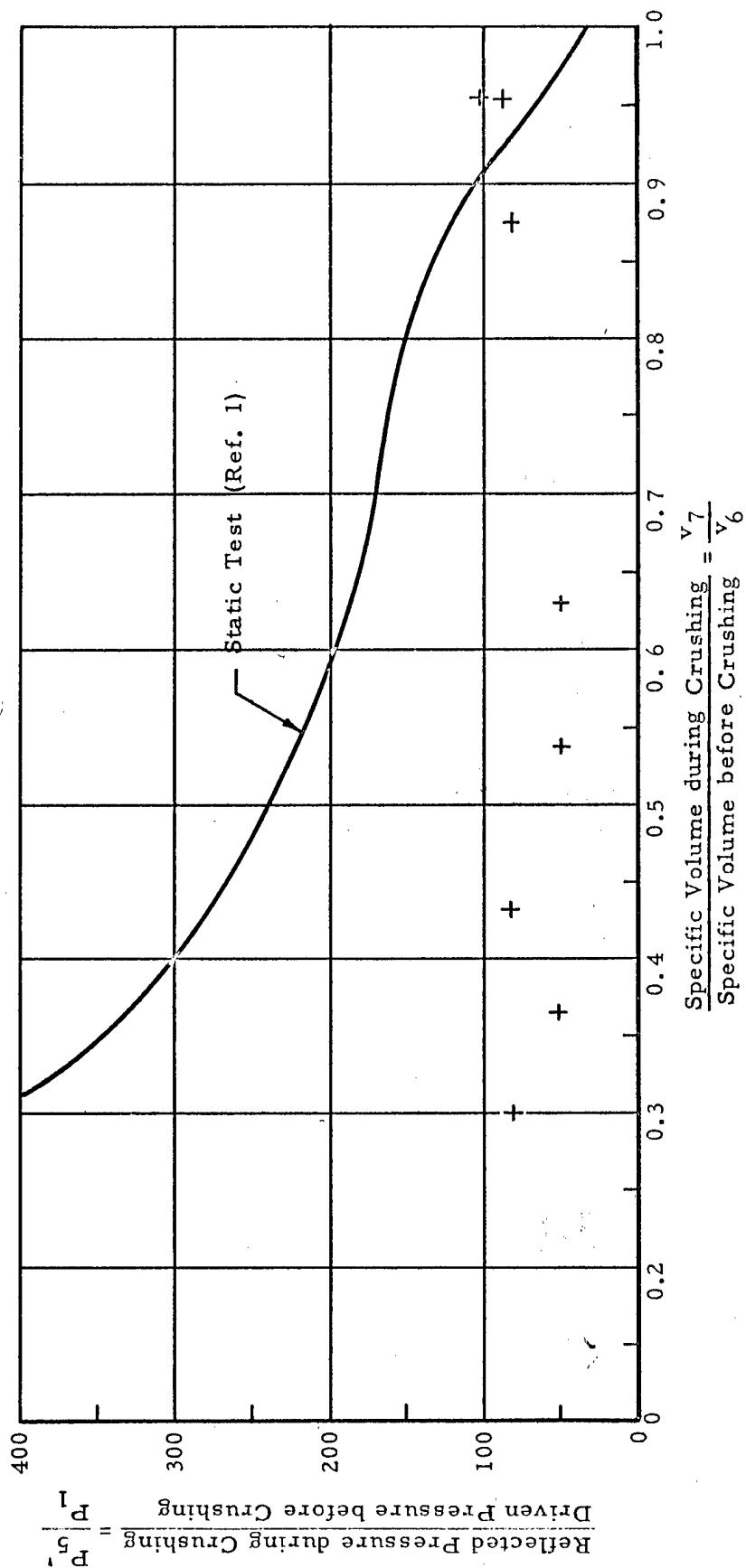


Fig. 16C DATA POINTS FOR THE HUGONIOT FOR SUGAR PINE

## APPENDICES

APPENDIX A  
APPROXIMATE PREDICTION OF REFLECTED PRESSURES

Reflected pressures  $P_5$  resulting from the normal reflection of a shock of pressure  $P_2$  incident upon a rigid wall are calculated directly from Eq. (1), assuming perfect gas behavior in the driven gas.

A rough prediction of the pressure  $P_5$ , resulting from the normal reflection of a shock of pressure  $P_2$  incident upon a compressible solid specimen can be made by assuming (1) that the Hugoniot is not far different from the static pressure-specific volume curve, and (2) that the impinging gas behaves as a perfect gas. The technique involves the matching of pressure and particle velocity in the gas and in the solid at the interface separating the two media. An iterative calculation is convenient for the purpose of this prediction.

A specimen of celotex and an initial driver pressure  $P_4 = 2775$  psia are selected to illustrate the procedure. The gage records at stations 2 and 3 for this case are shown in Fig. 5. The incident shock strength is measured as

$$\frac{P_2}{P_1} = 18.4.$$

This experimentally obtained pressure ratio is used to calculate an associated rigid-wall reflected pressure ratio  $P_5/P_1$  and an approximate anticipated value of the reflected pressure ratio  $P_5/P_1$  associated with the celotex specimen.

A. Rigid Wall Reflection

From Eq. (1) with  $P_2/P_1 = 18.4$  and  $\gamma = 5/3$ , we obtain



$$\frac{P_5}{P_1} = 89.9 .$$

#### B. Celotex Specimen Reflection

By using Eq. (4) of the present report in conjunction with static compression data of Fig. 10, a chart of the velocity ratio  $U_{5'}/A_1$  as a function of the reflected pressure ratio  $P_{5'}/P_1$  can be constructed for the case of celotex. This relationship, which is plotted in Fig. 11, depends on the assumption that the Hugoniot coincides with the static compression curve. The initial sound velocity  $A_1 = 1038$  ft/sec in argon at standard conditions has been used to normalize the interface velocity  $U_{5'}$ .

The approximate prediction of the reflected pressure ratio  $P_{5'}/P_1$  is performed by the following iterative procedure:

1. Enter Fig. 9A with the given value of shock strength  $P_2/P_1 = 18.4$ .

Recalling  $U_1 = 0$ , read the velocity ratio

$$\frac{|U_2|}{A_1} = 2.71 .$$

2. Enter Fig. 9B with  $P_2/P_1 = 18.4$ . Read the sound velocity ratio

$$\frac{A_2}{A_1} = 2.39 .$$

3. Assume a value of  $P_{5'}/P_1$  somewhat less than the value of  $P_5/P_1$  resulting from rigid-wall reflection as calculated in Part A above. For example, take

$$\frac{P_{5'}}{P_1} = 75.0 ,$$

and calculate a trial value of the pressure ratio  $P_{5'}/P_2$ :

$$\frac{P_{5'}}{P_1} = \frac{P_{5'}}{P_1} \cdot \frac{P_1}{P_2} = \frac{75.0}{18.4} = 4.08 .$$

4. Enter Fig. 9C with the trial value of  $P_{5'}/P_2$  from step 3 above. Read the ratio

$$\frac{|U_{5'} - U_2|}{A_2} = 0.98 .$$

5. Calculate the trial values

$$\frac{|U_{5'} - U_2|}{A_1} = \frac{|U_{5'} - U_2|}{A_2} \cdot \frac{A_2}{A_1} = (0.98)(2.39) = 2.34 ,$$

and

$$\frac{U_{5'}}{A_1} = \frac{|U_2|}{A_1} - \frac{|U_{5'} - U_2|}{A_1} = 2.71 - 2.34 = 0.37 ,$$

since, according to Diagram II, we anticipate  $U_2 > U_{5'} > 0$  .

6. Enter Fig. 11 with the trial value of  $U_{5'}/A_1 = 0.37$  and read on the curve for celotex

$$\frac{P_{5'}}{P_1} = 75.0 ,$$

which coincides with the trial value of  $P_{5'}/P_1$  assumed in step 3 above. Thus  $P_{5'}/P_1 = 75.0$  is the desired approximate prediction based on the static compression data. In general, of course, the result of step 6 will not coincide with the first trial value of the reflected pressure ratio. Steps 3 through 6 must be repeated with new trial values of  $P_{5'}/P_1$  until the result of step 6 is brought into coincidence with the corresponding trial value.

The experimental value of  $P_{5'}/P_1$  is obtained from the gage record in Fig. 5 for this case as

$$\frac{P_{5'}}{P_1} = 77.7.$$

The ratio of the final length to the initial length of this specimen was measured and found to range from 0.50 to 0.55 over the cross section of the sample. In Appendix B the method of calculating the density ratio in single shock for this specimen is presented. A comparison can then be made between the final-to-initial length ratio and the single-shock density ratio in order to assess the effect of the later stress-time history on the permanent deformation of the specimen.

APPENDIX B  
DETERMINATION OF POINTS ON THE HUGONIOT

A specimen of celotex and an initial driver pressure  $P_4 = 2775$  psia are selected to illustrate the calculation of a point on the Hugoniot for celotex. The gage records at stations 2 and 3 for this case are shown in Fig. 5. Perfect gas behavior is assumed in the impinging gas. A stepwise procedure is convenient for the purpose of the calculation.

The following pressure ratios for this case are measured from the record of the gage at station 3:

$$\frac{P_2}{P_1} = 18.4,$$

$$\frac{P_{5'}}{P_1} = 77.7.$$

The stepwise procedure is as follows:

1. Calculate the reflected-to-incident pressure ratio:

$$\frac{P_{5'}}{P_2} = \frac{P_{5'}}{P_1} \cdot \frac{P_1}{P_2} = 4.22.$$

2. Enter Fig. 9A with the given value of shock strength

$P_2/P_1 = 18.4$ . Recalling  $U_1 = 0$ , read the velocity ratio

$$\frac{|U_2|}{A_1} = 2.71.$$

3. Enter Fig. 9B with  $P_2/P_1 = 18.4$ . Read the sound velocity ratio

$$\frac{A_2}{A_1} = 2.39.$$

4. Enter Fig. 9C with the reflected-to-incident pressure ratio

$P_{5'}/P_2 = 4.22$  from step 1 above. Read the ratio

$$\frac{|U_{5'} - U_2|}{A_2} = 1.02.$$

5. Calculate the ratios

$$\frac{|U_{5'} - U_2|}{A_1} = \frac{|U_{5'} - U_2|}{A_2} \cdot \frac{A_2}{A_1} = (1.02)(2.39) = 2.44,$$

and

$$\frac{U_{5'}}{A_1} = \frac{|U_2|}{A_1} - \frac{|U_{5'} - U_2|}{A_1} = 2.71 - 2.44 = 0.27.$$

since, according to Diagram II, we anticipate  $U_2 > U_{5'} > 0$ .

6. Calculate the initial sound velocity  $A_1$  in the driven gas

from Eq. (8) using the initial driven chamber temperature. For this case

$T_1 = 65^\circ\text{F} = 525^\circ\text{R}$ . Hence

$$A_1 = \sqrt{\gamma \frac{R_o}{m} T_1} = \sqrt{\left(\frac{5}{3}\right) \left(\frac{1545 \text{ lb-ft/mol-}^\circ\text{R}}{40.0/32.2 \text{ slugs/mol}}\right) (525^\circ\text{R})} = 1042 \text{ ft/sec.}$$

7. Calculate the interface velocity

$$U_{5'} = \left(\frac{U_{5'}}{A_1}\right) A_1 = (0.27)(1042) = 281 \text{ ft/sec.}$$

8. Solve Eq. (4) for the shock specific volume ratio  $v_7/v_6$ .

Calculate the value of  $v_7/v_6$  using the result of step 7 above together with appropriate values of the initial driven chamber pressure  $P_1$  and the initial specific volume of the specimen,  $v_6$ . For this case  $P_1 = 14.4 \text{ psia}$ , and the initial weight density of the celotex specimen  $g\rho_6 = g/v_6 = 17.5 \text{ lb/ft}^3$ , where  $g = 32.2 \text{ ft/sec}^2$  is the gravitational acceleration. Thus

$$\frac{v_7}{v_6} = 1 - \frac{U_{s'}^2}{(P_1 v_6) \left( \frac{P_{s'}}{P_1} - 1 \right)} = 1 - \frac{(281)^2 (\text{ft/sec})^2}{(14.4 \text{ lb/in}^2)(144 \text{ in}^2/\text{ft}^2) (77.7 - 1)} \\
= 1 - 0.27 \\
= 0.73.$$

Thus a point on the Hugoniot for celotex is defined by the number pair  $(P_{s'}/P_1, v_7/v_6) = (77.7, 0.73)$ . This point appears on the chart for celotex, Fig. 16A.

Recall from Appendix A that the final-to-initial length ratio of this specimen was measured and found to range from 0.50 to 0.55 over the cross section of the sample. Since the cross-sectional dimensions of the sample are essentially unchanged in confined compression, this ratio represents a final-to-initial specific volume ratio and may be compared to the specific volume ratio obtained above for the case of single shock. The effects of successive traversal of the specimen by compression and expansion waves, and the associated volume changes in the deformation history of the specimen after initial shock, are apparently quite considerable.

It is interesting to note that the static compression curve for celotex in Fig. 16A shows that the specific volume ratio associated with the static pressure of 77.7 atmospheres is about 0.495. This is again considerably different from the specific volume ratio for celotex in single shock at the same pressure.

## APPENDIX C

### SHOCK TUBE PERFORMANCE

In this appendix we discuss some advantages and inherent limitations of the shock tube in regard to shock impingement experiments on crushable solids.

The shock tube is a convenient device for generating steep-fronted pressure waves with fairly uniform flow for periods of the order of a few milliseconds. The shock tube used in the present study is of circular cross section 18 ft in length, consisting of a 6-ft driver chamber and a 12-ft driven chamber. Initially, the high-pressure driver chamber is separated from the low-pressure driven chamber by a diaphragm (see Diagram I and Fig. 1). Initially the gas in each chamber is at rest and in thermal equilibrium, but the two chambers may contain different gases at different temperatures.

When the diaphragm bursts as a result of driver chamber pressurization, a shock wave moves into the driven gas. According to ideal shock tube theory, the strength of the shock is a function of the initial chamber pressures and temperatures and the physical properties of the gases. Perfect gas behavior is assumed in both chambers. For purposes of tests on solid specimens at the downstream end of the driven section, it is desired to produce strong shock waves as conveniently as possible. Shock generation can be optimized by proper choice of gases and initial conditions.

The shock pressure  $P_2$  is related to the initial driver chamber pressure  $P_4$  according to ideal shock tube theory by (see Ref. 7, p. 78)

$$\frac{P_4}{P_1} = \frac{P_2}{P_1} \left[ 1 - \frac{(\gamma_4 - 1) \left( \frac{A_1}{A_4} \right) \left( \frac{P_2}{P_1} - 1 \right)}{\sqrt{2\gamma_1} \sqrt{2\gamma_1 + (\gamma_1 + 1) \left( \frac{P_2}{P_1} - 1 \right)}} \right]^{\frac{2\gamma_4}{\gamma_4 - 1}}, \quad (C-1)$$

where the symbol A denotes sound velocity, P denotes pressure, and  $\gamma$  denotes the ratio of specific heats of a gas. The subscripts 1 and 4 refer to initial conditions in the driven and driver gases, respectively (see Diagram I). The ratio of initial sound velocities is given by (see Eq. (8) of the present report

$$\frac{A_1}{A_4} = \sqrt{\frac{m_4 T_1}{m_1 T_4}}, \quad (C-2)$$

where m denotes the molecular weight of a gas and T denotes its absolute temperature. In order for Eqs. (C-1) and (C-2) to apply, the gases must be sufficiently well behaved so that perfect gas laws can be assumed to govern. By inspection of Eqs. (C-1) and (C-2) it is clear that  $P_2$  increases with increasing  $P_4$  to a finite limit as  $P_4$  becomes infinitely large. The limit is given by

$$\lim_{P_4 \rightarrow \infty} \frac{P_2}{P_1} = 1 + \frac{\gamma_1(\gamma_1 + 1)}{(\gamma_4 - 1)^2} \left( \frac{A_4}{A_1} \right)^2 + \frac{\gamma_1}{\gamma_4 - 1} \frac{A_4}{A_1} \left[ \left( \frac{\gamma_1 + 1}{\gamma_4 - 1} \right)^2 \left( \frac{A_4}{A_1} \right)^2 + 4 \right]^{1/2}. \quad (C-3)$$

The pressure  $P_5$  resulting from the normal reflection of a shock of pressure  $P_2$  in the driven gas from a rigid boundary is given by (recall Eq. (1) of the present report



$$\frac{P_5}{P_1} = \frac{P_2}{P_1} \left[ \frac{\left( 2 \frac{\gamma_1 - 1}{\gamma_1 + 1} + 1 \right) \frac{P_2}{P_1} - \frac{\gamma_1 - 1}{\gamma_1 + 1}}{\frac{\gamma_1 - 1}{\gamma_1 + 1} \frac{P_2}{P_1} + 1} \right] \quad (C-4)$$

Consider now a helium/helium or argon/argon shock tube with  $T_4 = T_1$ .

Then  $A_4 = A_1$ ,  $\gamma_4 = \gamma_1 = 5/3$ , and from Eq. (C-3)

$$\lim_{P_4 \rightarrow \infty} \frac{P_2}{P_1} \cong 22.$$

Thus the maximum reflected pressure ratio  $P_5/P_1$  which could be produced as a result of normal reflection from a rigid closed end would be, from Eq. (C-4),

$$\lim_{P_4 \rightarrow \infty} \frac{P_5}{P_1} \cong 110.$$

The use of different gases improves shock generation considerably.

Consider a helium/argon shock tube with  $T_4 = T_1$ . This is the combination used in the present experimental program. Since helium has molecular weight  $m_4 = 4.003$  and argon has molecular weight 39.994, we have

$$\frac{A_4}{A_1} \cong \sqrt{10}.$$

Again  $\gamma_4 = \gamma_1 = 5/3$  for the monatomic gases involved, so that, from Eq. (C-3),

$$\lim_{P_4 \rightarrow \infty} \frac{P_2}{P_1} \cong 200.$$

In this case the maximum reflected pressure ratio is, from Eq. (C-4),

$$\lim_{P_4 \rightarrow \infty} \frac{P_5}{P_1} \approx 1200.$$

The results from ideal shock tube theory are useful in guiding the choice of operating techniques; they do not take into account energy losses in diaphragm breakage; viscosity, heat conduction, and mass diffusion effects in the gas; non-ideal contact surface effects; and deviations of the equation of state from that of a perfect gas. In practice, pressure and velocity measurements must be relied upon to provide reference or calibration data for a shock tube (see Fig. 13). The choice of helium and argon is optimum from other considerations. Both gases are inert noble gases, so that tube corrosion is minimized. Apparently boundary layer effects and non-ideal contact surface effects are also reduced, since it has been found<sup>9</sup> that cleaner flat-topped waves are produced with this combination of gases than with several others.

In shock impingement experiments on solids, the specimen is placed in the driven chamber and is thus initially immersed in a bath of pressure  $P_1$ . The significant variable involved in the crushing of a specimen should be the magnitude of the reflected pressure  $P_5$ , (see Diagram I) relative to a parameter like the bulk modulus of the material, rather than the pressure ratio  $P_5/P_1$ . In the experiments described in the present report,  $P_1 = 1$  atmosphere throughout, and it was convenient in calculations to normalize all pressures to  $P_1$ , which is equivalent to reporting the values of pressure in units of atmospheres. It is likely that initial static pressurization up to, say, several atmospheres has little effect on the compressibility of the solid and hence little effect on the determination of the Hugoniot. Thus the range of the pressure  $P_5$ , in the experiments can be extended by

perhaps an order of magnitude through initial pressurization of the driven gas, since the pressure ratios  $P_4/P_1$ ,  $P_2/P_1$ , and  $P_5/P_1$  are the pertinent dimensionless variables for the phenomena in the gases (note Eqs. (C-1) through (C-4) ).

Still further improvement in shock generation can be attained by heating the helium driver to increase its initial temperature  $T_4$  and hence its initial sound velocity  $A_4$  (see Eq. C-3) ). This can be accomplished by the use of externally supplied heat from an electric heater or by the use of combustible additives and spark ignition. The latter technique is discussed in Section II-A-3 of the present report.

Proper selection of the lengths of the driver and driven chambers and proper positioning of the gage upstream of the gas-solid interface are also essential. The length of the driver chamber relative to that of the driven chamber affects the duration of the flat-topped portion of the pressure wave (see Diagram I). The centered rarefaction wave originating at the diaphragm station at burst time propagates into the driver chamber and is reflected from the closed driver end of the tube. The reflected expansion tends to overtake both the contact surface separating the driver and driven gases and the shock front itself. For weaker shocks, the overtaking effect is more pronounced than for stronger shocks, and the total duration of constant-pressure flow is correspondingly less than for the stronger shocks. A longer driver chamber is therefore desirable for operation with weaker shocks. On the other hand, for stronger shocks the contact surface follows the shock more closely, reducing the duration of constant-pressure "hot flow" (i.e., that preceding the contact surface). It is desirable to make pressure measurements related to shock impingement on solids in the hot

flow in order to avoid disturbances due to contact surface interactions. Thus for stronger shocks a longer driven chamber is necessary to provide hot flow of duration sufficient to accomodate measurements. The use of combustible driver gas introduces additional operating problems which have been discussed in Section III-A-3 of the present report.